Stabilization of Visually Guided Robotic Lampreys

Joram Overdevest

Master of Science Thesis

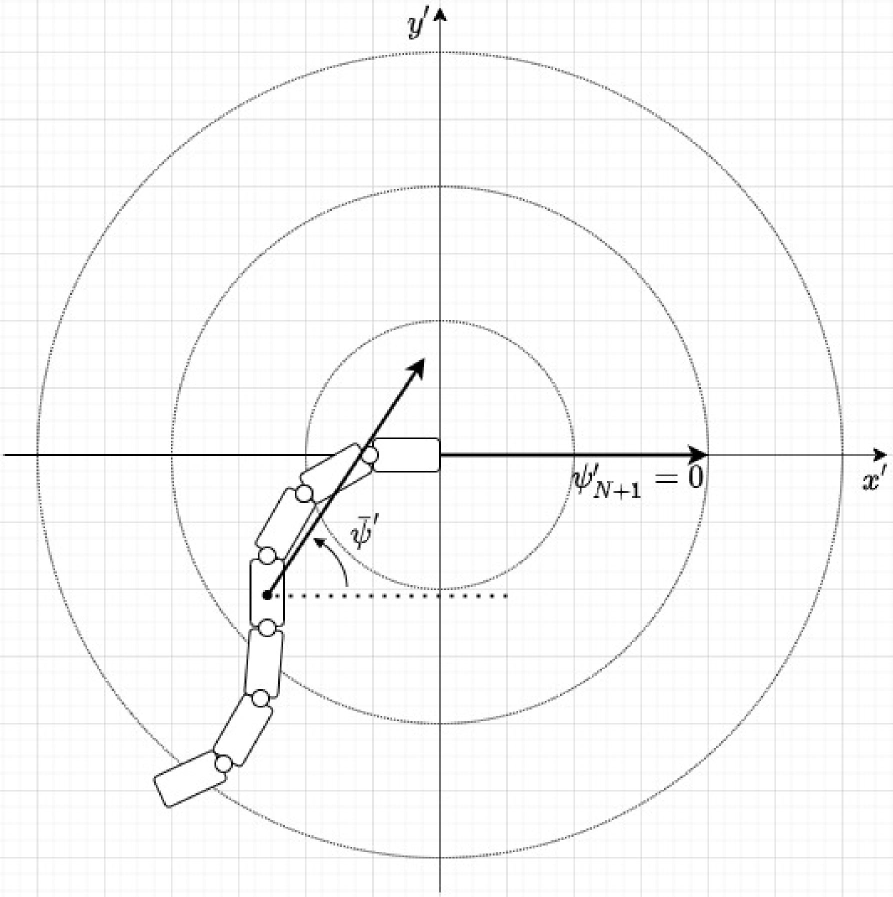

Delft University of Technology

Delft Center for Systems and Control

Stabilization of Visually Guided Robotic Lampreys

Master of Science Thesis

For the degree of Master of Science in Systems and Control at Delft University of Technology

Joram Overdevest

August 20, 2021

Faculty of Mechanical, Maritime and Materials Engineering (3mE) · Delft University of Technology

Abstract

This thesis contains two contributions to the stabilization of visually guided robotic lampreys: the head stabilization method and the head-led target tracking design. Both approach the problem that camera inputs, attached to the head segment, are disturbed due to the participation of the head in the locomotion gait of the robot. Head stabilization is designed to stabilize the head segment itself, and head-led target tracking is designed to stabilize the target in the field of view of the cameras.

The head stabilization and head-led target tracking designs are build upon the Ijspeert model. The Ijspeert model is an biologically inspired oscillator-based central pattern generator, capable of producing locomotion signals to achieve a lateral undulation gait. Analysis of this Ijspeert model is done by rewriting the model as a network of Kuramoto oscillators. This analysis concludes with a proof for the convergence of the phase differences of the Ijspeert oscillators.

Although methods that mitigate the head stabilization problem for robotic lampreys have been designed before, the head stabilization method in this thesis approaches the head stabilization problem as a control problem for the fist time, to the best of our knowledge. The head stabilization method is designed to align the head segment with the average body direction, by providing head stabilizing parameters to the Ijspeert model. Perfect head stabilization is achieved, under the assumption that the motor dynamics are instant. Even though head stabilization is not perfectly achieved in reality with non-instant motor dynamics, we have verified that the head stabilized Ijspeert model is an improvement in terms of head stability, compared to the Ijspeert model without head stabilization.

The designed head stabilization method is applied to a novel head-led target tracking design. This method combines a forward locomotion gait with a turning controller to perform target tracking, and is designed to increase the accuracy of visual information by directing the head segment towards the target. The head-led target tracking design is verified by placing the robotic lamprey in a virtual fluid environment with a target, which showed that the target is reached by the robot. Furthermore, the head-led target tracking design is compared to a design from the literature that does not direct the head segment towards the target. The head-led target tracking design shows improvements to the design from the literature in terms of the used performance measures.

Table of Contents

Preface ix

Acknowledgements xi

1 Introduction 1
- 1-1 Motivation 1
- 1-2 Locomotion Signal Generators 3
  - 1-2-1 Types of Locomotion Signal Generators 3
  - 1-2-2 Central Pattern Generators 4
  - 1-2-3 The Ijspeert Model 5
- 1-3 Head Stabilization for Visually Guided Robotic Lampreys 7
- 1-4 Contributions 8
- 1-5 Outline 9

2 Background and Preliminaries 11
- 2-1 Models for Robotic Lampreys 11
  - 2-1-1 State-of-the-Art System Models 11
  - 2-1-2 General Top Level System Description 14
- 2-2 Graph Theory and the Kuramoto Model 15
  - 2-2-1 Graph Theoretical Framework 15
  - 2-2-2 The Chain of Identical Kuramoto Oscillators 15
- 2-3 Body and Fluid Model 17
  - 2-3-1 Underwater Snake-Robot Model 18

3 Head Stabilization in a Lateral Undulation Gait 25

3-1 Ijspeert Model Analysis . . . 25

3-1-1 Lateral Undulation Gait . . . 25

3-1-2 Synchronization in the Ijspeert Model . . . 26

3-2 Head Stabilization . . . 29

3-2-1 Head Stabilization Problem . . . 29

3-2-2 Head Stabilization Method . . . 32

3-3 Numerical Results . . . 40

3-3-1 Models and Parameters . . . 40

3-3-2 Ijspeert Model Simulations . . . 42

3-3-3 Head Stabilization Simulations . . . 44

3-4 Discussion . . . 45

4 Head-led Target Tracking 47

4-1 Head-Led Target Tracking Problem . . . 47

4-2 Head-Led Target Tracking Design . . . 50

4-2-1 Head-Led Target Tracking System Description . . . 50

4-2-2 Head-Target Alignment Controller . . . 50

4-2-3 Turning Controller . . . 56

4-3 Numerical Results . . . 58

4-3-1 Simulated Designs . . . 58

4-3-2 Target Tracking Experiment . . . 59

4-4 Discussion . . . 65

5 Conclusions and Recommendations 67

5-1 Conclusions . . . 67

5-1-1 Head Stabilization . . . 67

5-1-2 Head-Led Target Tracking . . . 68

5-2 Future Directions . . . 70

A Supplementary Material for the Underwater Snake-Robot Model 71

A-1 Simplifications and Assumptions . . . 71

A-2 Parameters and Notations . . . 71

B Algorithms 75

C Turning Experiment 77

Bibliography 79

List of Figures

1-1 Schematic of the Ijspeert model network. 6
1-2 Head stabalizing modification in a Kuramoto oscillator-based CPG network . . . 7

2-1 The system description of Envirobot. 12
2-2 System schematic of Amphibot II. 13
2-3 Path following controller schematic used to simulate Mamba. 13
2-4 General top level description of simulated robotic lampreys. 14
2-5 The undirected graph underlying the chain network of identical Kuramoto oscillators. 16
2-6 Kinematic parameters in the snake model. 19

3-1 Definitions of kinematic variables in the head fixed polar coordinate frame. . . . 29
3-2 Schematic of the head stabilization problem. 30
3-3 System description of the head stabilized Ijspeert model. 32
3-4 The system schematic used in the head stabilization proof. 33
3-5 The evolution of the frequency differences. 43
3-6 The evolution of the phase differences minus the phase biases. 43
3-7 The evolution of the head-body alignment error signals, both for the head stabilized Ijspeert model and baseline Ijspeert model. 44

4-1 Schematic of head-led target tracking with the head-body alignment error signal and head-target alignment error signal. 48
4-2 System description of the head-led target tracking design. 51
4-3 Schematic of the head-target alignment control problem. 52
4-4 Schematic of two target tracking scenarios. 53
4-5 Visualization of the components of the reference signal for the head joint. 55
4-6 Schematic of the head-target alignment control. 57
4-7 The set-up for the target tracking experiments. 60

4-8 Evolution of the error signal of the head-led target tracking design. 61
4-9 The evolution of the head-target alignment error in the target tracking experiment for the head-led target tracking design and the Manfredi design. 62
4-10 The evolution of the head-body alignment errors in the target tracking experiment using the head-led target tracking design and Manfredi design. 63
4-11 The evolution of the head-target alignment error in the target tracking experiment for the head-led target tracking design with and without stabilization. 64

C-1 The results of the turning experiment with the Ijspeert model without stabilization. 78

List of Tables

3-1 Parameter values for the baseline and head stabilized Ijspeert model. 41

A-1 Values and definitions of the parameters used in the underwater snake-robot model. 72

Preface

This master thesis is part of the MSc program Systems and Control at Delft Center for Systems and Control (DCSC) at the Delft University of Technology (TU Delft). The thesis is supervised by main supervisor dr. Matin Jafarian and co-supervisor Clara Cavaliere.

Acknowledgements

The completion of this master thesis could not have been possible without the enthusiastic support of my thesis main supervisor dr. Matin Jafarian and co-supervisor Clara Cavaliere. Even though the pandemic did not allow us to meet much in person, I have greatly benefited from our collaboration and I much appreciate your assistance and contributions.

Delft, University of Technology
August 20, 2021

Joram Overdevest

Chapter 1

Introduction

Designing autonomous robots has been a great challenge for the field of robotics. Although significant steps have been made, as of today our most advanced robots are still outperformed by even the simplest of animals in many tasks. This has led the suggestion that biomimetic robotics are the solution for acquiring autonomous robots [30]. After all, ‘after 3.8 billion years of development, failures are fossils, and what surrounds us is the secret to survival’ [32].

One of the animals that has been of particular interest for biomimetic robotics is the lamprey. The lamprey is a jawless fish belonging to the vertebrates. It has diverged from the main vertebrate evolutionary line at an early stage of around 450 million years ago. Since then, the lamprey has evolved comparatively little and can therefore seen as a ‘prototype vertebrate’, making it a biologically interesting case [10]. Its spinal cord, responsible for the generation of inputs for the muscles during locomotion, shares all features of that of more complex vertebrae including humans, but with much fewer neurons. For this reason, the locomotor neuronal network of the lamprey has been well studied by experimental biologists [30].

1-1 Motivation

The motivation to research robotic lampreys comes from several applications. These applications range from the validation of biological theories to the improvement of aquatic autonomous robots. In this section, some of these applications are summarized.

Lampreys are particularly interesting for biologists, and collaboration between the fields of biology and robotics has been increasingly established. Advances in solving complex problems in robotics like locomotion and autonomous capabilities are aided by valuable insights from biologists, and bio-inspired robots are tools for biologists to validate theories. In Section 2-1-1 biologically inspired robots are described, with some being designed to form a platform for biological validation.

Bio-inspired locomotion in robotics improves our understanding of the workings of the spinal cord, which can be applied to aid neuroprostetics for people with a spinal cord injury [27].

This has been approached by artificially activating the spinal cord to recover the lost motor capabilities. Another application of robotic lamprey research is surgical robotics, where the aim is to make minimally invasive surgery instruments [6]. The design of a snake-like compliant and flexible shaft, for instance, makes high instrument manoeuvrability possible while keeping the incision size to a minimum. In such applications, high accuracy is of great importance. Achieving high accuracy is a shared goal among snake-like medical instruments and snake-like robotics.

Another important application for robotic lampreys is the improvement of the capabilities of aquatic robots. Aquatic robots are outperformed by biological fish in efficiency [7, 8], agility, acceleration and the ability to access confined spaces [19]. Bioinspired robots have to prove their advantage over conventional robots by showing improvements in adaptability, flexibility, robustness and autonomous behaviour [30]. Among the bioinspired robots, robotic lampreys are particularly maneuverable and flexible [17]. Their segmented body makes them inherently robust to perturbations, robust to partial failure, and modular.

Autonomous underwater vehicles are cost effective and safer alternatives to human operated vehicles [19, 22]. Furthermore, the requirement for mobility is increasing for underwater applications. This is where snake-like robots have much potential, not merely because of the slender and flexible body, but also because controlled manipulation of the body that is required for modification tasks of underwater systems is an inherent property [8]. An application of this includes inspection and maintenance for the oil and gas industry at sea, where cost-efficiency and accessibility play a big role. Furthermore, effective local guidance systems, e.g. for obstacle avoidance in unknown environments, remains a crucial task for many robots including underwater snake-like robots [19].

Aquatic robots can be deployed for environmental monitoring, where the aim is to retrieve information from the environment. Examples include water sampling and analysis using onboard chemosensors, biological sensors or GPS [5]. With chemosensors or biological sensors, the gradient of the concentration of a substance of interest can be followed. This is relevant for localization tasks like the localization of the source of chemical pollutants, oil or gas leakages [4, 5], or for chemical plume tracing [3]. With GPS, aquatic robots are capable of performing surveillance tasks of the environment, which are useful for investigating chemical pollution and greenhouse gasses in the water [5].

Robotic lampreys can also be equipped with cameras attached to the head, which allows for visually guided locomotion that is applicable to target tracking tasks. Visually guided robotic lampreys have been designed and constructed to validate biologically inspired visual guided locomotion methods [21, 31]. Other applications include the localization and removal of ocean debris [1] where robotic lampreys are desirable due to their energy efficiency, and visual inspection of maritime systems.

1-2 Locomotion Signal Generators

Locomotion is the central problem in the applications mentioned Section 1-1. This section explores the generation of locomotion signals for robotic lampreys. Robotic lampreys consist of a chain of segments connected by actuated joints. Like biological lampreys, robotic lampreys locomote by means of a lateral undulation gait. This two dimensional gait requires each joint to be actuated by a motor unit that receives reference signals from a locomotion signal generator. Selecting or designing such a locomotion signal generator is a challenge in the design of robotic lampreys.

In Section 1-2-1, different types of locomotion signal generators are explained. The type that is focused on in this thesis is the Central Pattern Generator (CPG), which is explored further in Section 1-2-2. The CPG of choice is the Ijspeert model, which is described in Section 1-2-3.

1-2-1 Types of Locomotion Signal Generators

The goal of locomotion control is to convert high level commands for e.g. speed and direction into the locomotion gaits that realize these commands. A fundamental difficulty for robotic lampreys is that they require a large number of actuators. Generally, locomotion signal generation is approached by having some periodic signal generator outputting signals to the actuators. The generator can then be controlled from a higher level for controlled locomotion.

The locomotion signal generators for robotic lampreys are categorized in three types: sine-based, model-based and CPG-based [14]. Sine-based generators produce a sine reference signal for the actuators with a phase delay from front to rear, which results in traveling sine-waves along the body. They can be designed with explicit control parameters that regulate characteristics of the locomotion gait like frequency and amplitude. A typical sine-based generator is described as [8]

$$\phi_{\text{ref},k}(t) = r_k \sin(\omega t + (k-1)\gamma) + \delta, \tag{1-1}$$

where $\phi_{\text{ref},k}(t)$ is the reference signal for the k^{th} motor unit, r_k the oscillation amplitude at joint k, ω the frequency, γ the phase-lag in the reference between two neighboring joints, and δ the offset used for turning. Sine-based generators are the most simple of the three types, but modulating sine-based generators from a higher level control can result in non-smooth transitions between locomotion gaits [14], which can pose a problem in control applications.

Model-based generators use models of the kinetics or dynamics of the robot body or the body-fluid interactions to design control laws used for the locomotion generation. These generators can be used to obtain optimal locomotion in terms of speed [14, 23]. However this method is not always suitable for modulation, and furthermore requires accurate models of the robot and the environment for good performance, which can pose a problem in unknown or difficult environments.

CPG-based locomotion signal generators are often inspired on some level by the biological locomotion network in animals [13]. CPGs are neuronal networks in animals responsible for rhythmic signal generation for the muscles. CPG-based approaches used for robotic applications generate locomotion signals form dynamical networks consisting of nodes described by either neuron dynamics or more abstract oscillators dynamics. Such networks exhibit limit cycle behaviour which generate the periodic locomotion signals. These limit cycles make the locomotion gait robust to perturbations, and modulating these limit cycles results in smooth transitions between locomotion gaits. Furthermore CPGs are better suited for sensory integration than the other two locomotion signal generation methods. Challenges of CPG-based approaches are the design complexity, and the complexity of the control via control parameters that are possibly not explicit [14].

The benefits of CPG-based locomotion signal generators make it a popular choice in recent literature [32]. Because of its benefits and close connection with the biological lamprey, the category of CPG-based locomotion signal generator is selected for this thesis and further explained in the next subsection.

1-2-2 Central Pattern Generators

Coordinated rhythmic muscle activation patterns underlie many motions in the bodies of animals, including respiration, swallowing and locomotion. Muscles participating in this require rhythmic input signals, which are produced by networks of interconnected neurons that exhibit rhythmic behaviour without requiring rhythmic inputs [32]. This behaviour is not trivial, considering that the basic elements, the neuron and synapse, do not exhibit this rhythmic behaviour on their own. These networks are called central pattern generators, where *central* explicitly indicates that sensory feedback is not required for the generation of rhythmic signals [13].

The CPG responsible for locomotion is located in the spinal cord, and converts signals from the visual system into inputs for the muscles participating in locomotion. The capability of converting low dimensional nonrhythmic inputs into high dimensional rhythmic and coordinated outputs makes it a critical link in the visuomotor network. Artificial CPG models are generally based on biological CPGs, and are categorized into three different levels of abstraction: biophysical, connectionist or oscillator-based [13, 20]. Biophysical neuronal networks model the voltage of neuron membranes as a result of ion flows, like in Hodgkin-Huxley type models. These are the most biologically accurate, and are used to study rhythmic activities in small networks [13]. Connectionist models describe neurons with simplified models like integrate-and-fire or firing rate models. Of interest to these models is the rhythmic behaviour emerging from network properties and synchronisation between different rhythmic parts in the network [13]. Oscillator models describe large oscillating groups of neurons with oscillators that intrinsically exhibit rhythmic behaviour. The focus of oscillator-based models is on the effect of coupling between oscillators on synchronization or phase difference between oscillators [13]. A more detailed review on these three categories of CPGs can be found in [24].

As this thesis relies on the control of the gait to perform head stabilization and target tracking, an oscillator-based model is selected for the generation of locomotion signals. Although oscillator-based models are the least biologically accurate, they have proven themselves to be the best suited for such control tasks. A description of the oscillator-based CPG model of choice is given in the next section.

1-2-3 The Ijspeert Model

The locomotion signal generator used in this thesis is the Ijspeert model. The Ijspeert model is an oscillator-based CPG model designed for generating locomotion signals for robotic lampreys. Its simplicity and explicit control parameters have made it a popular model in state-of-the-art designs. The model has been developed for Amphibot II, and has been used in several other designs since. The original model describes a double chain of phase oscillators with amplitude control in which joints are actuated by pairs of oscillators [14]. A later variant of the model describes a single chain of oscillators [21]. The single chain variant is used in this research and elaborated in this section.

The Ijspeert model in [21] describes N phase oscillators with amplitude control. Each oscillator $k \in \{1, \ldots, N\}$ is described by the following dynamics.

$$\begin{cases} \dot{\theta}_k = \omega_k + \sum_l \mathrm{w}_{lk} \sin(\theta_l - \theta_k - \gamma_{lk}) \\ \ddot{r}_k = -2\zeta\nu_0 \dot{r}_k + \nu_0^2 (R_k - r_k) \\ \phi_{\mathrm{ref},k} = r_k \cos(\theta_k) + \delta_k \end{cases} \tag{1-2}$$

The oscillator states θ_k and r_k are the phase and amplitude of oscillator k. These two are combined with turning parameter δ_k to obtain $\phi_{\mathrm{ref},k}$, the output of the k^{th}. The phase and amplitude dynamics are independent of each other and can therefore be treated separately.

The phase dynamics are equivalent to the widely studied Kuramoto model [2, 15] with phase bias terms (more on the Kuramoto model in Section 2-2). The parameter ω_k is the exogenous frequency (in rad/s), w_{lk} and γ_{lk} are the coupling strength and phase bias from oscillator l to k, respectively. In the chain network, w_{lk} and γ_{lk} only have nonzero values for $|k - l| = 1$ or along the links in Figure 1-1. instead of the general description of the phase dynamics in Eq. (1-2), the simplified version given in Eq. (1-6) is used in this thesis by posing the following restrictions on the three parameters in the phase dynamics [14, 21].

$$\gamma_{k,k+1} = -\gamma_{k+1,k} \qquad \forall k \in \{1, \ldots, N-1\} \tag{1-3}$$

$$\omega_k = \omega \qquad \forall k \in \{1, \ldots, N\} \tag{1-4}$$

$$\mathrm{w}_{kl} = \begin{cases} \mathrm{w} > 0 & \forall k, l \in \{1, \ldots, N\}, |k-l| = 1 \\ 0 & \text{otherwise} \end{cases} \tag{1-5}$$

The amplitude dynamics are described by a damped second order system that tracks the amplitude setpoint R_k. The parameters are chosen such that R_k is the global equilibrium of r_k. The amplitude dynamics are introduced to make the amplitudes r_k follow sudden changes in the setpoint R_k in a smooth manner. However, the amplitude dynamics are not of interest for this thesis, and are therefore not used for simplicity. By keeping the amplitudes r_k constant and including the above described simplification on the phase dynamics, the Ijspeert model reduces to

$$\begin{cases} \dot{\theta}_k = \omega + \mathrm{w} \sum_l \mathrm{A}_{lk} \sin(\theta_l - \theta_k - \gamma_{lk}), \\ \phi_{\mathrm{ref},k} = r_k \cos(\theta_k) + \delta_k. \end{cases} \tag{1-6}$$

Here, $A \in \mathbb{R}^{N\times N}$ is the adjacency matrix of the Ijspeert network (see Section 2-2). Note that, by leaving out the amplitude dynamics, this model has essentially become the Kuramoto model combined with a function that maps the phases to the outputs. Results in this thesis for the Ijspeert model without amplitude control are extendable to the amplitude-controlled variant of the Ijspeert model (the reason behind this is elaborated on in Remark 2). The model in Eq. (1-6) will be denoted as the Ijspeert model (and not the Kuramoto model) to explicitly build upon this popular locomotion signal generator for robotic lampreys.

The single chain network of Ijspeert oscillators is shown in Figure 1-1. The oscillators in the network are phase-coupled with their neighboring oscillators, indicated with the arrows between the oscillators. The output of each oscillator goes to the corresponding motor unit that tracks the reference angle $\phi_{\text{ref},k}$ with the joint angle ϕ_k (see Figure 2-4). The dynamics of the Ijspeert model have a limit cycle that is shaped by five parameters: ω, w, $\gamma_{k,k+1}$, r_k and δ_k. These parameters can either be set constant or used as control parameters. In this thesis, turning control is used for target tracking, so the turning parameter δ_k is considered a control parameter. The speed and other gait characteristics, determined by the other four parameters, are not controlled. These four parameter are therefore set constant, and the values of the constants are chosen to make the oscillator network output a rhythmic locomotion pattern with desired properties. Parameter choices for the generation of desired locomotion signals are described in Section 3-1-2, and parameter settings for the head stabilization objective are described thereafter in Section 3-2-2.

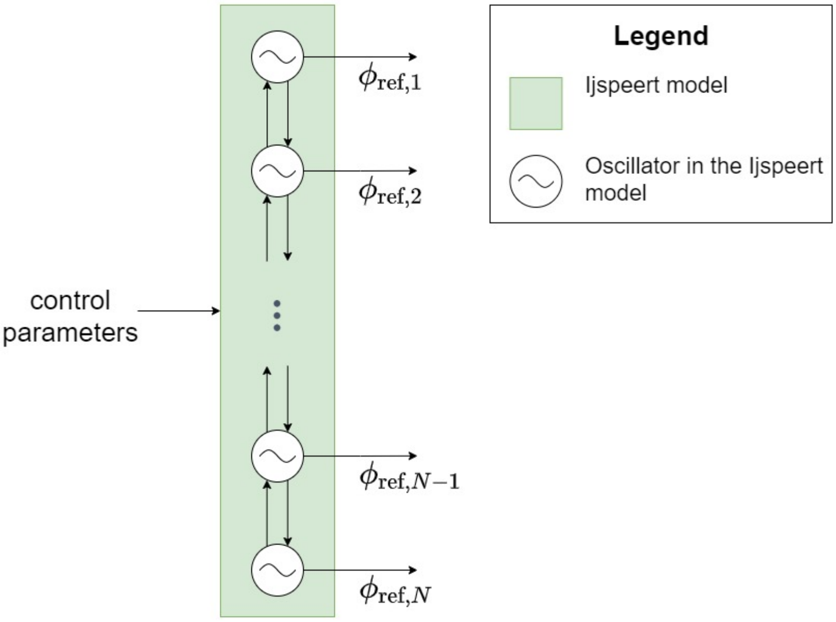

Figure 1-1: Schematic of the Ijspeert model network. This figure is modified from the double chain network figure in [14]. The Ijspeert model is substituted for the 'locomotion signal generator' subsystem in Figure 2-4 for the remainder of this thesis.

1-3 Head Stabilization for Visually Guided Robotic Lampreys

Biological lampreys propel themselves using a lateral undulatory locomotion gait. This propulsion mechanism is used by robotic lampreys as well, and has advantages over propeller based propulsion mechanisms, e.g. in efficiency improvements (see Section 1-1). However, as visually guided robotic lampreys rely on the inputs from cameras attached to the head, the participation of the head in these lateral undulations introduces a disturbance on the visual inputs. Reducing this disturbance would allow visually guided robotic lampreys to be deployable for precision tasks in aquatic environments [31], which can serve several applications as reviewed in Chapter 1-1.

The problem of inaccurate visual inputs caused by oscillations of the head segment has been pointed out to cause problems for visually guided robotic lampreys. For instance, it has caused the robotic lamprey Envirobot to overshoot its objective [31], and the robotic lamprey in [21] has experimentally been shown to have more difficulties keeping the target in the camera field of view without any form of head stabilization.

Three approaches are suggested in the literature to reduce the disturbance of the visual inputs caused by the head oscillations: head stabilization, eye compensation and visual memory [21, 31]. The first two are inspired by the fact that the movements of the eyes, neck and body of a lamprey are dependent, such that movements in one part results in compensating movements in other parts in response [21, 26]. The latter is based on the fact that lampreys, like many other animals, use their memory to estimate the location of targets when they are out of sight [31]. The approach taken in this thesis is head stabilization.

Head stabilization methods in the literature are mostly in the form of local modifications to existing locomotion signal generators. Two examples of this are discussed here. The first example is a modification on a CPG network of a robotic snake proposed by [7]. The original CPG consists of a network of phase-coupled Kuramoto oscillators (see Section 2-2-2) with nearest-neighbor coupling. The coupling of the first oscillator with the rest of the network is modified such that the head becomes more stable. This modification is shown in Figure 1-2, where the parameters φ and $-\varphi$ indicate the phase offset term between the oscillators. The phase offset between the oscillators of the first and third joint is set to π. With this network, the variations of the angle difference of the head segment with the direction of motion is found to decrease by a factor of about three.

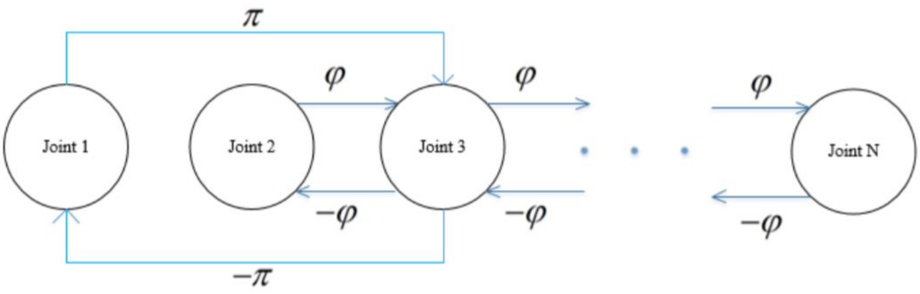

Figure 1-2: Head stabalizing modification in a Kuramoto oscillator-based CPG network [7].

In the second example, head stabilization is achieved in a network of Ijspeert oscillators (see Section 1-2-3). The head stabilizing method proposed in [21] works by inverting the phase of the output of the first oscillator. This inversion of the phase is written as

$$x_1 = -r_1 \cos(\theta_1), \tag{1-7}$$

where x_1 is the output of the first oscillator, and r_1 and θ_1 are states of the Ijspeert oscillator similar to the description in Eq. (1-6). The minus sign in front of r_1 inverts the phase of the oscillator. In [21] the effect of this head stabilization method is tested by measuring the time performance of approaching an object with a robotic lamprey in a pool. Fifteen trials were performed where the head stabilization was included, and fifteen were performed with the unmodified network (without the head stabilization modification). To compare the two groups of trials, the average and standard deviations of both groups were determined. It is found that the robot with head stabilizing modification had a smaller average and standard deviation to reach the object compared to the robot without head stabilization modification. Furthermore, without the modification the robot lost the object out of sight in four of the fifteen cases. With the network that included the modification the robot did not loose the object out of sight in any of the trials.

Besides using local modifications, another approach is to design the entire signal generator to achieve a more head stabilized gait. Actually, by making the gait of the robotic lamprey resemble the gait of a biological lamprey more closely, a decrease in visual distortions can be achieved. The gait of a biological lamprey can be described with a time dependent sine wave with an amplitude that increases exponentially from front to rear [12]. The head segment remains more stable in this locomotion gait, compared to the gait with constant amplitude that is most often used in robotic lampreys.

1-4 Contributions

In Section 1-3, two head stabilization methods from literature are described. The head stabilization method in [7] reduces the variations of the difference between the head segment direction and the direction of motion by a factor of about three, compared to not using the head stabilization method. Furthermore, the head stabilizing method in [21] prevented the robot from losing the target out of sight, which did occur when no head stabilizing method was used. Both of these head stabilization methods have been shown to reduce the disturbance of the head oscillations on the camera inputs, but none have focused on actually making this disturbance as small as possible. Therefore, reducing these disturbances is, for the first time to the best of our knowledge, approached as a control problem in this thesis. The contribution of this thesis is twofold.

First, a head stabilizing method is designed that is capable of perfectly stabilizing the head of a robotic lamprey in ideal circumstances, and significantly improving head stability in non ideal circumstances compared to using the Ijspeert model without the head stabilization method. The method uses the Ijspeert model as a basis, a commonly used CPG model in state-of-the-art robotic lampreys (see Section 1-2-3). The method works by providing head stabilizing parameters to the Ijspeert model. This requires no significant changes to the software or hardware of the robot, making it easy to implement in robotic designs using the Ijspeert model. Besides its ease of implementation, the main motivation for designing this method is to pioneer the control approach to head stabilization.

Second, a novel accuracy improving target tracking method for visually guided robotic lampreys is proposed: the head-led target tracking method. Novel to this method is that the head is directed towards the target during target tracking, thereby stabilizing the target in the field of view of the cameras. This target stabilization is combined with a turning control strategy that is a variation on the strategies from [14, 21], which works by turning the body in alignment with the head. In combination with the head being directed towards the target, this achieves the turning of the body towards the target. Using this method, the robot is able to approach the target while keeping the target stabilized in the camera field of view. To the best of our knowledge, this approach to target tracking with a robotic lamprey is the first of its kind. Besides the improved stabilization of the target in the field of view, the simulated robot using the head-led target tracking method is shown to reach the target faster than the simulated robot using the head-stabilizing method from [21] in a virtual target tracking experiment described in Section 4-3-2.

1-5 Outline

This thesis is structured as follows. Chapter 2 provides the background and preliminaries for the remainder of the thesis. Chapters 3 and 4 contain the main contributions of this thesis. The first describes the method for motion generation and the proposed head stabilization method, and the second describes the proposed target tracking method. Both methods are verified and compared using numerical simulations. Last, Chapter 5 contains the conclusion of the thesis, and provides recommendations for future directions.

Chapter 2

Background and Preliminaries

This chapter describes the background and preliminaries for the remainder of the thesis. Section 2-1 provides the background for system models of robotic lampreys, together with a general top level system description that is used as a basis in the rest of this thesis. After that, Section 2-2 explains basic concepts of graph theory and explains the relation between the Ijspeert model and the Kuramoto model, which is required in Chapter 3. Section 2-3 gives an overview of different simulation methods for (robotic) lampreys, and provides the underwater snake-robot model used for the simulations in this thesis.

2-1 Models for Robotic Lampreys

The designs of some state-of-the-art robotic lampreys are explored in Section 2-1-1. These designs give insight in current advancements in the field, and are inspirations for the problem which has been investigated in this thesis. A general block diagram model for robotic lampreys is provided in Section 2-1-2, which is used as a basis for models in the remainder of this thesis.

2-1-1 State-of-the-Art System Models

Although lampreys can move in three dimensions, their propelling locomotion gait is a two dimensional movement. The part of the locomotion network in the spinal cord that facilitates this planar motion is well studied by biologists. Most robots inspired by lampreys are planar robots as well, which are made buoyant such that their movement is restricted to the surface of the water. Snake-like robots, a more general category of robots, also include robots that are able to move in three dimensions. Some of these do make use of the biological knowledge of the lamprey in their design.

Envirobot

Envirobot is a robotic lamprey made by EPFL that was first constructed in 2016 [5]. The system model of the robot is given in Figure 2-1. The system of both versions is divided into a sensory processor part, a locomotion pattern generator part, and a body consisting of multiple identical modules, each driven by a motor unit. The block diagram of the 2016 version is shown in Figure 2-1. In this design the sensory input is not camera based, whereas the sensory subsystem of the 2020 version is camera based. Apart from that, the locomotion and actuator part are the same.

The locomotion part of the diagram, referred to with *ARM* in the figure, consists of the CPG. This term is elaborated on in Section 1-2-2. It gets input from the sensors of the system, and converts that into the reference angle θ_{ri} motor i should follow (which in the rest of this review will be referred to as $\phi_{\text{ref},k}$). The robotic lamprey consists of many segments, and the overall shape is determined by the joint angles between those segments. To control the shape of the body, each joint is controlled by a motor unit, of which the i^{th} motor unit is shown in the diagram in the *Modules* block. The unit is designed to make the angle of joint i follow the reference signal. An encoder measures the current angle, which is subtracted from the reference signal to obtain the angle error signal $e_{\psi i}$ for the position controller. This converts the error into the control input u for the motor. Envirobot uses a PD controller for this [5]. This closes the inner-loop controlling each of the joint angles. The gait of the robot is controlled by the heading and speed controller. Using the control parameters of the CPG, they alter the reference outputs to the motor units.

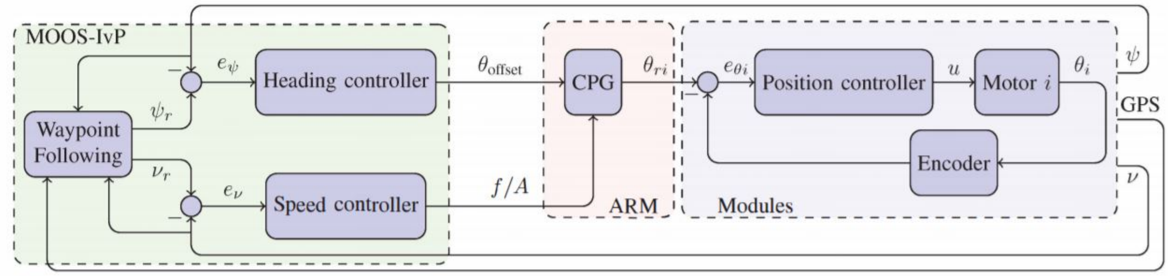

Figure 2-1: The system description of Envirobot. Subsystems are categorized into three groups according to the hardware they are executed on: *MOOS modules* provide waypoint following, as well as the lower level heading and speed control; *ARM* containing the CPG; and the *Modules* for angle control of the joint angles. [5]

For the sensory components of the system, the focus will be shifted towards the 2020 model of Envirobot, applied in [31] and simulated in [16]. This system uses a type of cameras to observe its surroundings. The visual data is processed by an artificial neural network to provide inputs for the CPG. These inputs come in the form of a desired heading direction and speed [31].

Amphibot

Another series of biologically inspired robots from EPFL is the Amphibot with versions I, II and III. These predecessors of the Envirobot are also based on snake-like animals and lampreys, and are similar in design. Figure 2-2 shows the system schematic of Amphibot II, which is designed to receive high level control input from a remote controller.

The actuation of the joints is done in the same way as in Envirobot. The reference signals for the motor units are generated by a double chain of Ijspeert oscillators, and the characteristics of the gait are manipulated with the control parameters from the interface.

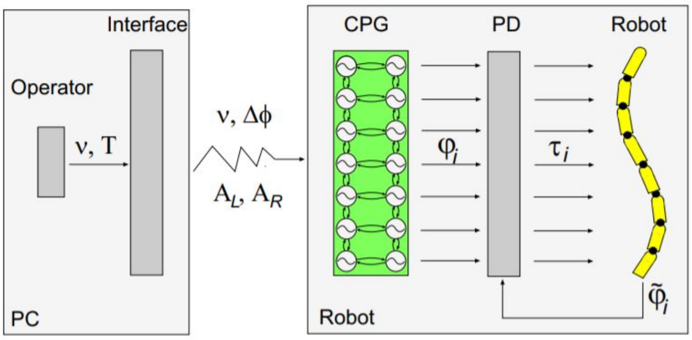

Figure 2-2: System schematic of Amphibot II. High level commands from the remote control, given as v and T, are transformed into CPG inputs v, $\Delta\phi$, A_L and A_R which used to modify the pattern generation. The CPG outputs reference signals to the PD controllers that make the joints follow the reference signal [14].

Mamba

Mamba is an underwater snake-like robot with path following as main objective. In [8], Mamba is both simulated and build to compare data from simulations and experiments. Its blockdiagram is given in Figure 2-3. When simulating a robot in a virtual environment, the motor dynamics and body mechanics need to be described, as well as the interactions with the surrounding fluid. In Figure 2-3 the body and fluid dynamics are represented in one block: the *Underwater Snake-like Robot*. In order to simulate the movement of a robotic lamprey through a fluid, the body dynamics, fluid dynamics and body fluid interactions will need to be included.

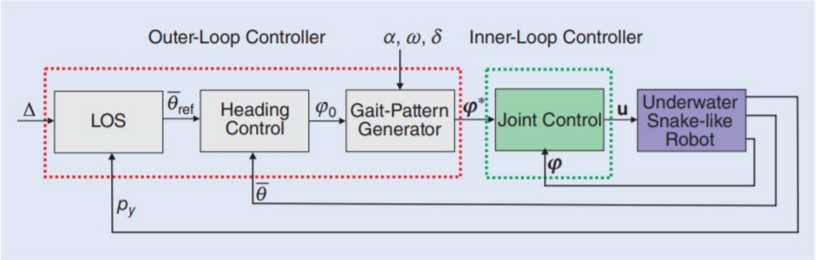

Figure 2-3: Path following controller schematic used to simulate Mamba [8].

The Bio-Inspired Autonomous Swimming Robot

The robotic lamprey designed in [21] has a relatively high level of biological accuracy. It includes two cameras at the tip of the head, sensors that are analogous to the stretch receptors in biological lampreys, distributed control, and a waterproof silicon skin. This robot is of particular interest to this thesis for two reasons. One, the robot uses a single chain of Ijspeert oscillators for the generation of locomotion signals, which is also used in this thesis (more on that in Section 1-2-3). And two, this is one of the few robotic lampreys that includes a head stabilizing method, as described in Section 1-3.

2-1-2 General Top Level System Description

Robotic lampreys generally share a similar top level system description. A concise diagram for simulated robotic lampreys is given in Figure 2-4. This diagram is used as a basis for building the system in this thesis.

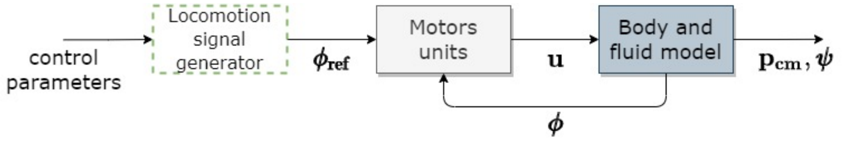

Figure 2-4: General top level description of simulated robotic lampreys. Different type of locomotion signal generation models can be substituted for the general 'locomotion signal generator' subsystem.

The locomotion signal generator is of highest interest, and understanding this subsystem it is required to generate and modify the reference signals that eventually determine the locomotion gait. It has taken many different forms in past robotic designs, and is the subsystem where knowledge about biological lampreys is applied. The subsystem generates the reference signals for the motor units. As each joint is actuated by one such a motor, the locomotion signal generator needs to output as many signals as the number of joints. The signals are required to be rhythmic and coordinated to obtain a propelling locomotion gait. Coordinated here means that the signal to each of the motor units needs to be carefully adjusted to the signals to the other motors, in order to achieve an overall locomotion goal. Different types of locomotion signal generators are explored in Section 1-2. The gait is manipulated for control purposes using the control parameters.

The motor units subsystem is a combination of the motor controllers, motors and encoders. The encoder in the k^{th} motor unit measures the joint angle of the k^{th} joint, ϕ_k. The motor controller converts error signal $\phi_{\text{ref},k} - \phi_k$ into a control input for the motor. The motor, subsequently, converts the control inputs into torques u_k that acts on joint k.

The body and fluid model subsystem contains the kinematics of the robot and the dynamics resulting from motor forces and body-fluid interactions. This thesis makes use of a model that combines the effect of the kinematics and fluid dynamics into a single description for the equations of motion. The subsystem can be considered as the plant of the entire system, and all other subsystems are essentially in place to provide the correct input torques $\mathbf{u}$. The body and fluid model converts the torques $\mathbf{u}$ into the position of the Center of Mass (CM), $\mathbf{p_c m}$, and the orientation of the segments, $\boldsymbol{\psi}$. The dynamic model is elaborated on in Section 2-3.

2-2 Graph Theory and the Kuramoto Model

As mentioned in Section 1-2-3, the phase dynamics of the Ijspeert model in Eq. (1-6) are described by the Kuramoto model with phase bias terms $\gamma_{k,k+1}$. This is convenient for the analysis in this thesis, as the Kuramoto model has been widely studied in literature. This section mainly serves the purpose of rewriting the phase dynamics of the Ijspeert model in vector form for the Kuramoto model analysis in Chapter 3, which is done in Section 2-2-2. This conversion requires a graph theoretical framework that is introduced first in Section 2-2-1.

2-2-1 Graph Theoretical Framework

Although the theory described in this part is applicable to undirected graphs in general, the specific undirected chain graph $\mathcal{G}$ of N nodes and $e = N - 1$ links is considered here. Two matrices related to graph $\mathcal{G}$ are introduces: the adjacency matrix and the oriented incidence matrix.

The adjacency matrix $\mathrm{A} \in \mathbb{R}^{N\times N}$ is a representation of $\mathcal{G}$ that contains information about how the nodes are connected. Namely, $\mathrm{A}_{lk} = 1$ when the graph contains a link from node l to k, and $\mathrm{A}_{lk} = 0$ otherwise [9]. In the chain network considered in this thesis, $\mathrm{A}_{lk} = 1$ for $|k - l| = 1$ and $\mathrm{A}_{lk} = 0$ otherwise.

Next, the oriented incidence matrix of graph $\mathcal{G}$ is described. To do so, the orientation of an undirected graph and the incidence matrix of a directed graph are explained first. To start with the first, the orientation of an undirected graph is an assignment of exactly one direction to each of the links in the graph [9, 29]. Therefore, an undirected graph that is assigned an orientation is a directed graph. As each undirected link can be assigned two different directions, the orientation is in general not unique with respect to the graph. Secondly, the incidence matrix $\mathcal{B}$ of a directed graph contains information about the direction of the links with respect to the nodes. The elements of the matrix are $\mathcal{B}_{ij} = 1$ if link j is incoming to node i, $\mathcal{B}_{ij} = -1$ if link j is outgoing from node i, and $\mathcal{B}_{ij} = 0$ otherwise [9].

Using these definitions, the oriented incidence matrix $\mathrm{B} \in \mathbb{R}^{N\times e}$ of the previously defined undirected graph $\mathcal{G}$ is defined as the incidence matrix of $\mathcal{G}^\sigma$, with $\mathcal{G}^\sigma$ being the directed graph resulting from the assignment of any orientation σ to $\mathcal{G}$ [9]. As any orientation is allowed, naturally this matrix is not unique with respect to $\mathcal{G}$.

2-2-2 The Chain of Identical Kuramoto Oscillators

The phase dynamics of the Ijspeert model in Eq. (1-6) is rewritten as a chain of identical Kuramoto oscillators without exogenous frequencies, which is shown in Eq. (2-1). This description is obtained by applying the coordinate change described in Eq. (2-2). Note that this shift is only possible because of the restrictions on $\gamma_{k,k+1}$ and ω in Eq. (1-3) and (1-5), respectively.

$$\dot{\vartheta}_k = \mathrm{w} \sum_{l=1}^{N} \mathrm{A}_{lk} \sin(\vartheta_l - \vartheta_k) \tag{2-1}$$

$$\vartheta_k \equiv \theta_k - \omega t - \sum_{l=k}^{N-1} \gamma_{l,l+1} \qquad \text{for } k \in \{1, \dots, N-1\} \tag{2-2a}$$

$$\vartheta_N \equiv \theta_N - \omega t \tag{2-2b}$$

Eq. (2-1) contains adjacency matrix $\mathrm{A} \in \mathbb{R}^{N \times N}$ (see Section 2-2-1). Besides simplifying the dynamics, this coordinate shift allows for the simplification of the underlying network. The Ijspeert network in Eq. (1-1) has a different coupling from oscillator k to l than from oscillator l to k (since $\gamma_{kl} \neq \gamma_{lk}$). By removing the phase bias terms, the links only describe the coupling weights, and these are equal for all couplings. Therefore, the coupling in the chain of identical Kuramoto oscillators can be modelled as the undirected graph $\mathcal{G}$ in Figure 2-5 (which is the same as described in Section 2-2-1). In this graph, the oscillators are represented with nodes and the couplings with links. Note that the matrix $w\mathrm{A}$ describes the coupling weights in both this undirected graph and the directed graph in Figure 1-1.

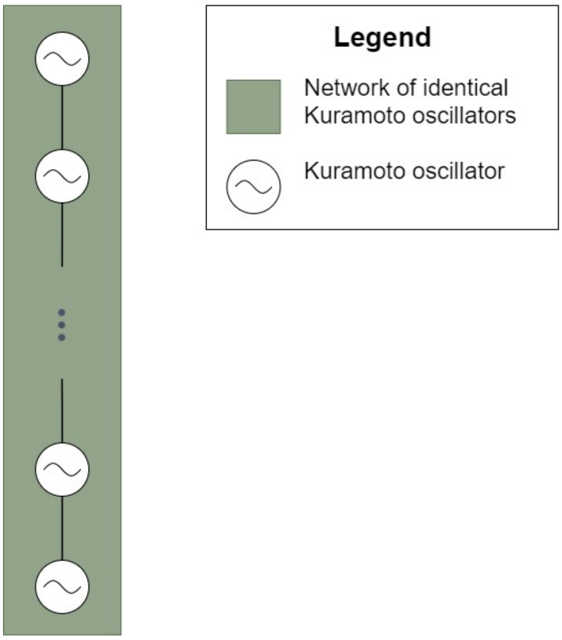

Figure 2-5: The undirected graph underlying the chain network of identical Kuramoto oscillators.

Using the undirected graph $\mathcal{G}$, the Kuramoto model in Eq. (2-1) can be rewritten in vector form by introducing the oriented incidence matrix $\mathrm{B} \in \mathbb{R}^{N \times e}$ of the oriented graph $\mathcal{G}^\sigma$ (see Section 2-2-1) as [15]

$$\dot{\boldsymbol{\vartheta}} = -w\mathrm{B} \sin(\mathrm{B}^\top \boldsymbol{\vartheta}). \tag{2-3}$$

An important property of this equation is that it holds for any orientation σ.

2-3 Body and Fluid Model

Validating novel target tracking methods is done by simulating a robotic lamprey in a virtual pool of water. Besides a description of the locomotion signal generation and motor dynamics, such simulations require a model that captures the effect of the motor forces and body-fluid interactions on the body of the robot. For the purposes of this thesis, the body and fluid models are integrated in one model. The motor torques are the control inputs for this dynamic model, the position of the CM and the orientation of the segments of the robotic lamprey are the outputs. External currents can be seen as disturbances, but these are not considered in this thesis.

The body-fluid interactions are particularly complex. They describe external forces on the body as a result of changes in the shape of the body. Different models for these interactions exist in the literature with varying accuracy and computational complexity. These models include: 1) Computational Fluid Dynamics (CFD) models, 2) a combination of the large amplitude elongated body theory (LAEBT) and the Taylor model, and 3) the underwater snake-robot model. The models are first explained, and thereafter an argument is made to use one of the models in this thesis.

The most accurate and computationally demanding models are a combination of a computational fluid dynamic (CFD) model and a model for the boundary interaction between the body and fluid. The CFD model use the Navier–Stokes equations for the dynamics of the liquid. Interaction between the fluid and body are described using the immersed boundary framework, which translates forces between the structure and the fluid. The Navier-Stokes equations combined with the immersed boundary framework have been used to simulate lampreys in [11, 28].

Simplifications of the hydrodynamics specifically for elongated bodies like that of the lamprey exist, which are computationally lighter. Two well known simplified models are the large amplitude elongated body theory (LAEBT) of Lighthill [25] to describe reactive forces, and the Taylor model to describe the resistive forces. In the slow swimming limit, the hydrodynamics are dominated by resistive forces, which are drag forces due to the viscosity of the fluid. In the fast swimming regime, the hydrodymanics are dominated by reactive forces that arise from the acceleration of the fluid. Therefore, this is also referred to as the 'added mass effect'. Underwater snake-like or lamprey-like robots lie in between these two extreme cases [17], so a combination of the reactive and resistive forces needs to be considered. These models are computationally lighter than the Navier-Stokes equations, which make them more suitable for model-based control applications [8]. However, these models require major simplifications, e.g. they neglect the effect of fluid torques [17]. These are not always grounded well and can introduce varying levels of inaccuracy [25]. The accuracy of the Lighthill and Taylor models are tested for a simulated lamprey in [28] by comparing them to the 2D Navier-Stokes equations with the immersed boundary framework. The Lighthill model shows a good level of agreement, and its assumptions are thought to be reasonably grounded. The Taylor model, however, shows a lower level of agreement which, according to the source, is probably because its assumptions do not hold well enough.

A more recent approximation of the hydrodynamics is the underwater snake-robot model given in [17]. In recent years this model has been used for several control designs including the planar snake-like robot Mamba in [8]. On the one hand, the model is more accurate that the Lighthill and Taylor models because it takes into account more hydrodynamic effects than previous approximations (reactive forces, linear and nonlinear resistive forces, fluid torques and fluid current). On the other hand, the model remains computationally light compared to CFD models [8]. In [17], the hydrodynamic model is combined with the kinematics of the robot to obtain a single state space representation of the body and fluid. To the best of our knowledge, this model is the most accurate analytical approximation of the hydrodynamics of a segmented robotic lamprey that is currently available.

The nature of the research in this thesis does not require the accuracy of the fluid model to be as high as possible. Still, the accuracy of the model should be high enough for experiments in the simulation to be representative for experiments in a real fluid. Furthermore, computational complexity and ease of implementation are important factors in the consideration. For these reasons, and the fact that this model has proven itself for similar applications, the underwater snake-robot model is chosen for this thesis. In the remainder of this section, a description of this model is given.

2-3-1 Underwater Snake-Robot Model

The underwater snake-robot model is described in [17,18], and used to model the underwater snake robot Mamba in [8]. The locomotion signal generator of Mamba is sine-based, but the underwater snake model can be used for CPG-based robotic lamprey as well by replacing the sine-based generator with the Ijspeert model. This only changes the way in which the inputs $\mathbf{u}$ to the underwater snake model are generated.

With N the number of joints, the robot has $N+3$ degrees of freedom in the planar snake model: $N+1$ for each segment orientation and 2 for the x and y positions of the CM of the robot. The model describes the dynamics of these segment angles and position of the CM of the robot with a state space representation of $2N+6$ states. This state space model is given in Eq. (2-4).

$$\dot{\mathbf{x}} = \begin{bmatrix} \dot{\boldsymbol{\psi}} \\ \dot{\mathbf{p}}_{\text{cm}} \\ \ddot{\boldsymbol{\psi}} \\ \ddot{\mathbf{p}}_{\text{cm}} \end{bmatrix} = \mathbf{F}(\mathbf{x}, \mathbf{u}) \tag{2-4}$$

To obtain the expression for $\mathbf{F}(\mathbf{x}, \mathbf{u})$, expressions for $\ddot{\boldsymbol{\psi}}$ and $\ddot{\mathbf{p}}_{\text{cm}}$ in terms of the states $\boldsymbol{\psi}$, $\mathbf{p}_{\text{cm}}$, $\dot{\boldsymbol{\psi}}$ and $\dot{\mathbf{p}}_{\text{cm}}$ and the input $\mathbf{u}$ need to be obtained. This section focuses on obtaining these expressions by making use of models for the kinematics, fluid forces and fluid torques. The content of this section is mainly borrowed from [8,17,18]; for more detail the reader is referred to these original sources[1]. Supplementary material for this section is provided in Appendix A, and includes simplifications, assumptions and notations, as well as descriptions and values of the parameters.

---

[1] Note that here the joint angles are denoted with ψ_k, whereas in the source they are denoted with θ_k.

Kinematics

In this part, the kinematics of the robot are described. These are used later on for constructing the equations of motion. Definitions of relevant parameters are illustrated in Figure 2-6. Note that segment 1, the left most segment in Figure 2-6a, is defined as the tail segment, and segment $N+1$, the right most segment in the figure, is defined as the head. Head first swimming is considered forward swimming throughout the thesis.

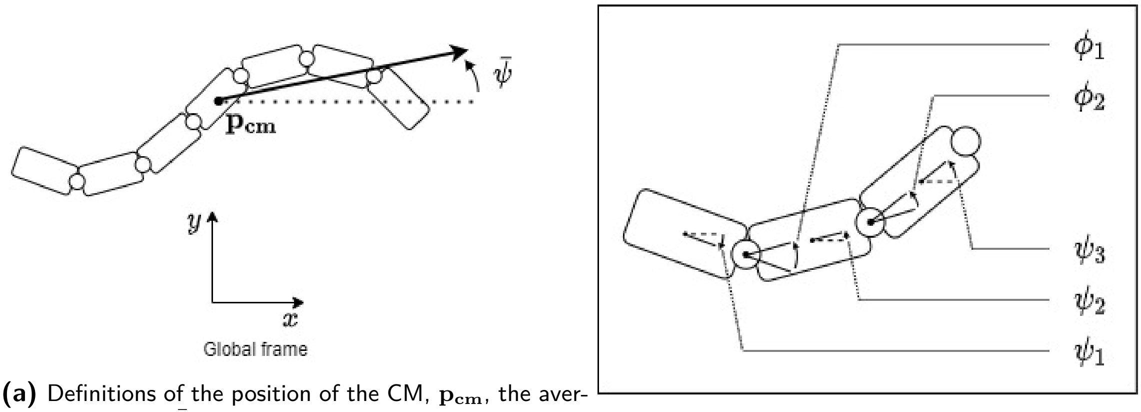

(a) Definitions of the position of the CM, $\mathbf{p}_{\mathrm{cm}}$, the average body angle, $\bar{\psi}$, and the global frame.

(b) Definitions of the first few joint angles ϕ_k and segment angles ψ_k.

Figure 2-6: Kinematic parameters in the snake model. The image is inspired by Figure 1 from [17].

The segment angles are defined as the angle between the segments and the global x-axis (defined in Figure 2-6a), and are stored in $\boldsymbol{\psi} \equiv [\ \psi_1 \ \ \dots \ \ \psi_{N+1}\ ]^\top \in \mathbb{R}^{N+1}$. The joint angles $\boldsymbol{\phi} \equiv [\ \phi_1 \ \ \dots \ \ \phi_N\ ]^\top \in \mathbb{R}^N$ are defined according to the following geometric relation with the segment angles

$$\phi_k \equiv \psi_{k+1} - \psi_k \qquad \text{for } k \in \{1, \dots, N\}. \tag{2-5}$$

Furthermore, the average body angle $\bar{\psi}$ is defined as [17]

$$\bar{\psi} \equiv \frac{1}{N+1} \sum_{k=1}^{N+1} \psi_k. \tag{2-6}$$

The elements of $\boldsymbol{\psi}$ and $\boldsymbol{\phi}$ are defined in the domain $(-\pi, \pi]$. This implies that the average body angle $\bar{\psi}$ is defined inside this range as well. Moreover, all angles in this thesis are defined positive in the counter-clockwise direction. The x and y positions of the centers of mass of the segments, defined in the global frame, are stored in vectors $\mathbf{X} \equiv [\ x_1 \ \ \dots \ \ x_{N+1}\ ]^\top$ and $\mathbf{Y} \equiv [\ y_1 \ \ \dots \ \ y_{N+1}\ ]^\top$, respectively. As all segments are modelled with equal mass, the position of the CM of the robot is [17]

$$\mathbf{p}_{\mathrm{cm}} \equiv \begin{bmatrix} p_x \\ p_y \end{bmatrix} = \frac{1}{N+1} \begin{bmatrix} \mathbf{e}^\top \mathbf{X} \\ \mathbf{e}^\top \mathbf{Y} \end{bmatrix}. \tag{2-7}$$

The geometric relation between the segment CM positions, the body CM position and the segment angles is [17]

$$\mathbf{X} = -l\mathrm{K}^\top \cos\boldsymbol{\psi} + \mathbf{e}p_x, \tag{2-8a}$$
$$\mathbf{Y} = -l\mathrm{K}^\top \sin\boldsymbol{\psi} + \mathbf{e}p_y. \tag{2-8b}$$

Taking the first and second derivative of Eq. (2-8) with respect to time, the velocities and accelerations of the centers of mass of the segments are obtained, given below in Eq. (2-9) and (2-10), respectively [18].

$$\dot{\mathbf{X}} = l\mathrm{K}^\top \mathrm{S}_\psi \dot{\boldsymbol{\psi}} + \mathbf{e}\dot{p}_x \tag{2-9a}$$
$$\dot{\mathbf{Y}} = -l\mathrm{K}^\top \mathrm{C}_\psi \dot{\boldsymbol{\psi}} + \mathbf{e}\dot{p}_y \tag{2-9b}$$

$$\ddot{\mathbf{X}} = l\mathrm{K}^\top \left(\mathrm{C}_\psi \dot{\boldsymbol{\psi}}^2 + \mathrm{S}_\psi \ddot{\boldsymbol{\psi}}\right) + \mathbf{e}\ddot{p}_x \tag{2-10a}$$
$$\ddot{\mathbf{Y}} = l\mathrm{K}^\top \left(\mathrm{S}_\psi \dot{\boldsymbol{\psi}}^2 - \mathrm{C}_\psi \ddot{\boldsymbol{\psi}}\right) + \mathbf{e}\ddot{p}_y \tag{2-10b}$$

Furthermore, the constraints that each segment is connected to its neighboring segments via the joints provides an additional expression for the position of the CM [18].

$$\mathrm{D}\mathbf{X} + l\mathrm{A}\cos(\boldsymbol{\psi}) = \mathbf{0} \tag{2-11a}$$
$$\mathrm{D}\mathbf{Y} + l\mathrm{A}\sin(\boldsymbol{\psi}) = \mathbf{0} \tag{2-11b}$$

Again, by differentiating these equations twice with respect to time, the following equations for the segment accelerations are obtained [18].

$$\mathrm{D}\ddot{\mathbf{X}} = l\mathrm{A}\left(\mathrm{C}_\psi \dot{\boldsymbol{\psi}}^2 + \mathrm{S}_\psi \ddot{\boldsymbol{\psi}}\right) \tag{2-12a}$$
$$\mathrm{D}\ddot{\mathbf{Y}} = l\mathrm{A}\left(\mathrm{S}_\psi \dot{\boldsymbol{\psi}}^2 - \mathrm{C}_\psi \ddot{\boldsymbol{\psi}}\right) \tag{2-12b}$$

Fluid Forces and Torques

The derivations for the fluid forces and torques make use of fluid force parameters c_t, c_n and μ_n, and fluid torque parameters λ_1, λ_2 and λ_3. These parameters are expressed in terms of the geometric and fluid parameters as given below [17].

$$c_t = \frac{1}{2}\rho\pi C_f \frac{(b+a)}{2} 2l \tag{2-13}$$

$$c_n = \frac{1}{2}\rho C_D 2a2l \tag{2-14}$$

$$\mu_{\text{n}} = \rho\pi C_A a^2 2l \tag{2-15}$$

$$\lambda_1 = \frac{1}{12}\rho\pi C_M (a^2 - b^2)^2 l^3 \tag{2-16}$$

$$\lambda_2 = \frac{1}{6}\rho\pi C_f (a+b) l^3 \tag{2-17}$$

$$\lambda_3 = \frac{1}{8}\rho\pi C_f (a+b) l^4 \tag{2-18}$$

The description of the parameters can be found in Table A-1. It is worth noting that the tangential added mass parameter μ_t is approximately zero under the slender body assumption, and is therefore neglected in the derivations.

The fluid forces on each of the segments consist of two components: the added mass effect $\mathbf{f_{A_x}}$, $\mathbf{f_{A_y}}$ and the drag force. The drag force can be further subdivided into a linear $\mathbf{f}^{\mathbf{I}}_{\mathbf{D_x}}$, $\mathbf{f}^{\mathbf{I}}_{\mathbf{D_y}}$ and nonlinear part $\mathbf{f}^{\mathbf{II}}_{\mathbf{D_x}}$, $\mathbf{f}^{\mathbf{II}}_{\mathbf{D_y}}$, resulting in [17]

$$\mathbf{f} = \begin{bmatrix} \mathbf{f_x} \\ \mathbf{f_y} \end{bmatrix} = \begin{bmatrix} \mathbf{f_{A_x}} \\ \mathbf{f_{A_y}} \end{bmatrix} + \begin{bmatrix} \mathbf{f}^{\mathbf{I}}_{\mathbf{D_x}} \\ \mathbf{f}^{\mathbf{I}}_{\mathbf{D_y}} \end{bmatrix} + \begin{bmatrix} \mathbf{f}^{\mathbf{II}}_{\mathbf{D_x}} \\ \mathbf{f}^{\mathbf{II}}_{\mathbf{D_y}} \end{bmatrix}. \tag{2-19}$$

The added mass effect is governed by the added mass coefficient μ_n, and is expressed as follows [17].

$$\begin{aligned} \begin{bmatrix} \mathbf{f_{A_x}} \\ \mathbf{f_{A_y}} \end{bmatrix} = &- \begin{bmatrix} \mu_{\text{n}} \left(\text{S}_\psi\right)^2 & -\mu_{\text{n}}\text{S}_\psi\text{C}_\psi \\ -\mu_{\text{n}}\text{S}_\psi\text{C}_\psi & \mu_{\text{n}} \left(\text{C}_\psi\right)^2 \end{bmatrix} \begin{bmatrix} \ddot{\mathbf{X}} \\ \ddot{\mathbf{Y}} \end{bmatrix} \\ &- \begin{bmatrix} -\mu_{\text{n}}\text{S}_\psi\text{C}_\psi & -\mu_{\text{n}} \left(\text{S}_\psi\right)^2 \\ \mu_{\text{n}} \left(\text{C}_\psi\right)^2 & \mu_{\text{n}}\text{S}_\psi\text{C}_\psi \end{bmatrix} \begin{bmatrix} \mathbf{V}_x^a \\ \mathbf{V}_y^a \end{bmatrix} \dot{\boldsymbol{\psi}} \end{aligned} \tag{2-20}$$

Here $\mathbf{V}_x^a = \text{diag}(V_{x,1}, \ldots, V_{x,N+1})$, $\mathbf{V}_y^a = \text{diag}(V_{y,1}, \ldots, V_{y,N+1})$, with $[V_{x,i} \quad V_{y,i}]^\top$ the current velocity in the inertial frames [8].

In the drag model, the drag on each segment is governed by the normal drag coefficient c_n and tangential drag coefficient c_t [8].

$$\begin{bmatrix} \mathbf{f}^{\mathbf{I}}_{\mathbf{D_x}} \\ \mathbf{f}^{\mathbf{I}}_{\mathbf{D_y}} \end{bmatrix} = - \begin{bmatrix} c_t\text{C}_\psi & -c_n\text{S}_\psi \\ c_t\text{S}_\psi & c_n\text{C}_\psi \end{bmatrix} \begin{bmatrix} \mathbf{V_{r_x}} \\ \mathbf{V_{r_y}} \end{bmatrix}, \tag{2-21}$$

$$\begin{bmatrix} \mathbf{f}^{\mathbf{II}}_{\mathbf{D_x}} \\ \mathbf{f}^{\mathbf{II}}_{\mathbf{D_y}} \end{bmatrix} = - \begin{bmatrix} c_t\text{C}_\psi & -c_n\text{S}_\psi \\ c_t\text{S}_\psi & c_n\text{C}_\psi \end{bmatrix} \text{sgn}\left(\begin{bmatrix} \mathbf{V_{r_x}} \\ \mathbf{V_{r_y}} \end{bmatrix}\right) \begin{bmatrix} \mathbf{V}^2_{\mathbf{r_x}} \\ \mathbf{V}^2_{\mathbf{r_y}} \end{bmatrix} \tag{2-22}$$

Here vectors $\mathbf{V}_{\mathbf{r_x}}$ and $\mathbf{V}_{\mathbf{r_y}}$ contain the relative segment velocities, and are computed as

$$\begin{bmatrix} \mathbf{V}_{\mathbf{r_x}} \\ \mathbf{V}_{\mathbf{r_y}} \end{bmatrix} = \begin{bmatrix} \mathrm{C}_\psi & \mathrm{S}_\psi \\ -\mathrm{S}_\psi & \mathrm{C}_\psi \end{bmatrix} \begin{bmatrix} \dot{\mathbf{X}} - \mathbf{V}_x \\ \dot{\mathbf{Y}} - \mathbf{V}_y \end{bmatrix}. \tag{2-23}$$

Fluid torques on the segments result from segment rotations. The torque model is based on the model of a flat plate that undergoes forced angular oscillations [17], given as

$$\boldsymbol{\tau} = -\lambda_1 \ddot{\boldsymbol{\psi}} - \lambda_2 \dot{\boldsymbol{\psi}} - \lambda_3 \dot{\boldsymbol{\psi}} |\dot{\boldsymbol{\psi}}|. \tag{2-24}$$

Here, $\Lambda_1 = \lambda_1 \mathrm{I}$, $\Lambda_2 = \lambda_2 \mathrm{I}$ and $\Lambda_3 = \lambda_3 \mathrm{I}$.

Equations of Motion for the Position of the Center of Mass

Now that the expressions for the torques and forces on the segments are obtained, the equations of motion can be constructed. As mentioned at the beginning, the planar underwater snake-robot model requires the dynamics of the position of the CM and the segment angles. To start with the former, the acceleration of the CM of the robot is obtained by differentiating Eq. (2-7) twice with respect to time [18].

$$\ddot{\mathbf{p}}_{\mathrm{cm}} = \frac{1}{N+1} \begin{bmatrix} \mathbf{e}^\top \ddot{\mathbf{X}} \\ \mathbf{e}^\top \ddot{\mathbf{Y}} \end{bmatrix} \tag{2-25}$$

The acceleration of the CM of the segments can be obtained from the segment force balance equations, which are written in vector form as [17]

$$m\ddot{\mathbf{X}} = \mathrm{D}^\top \mathbf{h}_\mathbf{x} + \mathbf{f}_\mathbf{x}, \tag{2-26a}$$

$$m\ddot{\mathbf{Y}} = \mathrm{D}^\top \mathbf{h}_\mathbf{y} + \mathbf{f}_\mathbf{y}. \tag{2-26b}$$

Here $\mathbf{f} \equiv [\ \mathbf{f}_\mathbf{x} \quad \mathbf{f}_\mathbf{y}\ ]^\top$ is as defined in Eq. (2-19), and $\mathbf{h}_\mathbf{x}$ and $\mathbf{h}_\mathbf{y}$ are the x and y components of the constraint forces. Isolating $\ddot{\mathbf{X}}$ and $\ddot{\mathbf{Y}}$, substituting them into Eq. (2-25) and noticing that $\mathbf{e}^\top \mathrm{D}^\top = \mathbf{0}$ (i.e. the constraint forces cancel each other out as expected) gives [17]

$$\ddot{\mathbf{p}}_{\mathbf{cm}} = \frac{1}{(N+1)m} \begin{bmatrix} \mathbf{e}^\top & \mathbf{0}_{1\times(N+1)} \\ \mathbf{0}_{1\times(N+1)} & \mathbf{e}^\top \end{bmatrix} \mathbf{f}. \tag{2-27}$$

This equation essentially states that the acceleration equals the sum of external forces divided by the total mass of the robot. By substituting $\mathbf{f}$ from Eq. (2-19) in this equation, and subsequently substituting $\ddot{\mathbf{X}}$ and $\ddot{\mathbf{Y}}$ from Eq. (2-10) and $\mathbf{f}_{\mathbf{Ax}}$ from Eq. (2-20) into the result, the final expression for $\ddot{\mathbf{p}}_{\mathbf{cm}}$ is obtained [18].

$$\begin{aligned}\ddot{\mathbf{p}}_{\mathbf{cm}} \equiv \begin{bmatrix} \ddot{p}_x \\ \ddot{p}_y \end{bmatrix} = &- \mathrm{M_p} \begin{bmatrix} \mathbf{k}_{11} & \mathbf{k}_{12} \\ \mathbf{k}_{21} & \mathbf{k}_{22} \end{bmatrix} \begin{bmatrix} l\mathrm{K}^\top \left(\mathrm{C}_\psi \dot{\boldsymbol{\psi}}^2 + \mathrm{S}_\psi \ddot{\boldsymbol{\psi}}\right) \\ l\mathrm{K}^\top \left(\mathrm{S}_\psi \dot{\boldsymbol{\psi}}^2 - \mathrm{C}_\psi \ddot{\boldsymbol{\psi}}\right) \end{bmatrix} \\ &- \mathrm{M_p} \begin{bmatrix} \mathbf{k}_{12} & -\mathbf{k}_{11} \\ \mathbf{k}_{22} & -\mathbf{k}_{21} \end{bmatrix} \begin{bmatrix} \mathbf{V}_x^a \\ \mathbf{V}_y^a \end{bmatrix} \dot{\boldsymbol{\psi}} + \mathrm{M_p} \begin{bmatrix} \mathbf{e}^\top \mathbf{f_{Dx}} \\ \mathbf{e}^\top \mathbf{f_{Dy}} \end{bmatrix}\end{aligned} \tag{2-28}$$

Here, $\mathbf{f_{Dx}} = \mathbf{f}^{\mathbf{I}}_{\mathbf{D_x}} + \mathbf{f}^{\mathbf{II}}_{\mathbf{D_x}}$ and $\mathbf{f_{Dy}} = \mathbf{f}^{\mathbf{I}}_{\mathbf{D_y}} + \mathbf{f}^{\mathbf{II}}_{\mathbf{D_y}}$, and matrix $\mathrm{M_p}$ and vectors $\mathbf{k}_{11}$, $\mathbf{k}_{12}$, $\mathbf{k}_{21}$ and $\mathbf{k}_{22}$ are defined as

$$\mathrm{M_p} \equiv \begin{bmatrix} \mathbf{m}_{11} & \mathbf{m}_{12} \\ \mathbf{m}_{21} & \mathbf{m}_{22} \end{bmatrix} \equiv \begin{bmatrix} (N+1)m + \mathbf{e}^\top \mu_\mathrm{n} \mathrm{S}_\psi^2 \mathbf{e} & -\mathbf{e}^\top \mu_\mathrm{n} \mathrm{S}_\psi \mathrm{C}_\psi \mathbf{e} \\ -\mathbf{e}^\top \mu_\mathrm{n} \mathrm{S}_\psi \mathrm{C}_\psi \mathbf{e} & (N+1)m + \mathbf{e}^\top \mu_\mathrm{n} \mathrm{C}_\psi^2 \mathbf{e} \end{bmatrix}^{-1}, \tag{2-29}$$

$$\begin{bmatrix} \mathbf{k}_{11} & \mathbf{k}_{12} \\ \mathbf{k}_{21} & \mathbf{k}_{22} \end{bmatrix} \equiv \begin{bmatrix} \mathbf{e}^\top \mu_\mathrm{n} \mathrm{S}_\psi^2 & -\mathbf{e}^\top \mu_\mathrm{n} \mathrm{S}_\psi \mathrm{C}_\psi \\ -\mathbf{e}^\top \mu_\mathrm{n} \mathrm{S}_\psi \mathrm{C}_\psi & \mathbf{e}^\top \mu_\mathrm{n} \mathrm{C}_\psi^2 \end{bmatrix}. \tag{2-30}$$

Equations of Motion for the Segment Angles

The torque balance equations of the segments are described as [17]

$$j\ddot{\psi}_1 = u_1 \qquad - l \sin\psi_1 \left(h_{x,1}\right) + l \cos\psi_k \left(h_{y,k}\right) + \tau_1, \tag{2-31a}$$

$$j\ddot{\psi}_k = u_k - u_{k-1} - l \sin\psi_k \left(h_{x,k} + h_{x,k-1}\right) + l \cos\psi_k \left(h_{y,k} + h_{y,k-1}\right) + \tau_k \quad \text{for } k \in \{2, \ldots, N\}, \tag{2-31b}$$

$$j\ddot{\psi}_{N+1} = \qquad - u_N \quad - l \sin\psi_{N+1} \left(h_{x,N}\right) + l \cos\psi_{N+1} \left(h_{y,N}\right) + \tau_{N+1}. \tag{2-31c}$$

Looking at Eq. (2-31b), the first and second terms on the right hand side are the effect of the torques generated by the motors in joints k and $k-1$. The last term is the effect of the fluid torques on the segment, which is the k^th element of $\boldsymbol{\tau}$ in Eq. (2-24). The third and fourth terms are the effect of the x and y component of the constraint forces $h_{x,k}$ and $h_{y,k}$, which are the k^th components of Eq. (2-33).

Eq. (2-31) can be expressed in vector form as follows [17].

$$\mathrm{J}\ddot{\psi} = \mathrm{D}^\top \mathbf{u} - l\mathrm{S}_\psi \mathrm{A}^\top \mathbf{h}_x + l\mathrm{C}_\psi \mathrm{A}^\top \mathbf{h}_y + \boldsymbol{\tau} \tag{2-32}$$

The x and y components of the constraint forces, $\mathbf{h_x}$ and $\mathbf{h_y}$, are obtained by isolating them from Eq. (2-26) and writing out the added mass effect in Eq. (2-20). This results in [17, 18]

$$\begin{aligned}\mathbf{h}_x = &\left(\mathrm{D}\mathrm{D}^\top\right)^{-1} \mathrm{D} \Big(m\ddot{\mathbf{X}} + \mu_\mathrm{n} \left(\mathrm{S}_\psi\right)^2 \ddot{\mathbf{X}} - \mu_\mathrm{n} \mathrm{S}_\psi \mathrm{C}_\psi \ddot{\mathbf{Y}} \\ &-\mu_\mathrm{n} \mathrm{S}_\psi \mathrm{C}_\psi \mathbf{V}_x^a \dot{\psi} - \mu_\mathrm{n} \left(\mathrm{S}_\psi\right)^2 \mathbf{V}_y^a \dot{\psi} - \mathbf{f}^{\mathbf{I}}_{\mathbf{D_x}} - \mathbf{f}^{\mathbf{II}}_{\mathbf{D_x}}\Big),\end{aligned} \tag{2-33a}$$

$$\begin{aligned}\mathbf{h}_y = &\left(\mathrm{D}\mathrm{D}^\top\right)^{-1} \mathrm{D} \Big(m\ddot{\mathbf{Y}} - \mu_\mathrm{n} \mathrm{S}_\psi \mathrm{C}_\psi \ddot{\mathbf{X}} + \mu_\mathrm{n} \left(\mathrm{C}_\psi\right)^2 \ddot{\mathbf{Y}} \\ &+\mu_\mathrm{n} \left(\mathrm{C}_\psi\right)^2 \mathbf{V}_x^a \dot{\psi} + \mu_\mathrm{n} \mathrm{S}_\psi \mathrm{C}_\psi \mathbf{V}_y^a \dot{\psi} - \mathbf{f}^{\mathbf{I}}_{\mathbf{D_y}} - \mathbf{f}^{\mathbf{II}}_{\mathbf{D_y}}\Big).\end{aligned} \tag{2-33b}$$

Eq. (2-33) can be rewritten by substituting $\mathrm{D}\ddot{\mathbf{X}}$ and $\mathrm{D}\ddot{\mathbf{Y}}$ with Eq. (2-12b). Furthermore, $\ddot{\mathbf{X}}$ and $\ddot{\mathbf{Y}}$ are substituted with Eq. (2-10), and subsequently $\ddot{p}_x$ and $\ddot{p}_y$ in Eq. (2-10) are replaced by Eq. (2-28).

Substituting the result of this into Eq. (2-32), together the previously obtained expression for $\boldsymbol{\tau}$ in Eq. (2-24), the derivation arrives at the final expression for the equations of motion of $\boldsymbol{\psi}$, given as [18]

$$\mathrm{M}_\psi \ddot{\boldsymbol{\psi}} + \mathrm{W}_\psi \dot{\boldsymbol{\psi}}^2 + \mathrm{V}_\psi \dot{\boldsymbol{\psi}} + \Lambda_3 |\dot{\boldsymbol{\psi}}| \dot{\boldsymbol{\psi}} + \mathrm{K}_{\mathrm{D_x}} \mathbf{f}_{\mathbf{D_x}} + \mathrm{K}_{\mathrm{D_y}} \mathbf{f}_{\mathbf{D_y}} = \mathrm{D}^\top \mathbf{u}. \tag{2-34}$$

The definitions of matrices M_ψ, W_ψ, V_ψ, $\mathrm{K}_{\mathrm{D_x}}$ and $\mathrm{K}_{\mathrm{D_y}}$ are given below [18].

$$\mathrm{M}_\psi \equiv \mathrm{J} + ml^2 \mathrm{S}_\psi \mathrm{V} \mathrm{S}_\psi + ml^2 \mathrm{C}_\psi \mathrm{V} \mathrm{C}_\psi + \Lambda_1 + l^2 \mu_\mathrm{n} \mathrm{K}_1 \mathrm{K}^\top \mathrm{S}_\psi + l^2 \mu_\mathrm{n} \mathrm{K}_2 \mathrm{K}^\top \mathrm{C}_\psi \tag{2-35}$$

$$\mathrm{W}_\psi \equiv l^2 \mathrm{S}_\psi \mathrm{V} \mathrm{C}_\psi - ml^2 \mathrm{C}_\psi \mathrm{V} \mathrm{S}_\psi + l^2 \mu_\mathrm{n} \mathrm{K}_1 \mathrm{K}^\top \mathrm{C}_\psi - l^2 \mu_\mathrm{n} \mathrm{K}_2 \mathrm{K}^\top \mathrm{S}_\psi \tag{2-36}$$

$$\mathrm{V}_\psi \equiv \Lambda_2 - l\mu_\mathrm{n} \mathrm{K}_2 \mathrm{V}_x^a - l\mu_\mathrm{n} \mathrm{K}_1 \mathrm{V}_y^a \tag{2-37}$$

$$\mathrm{K}_{\mathrm{D_x}} \equiv \mu_\mathrm{n} \mathbf{m}_{11} \mathrm{A}_1 \mathbf{e}\mathbf{e}^\top - l\mu_\mathrm{n} \mathbf{m}_{21} \mathrm{A}_2 \mathbf{e}\mathbf{e}^\top - l \mathrm{S}_\psi \mathrm{K} \tag{2-38}$$

$$\mathrm{K}_{\mathrm{D_y}} \equiv \mu_\mathrm{n} \mathbf{m}_{12} \mathrm{A}_1 \mathbf{e}\mathbf{e}^\top - l\mu_\mathrm{n} \mathbf{m}_{22} \mathrm{A}_2 \mathbf{e}\mathbf{e}^\top + l \mathrm{C}_\psi \mathrm{K} \tag{2-39}$$

Here,

$$\mathrm{K}_1 \equiv \mathrm{A}_1 + \mu_\mathrm{n} \mathrm{A}_1 \mathbf{e}\mathbf{e}^\top \left(\mathbf{m}_{12} \mathrm{S}_\psi \mathrm{C}_\psi - \mathbf{m}_{11} \mathrm{S}_\psi^2 \right) - \mu_\mathrm{n} \mathrm{A}_2 \mathbf{e}\mathbf{e}^\top \left(\mathbf{m}_{22} \mathrm{S}_\psi \mathrm{C}_{\boldsymbol{\psi}} - \mathbf{m}_{21} \mathrm{S}_\psi^2 \right), \tag{2-40}$$

$$\mathrm{K}_2 \equiv \mathrm{A}_2 - \mu_\mathrm{n} \mathrm{A}_1 \mathbf{e}\mathbf{e}^\top \left(\mathbf{m}_{11} \mathrm{S}_\psi \mathrm{C}_\psi - \mathbf{m}_{12} \mathrm{C}_\psi^2 \right) + \mu_\mathrm{n} \mathrm{A}_2 \mathbf{e}\mathbf{e}^\top \left(\mathbf{m}_{21} \mathrm{S}_\psi \mathrm{C}_\psi - \mathbf{m}_{22} \mathrm{C}_\psi^2 \right), \tag{2-41}$$

$$\mathrm{A}_1 \equiv \mathrm{S}_\psi \mathrm{K} \mathrm{S}_\psi^2 + \mathrm{C}_\psi \mathrm{K} \mathrm{S}_\psi \mathrm{C}_\psi, \tag{2-42}$$

$$\mathrm{A}_2 \equiv \mathrm{S}_\psi \mathrm{K} \mathrm{S}_\psi \mathrm{C}_\psi + \mathrm{C}_\psi \mathrm{K} \mathrm{C}_\psi^2. \tag{2-43}$$

Chapter 3

Head Stabilization in a Lateral Undulation Gait

This chapter focuses on generating the reference signals for lateral undulations with the Ijspeert model, and achieving head stabilization in the lateral undulation gait. The head stabilization method is build upon the Ijspeert model, and requires the model to generate desirable reference signals. Therefore, Section 3-1 starts with formulating the objectives for the desired lateral undulation gait, and shows that this gait achieved under certain conditions. After that, Section 3-2 formalizes the head stabilization control objective and provides conditions for which this objective is achieved. The methods to generate lateral undulations and achieve head stabilization are verified with simulations, of which the results are presented in Section 3-3. Last, the results are discussed in Section 3-4.

3-1 Ijspeert Model Analysis

The goal of this section is to determine under what conditions the Ijspeert model produces a desirable lateral undulation gait. In Section 3-1-1, the objectives for this desired gait are formulated. After that, Section 3-1-2 shows that these objectives are achieved for the imposed parameter restrictions and restrictions on the initial conditions.

3-1-1 Lateral Undulation Gait

The Ijspeert model is governed by five parameters that are given in Section 1-2-3, which shape the output signals of the model. Not all parameter settings in the original Ijspeert model in Eq. (1-2) actually make the Ijspeert model produce desirable reference signals. The goal of analysing the Ijspeert model is to ensure that the model produces a desirable gait. To do so, the definition of a desired gait is given first.

The first requirement is that the reference signals should produce lateral undulations in order to propel the body. Such reference signals are obtained when the oscillators are synchronized in frequency, and have a nonzero phase difference between them. The second requirement is to make that nonzero phase differences asymptotically converge the phase bias terms $\gamma_{k,k+1}$, making the phase bias terms explicit control parameters for the assymptotic phase differences. This is convenient for control purposes, and is required for the head stabilization method in Section 3-2-2.

Consider the Ijspeert model in Eq. (1-6). The phase and frequency of the output of oscillator k are determined by the phase dynamics of the oscillator, where the phase equals θ_k and the frequency equals $\dot{\theta}_k$. First, the phase dynamics in Eq. (1-6) are rewritten as

$$\begin{aligned}
\dot{\theta}_1 &= \omega + w\sin(\theta_2 - \theta_1 - \gamma_{2,1}) && \text{for } k = 1, && \text{(3-1a)}\\
\dot{\theta}_k &= \omega + w\sin(\theta_{k-1} - \theta_k - \gamma_{k-1,k}) \\
&\quad + w\sin(\theta_{k+1} - \theta_k - \gamma_{k+1,k}) && \text{for } k \in \{2, \dots, N-1\}, && \text{(3-1b)}\\
\dot{\theta}_N &= \omega + w\sin(\theta_{N-1} - \theta_N - \gamma_{N-1,N}) && \text{for } k = N. && \text{(3-1c)}
\end{aligned}$$

Since the phase biases adhere to the restrictions in Eq. (1-3), the objectives for the lateral undulation gait (frequency synchronization and asymptotic phase difference equal to the phase bias) are captured in the following equations.

$$\lim_{t\to\infty} \dot{\theta}_k - \dot{\theta}_l = 0 \qquad \forall k, l \in \Big\{\{1, \dots, N\} \;\Big|\; |k-l| = 1\Big\} \tag{3-2}$$

$$\lim_{t\to\infty} \theta_k - \theta_l = \gamma_{kl} + n_{kl}\ 2\pi \qquad n_{kl} \in \mathbb{Z}, \quad \forall k, l \in \Big\{\{1, \dots, N\} \;\Big|\; |k-l| = 1\Big\} \tag{3-3}$$

3-1-2 Synchronization in the Ijspeert Model

The goal of this section is to show that the objectives for the lateral undulation gait given in Eq. (3-2) and (3-3) hold in the chain of Ijspeert oscillators in Eq. (1-6) for certain restrictions on the initial conditions.

In [14] is shown that, in a network of Ijspeert oscillators with dynamics given in Eq. (1-6) where the phase bias parameters γ_{lk} are consistent, the phases of the oscillators synchronize in frequency, and the phase difference between each two connected oscillators asymptotically converge to

$$\lim_{t\to\infty} \theta_l - \theta_k = \gamma_{lk}. \tag{3-4}$$

In a chain network, the restriction in Eq. (1-3) is sufficient to guarantee that the parameters γ_{lk} are consistent, i.e. the sum of $\gamma_{k,k+1}$ in the Ijspeert network in Figure 1-1 is a multiple of 2π over any closed path [14]. Therefore, the objectives in Eq. (3-2) and (3-3) are achieved.

In the remainder of this section, an alternative proof is presented to show that the oscillators in the Ijspeert model in Eq. (1-6) synchronize in frequency, and that the phase differences in the Ijspeert model converge to the phase bias terms. This is done by representing the phase dynamics of the Ijspeert network as the network of Kuramoto oscillators described in Eq. (2-3), using the coordinate change in Eq. (2-2) (see Section 2-2-2). The lateral undulation gait objectives in Eq. (3-2) and (3-3) are rewritten in terms of the states of the Kuramoto model using Eq. (2-2).

$$\lim_{t\to\infty} \dot{\vartheta}_k - \dot{\vartheta}_l = 0 \qquad \forall k, l \in \Big\{\{1,\dots,N\} \;\Big|\; |k-l| = 1\Big\} \tag{3-5}$$

$$\lim_{t\to\infty} \vartheta_k - \vartheta_l = n_{kl}\, 2\pi \qquad n_{kl} \in \mathbb{Z} \tag{3-6}$$

In new coordinate frame, the latter objective is called phase synchronization. Using the description of the phase dynamics in Eq. (2-3), Theorem 1 shows that, for certain initialization restrictions, the states ϑ_k converge to the phase synchronized solutions in the limit, i.e. the control objectives in Eq. (3-5) and (3-6) are achieved.

Theorem 1 (Convergence of the unperturbed Kuramoto model [15])**.** *"Consider the unperturbed Kuramoto model*[1] *Eq. (2-3) defined over an arbitrary connected graph with incidence matrix B. For any value of the coupling $\mathrm{w} > 0$ and for almost all initial conditions starting in $(-\pi,\pi)^N$*[2]*, the phase differences will go to an even multiple of 2π, i.e., the oscillators will synchronize."*

Theorem 1 about the convergence of the phase differences of the Kuramoto model is now used to obtain the convergence of the phase differences of the Ijspeert model. Using Eq. (2-2), the restrictions on the initial phases ϑ_k in Theorem 1 are written in terms of the original phases θ_k as

$$\theta_k(0) + \sum_{l=k}^{N-1} \gamma_{l,l+1} \in (-\pi,\pi) \qquad \forall k \in \{1,\dots,N-1\}, \tag{3-7a}$$

$$\theta_N(0) \in (-\pi,\pi). \tag{3-7b}$$

The initial phases ϑ_k only converge to zero when they do not start in the unstable equilibrium [15]. This is written in terms of θ_k as

$$\begin{aligned} &\theta_k(0) - \theta_l(0) - \gamma_{kl} \neq (2n_{kl}+1)\pi, \\ &\forall k, l \in \{1,\dots,N\}, |k-l| = 1, n_{kl} \in \mathbb{Z}. \end{aligned} \tag{3-8}$$

Using Eq. (3-7) and (3-8) and Assumption 1.1, the convergence of the phase differences of the Ijspeert model is given by Lemma 1.1.

---

[1] The unperturbed Kuramoto model refers to the Kuramoto model with equal exogenous frequencies.

[2] The initial conditions that do not converge to the synchronized states are equal to the unstable equilibrium points. Therefore, unless the initial conditions exactly equals an unstable equilibrium, the trajectories converge to the frequency and phase synchronized states.

Assumption 1.1. *The initial conditions for the states in the Ijspeert model in Eq. (1-6) obey the restrictions in Eq. (3-7) and (3-8).*

Lemma 1.1. *Consider the Ijspeert model in Eq. (1-6) with phase bias parameters adhering to Eq. (1-3) and with coupling weight* $w > 0$*. Under Assumption 1.1, the phase differences converge according to Eq. (3-2) and (3-3).*

Proof. With the phase difference parameters adhering to Eq. (1-3), the Ijspeert model in Eq. (1-6) can be rewritten as the Kuramoto model in Eq. (2-1) using the coordinate change in Eq. (2-2). With the same coordinate change, the initialization restrictions on θ_k in Eq. (3-7) and (3-8) can be shown to be equivalent to the initialization restrictions on ϑ_k in Theorem 1. Therefore, under Assumption 1.1, the restrictions on ϑ_k in Theorem 1 are met. Furthermore, the condition on the coupling weight parameter in Theorem 1 is equivalent to Eq. (1-5).

With all conditions of Theorem 1 being met, the theorem is applied to find that the oscillators in Eq. (2-1) synchronize in phase, i.e. Eq. (3-5) and (3-6) are achieved. These equations can be shown to be equivalent to Eq. (3-2) and (3-3) using Eq. (2-2). This concludes the proof.

□

3-2 Head Stabilization

The goal of this section is to design a method to stabilize the head of a robotic lamprey using the Ijspeert model for the generation of reference signals for a lateral undulation gait. In Section 3-2-1, the problem of head stabilization in the lateral undulation gait is formalized. Thereafter, the head stabilization method is described in Section 3-2-2.

3-2-1 Head Stabilization Problem

The goal of the head stabilization method is to reduce the distortions of the visual inputs by mitigating the effect of the lateral undulations on the the movements of the head. This is approached by aligning the head segment with some direction that remains reasonably fixed. This criterion is defined somewhat loosely, which has the following reason. A perfectly fixed direction is not desirable here, as the head needs to be able to turn with the body. The average body direction is the direction of choice that meets this criterion, and has the advantage of directing the head approximately in the direction of motion. This alignment strategy is referred to as head-body alignment.

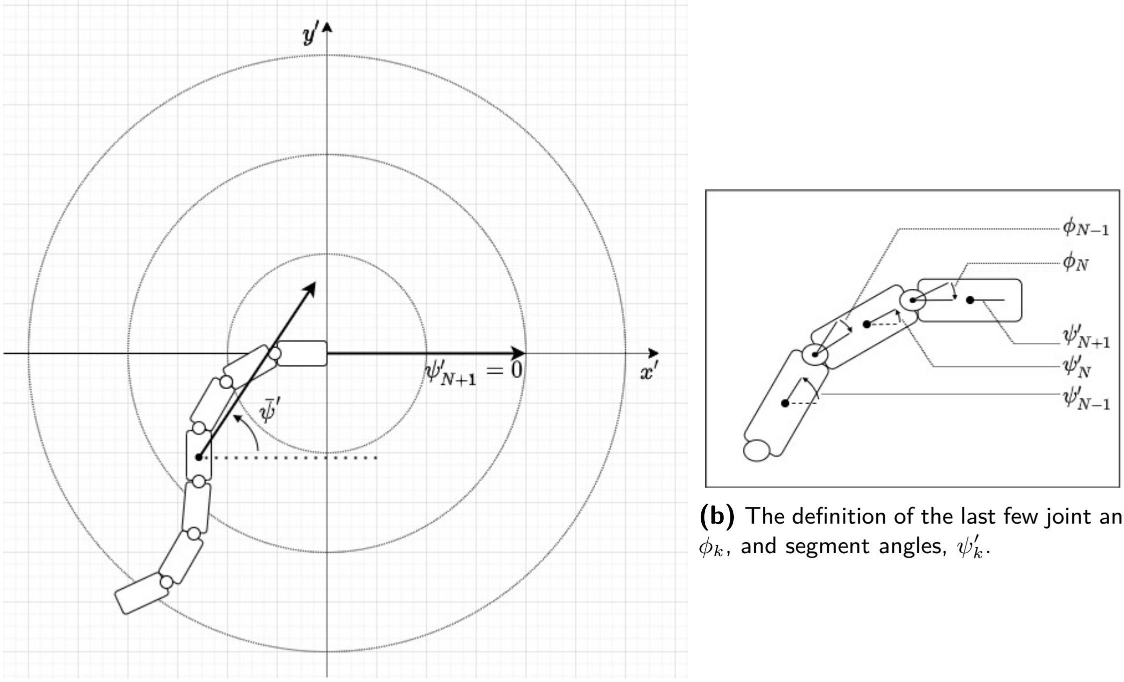

(a) The definitions of the head segment angle, $\psi'_{N+1} = 0$, and the average body angle, $\bar{\psi}'$.

(b) The definition of the last few joint angles, ϕ_k, and segment angles, ψ'_k.

Figure 3-1: Definitions of kinematic variables in the head fixed polar coordinate frame.

To express the head stabilization control objectives in terms of the kinematic variables of the robot, it is convenient to consider the head fixed polar coordinate frame shown in Figure 3-1a. The relation between the segment angles in this frame, ψ'_k, and those in the global frame in Figure 2-6, ψ_k, is

$$\psi'_k = \psi_k - \psi_{N+1}. \tag{3-9}$$

The head segment angle ψ'_{N+1} is zero in this coordinate frame, and the head-body alignment error $\bar{\psi}'$ is the average angle of the body as measured in this coordinate frame (see Eq. (2-6)). Using this error, the head-body alignment problem in the head fixed polar coordinate frame is visualized in Figure 3-2, and the control objective is written as

$$\lim_{t \to \infty} \bar{\psi}' = 0 \qquad \text{with} \tag{3-10a}$$

$$\bar{\psi}' = \frac{1}{N+1} \sum_{s=1}^{N+1} \psi'_s. \tag{3-10b}$$

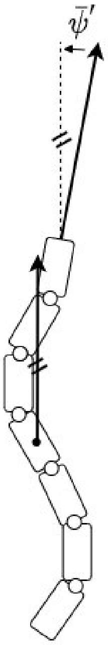

Figure 3-2: Schematic of the head stabilization problem.

Eq. (3-10b) is not useful in this form because the angles ψ'_s are not known to the robot. Therefore, the joint angles are first written in terms of the measurable joint angles ϕ_k. The angles in the following derivations are visualized in Figure 3-1.

$$
\begin{aligned}
\psi'_N &= \psi'_{N+1} - \phi_N && \text{(3-11a)}\\
\psi'_{N-1} &= \psi'_N - \phi_{N-1} &&\\
&= \psi'_{N+1} - \phi_{N-1} - \phi_N && \text{(3-11b)}\\
&\vdots &&\\
&\Downarrow &&\\
\psi'_s &= \psi'_{N+1} - \sum_{k=s}^{N} \phi_k \qquad \text{for } s \in \{1, \dots, N\} && \text{(3-11c)}
\end{aligned}
$$

In these equations, $\psi'_{N+1} = 0$ by definition of the coordinate frame. By combining Eq. (3-11c) with Eq. (3-10b), the following expressions are obtained.

$$
\begin{aligned}
\bar{\psi}' &= \frac{1}{N+1}\left(\psi'_{N+1} + \sum_{s=1}^{N} \psi'_s\right) && \text{(3-12a)}\\
&= -\frac{1}{N+1}\sum_{s=1}^{N}\sum_{k=s}^{N} \phi_k && \text{(3-12b)}\\
&= -\frac{1}{N+1}\sum_{k=1}^{N} k\phi_k && \text{(3-12c)}
\end{aligned}
$$

The latter expression replaces Eq. (3-10b) to express the head stabilization objective in terms of the joint angles. This results in the head-body alignment objective expressed in terms of the joint angles ϕ_k.

This objective can be simplified by assuming that the motor dynamics are instantaneous such that $\phi_k = \phi_{\text{ref},k}\ \forall k \in \{1, \dots, N\}$. This means the motor dynamics and intricate fluid dynamics can be neglected, and only the reference signals need to be investigated. If $\bar{\psi}'_{\text{ref}}$ is defined as the average body angle when all joint angles equal their reference signals, the control objective in Eq. (3-10) and the result in Eq. (3-12c) can be rewritten as

$$
\begin{aligned}
\lim_{t\to\infty} \bar{\psi}'_{\text{ref}} &= 0 \qquad \text{with} && \text{(3-13a)}\\
\bar{\psi}'_{\text{ref}} &= \frac{1}{N+1}\sum_{k=1}^{N} k\phi_{\text{ref},k}. && \text{(3-13b)}
\end{aligned}
$$

If this control objective is achieved, the original objective in Eq. (3-10a) is also achieved since $\bar{\psi}' = \bar{\psi}'_{\text{ref}}$ under the instant motor assumption. In reality, non instant motor dynamics will result in $\bar{\psi}' \approx \bar{\psi}'_{\text{ref}}$, where the closeness of the approximate equality depends on how fast the motor dynamics are.

3-2-2 Head Stabilization Method

This section first presents the head stabilization method. This method is build upon Proposition 1, of which the derivation is given in the remaining part of the section. The algorithm for the head stabilization method is presented in Algorithm 1 in Appendix B.

The head stabilization method is approached by locally modifying the Ijspeert model to alter the generation of $\phi_{\text{ref},N}$. This way, the reference signals for the other joints remain available for the lateral undulations, as naturally the head stabilization method is not useful when the motion of the robot is restricted. This approach also makes it possible to treat the stabilization and lateral undulation problems separately. As explained in Section 3-2-1, the assumption is made that the motor dynamics are instant, such that the control objective for head stabilization is given in Eq. (3-13).

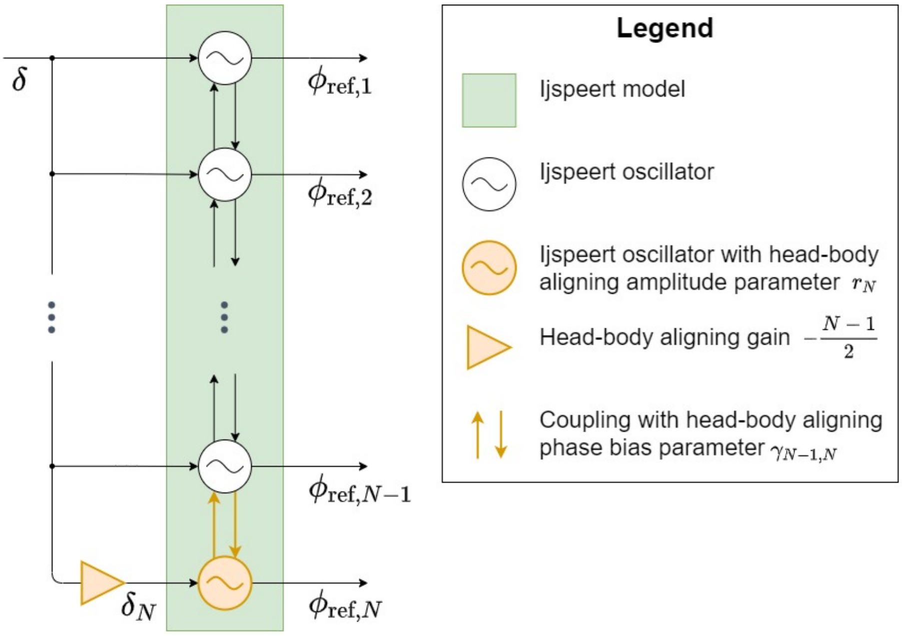

Figure 3-3: System description of the head stabilized Ijspeert model. For a comparison with the original Ijspeert model, see Figure 1-1.

The basis for the head stabilization method is the Ijspeert model in Eq. (1-6) with initial conditions inside the allowed ranges derived in Section 3-1-2 (i.e. Assumption 1.1 holds), such that the lateral undulation control objectives are achieved. Furthermore, the Ijspeert model parameters $r_1, \ldots, r_{N-1}$ and $\gamma_{1,2}, \ldots, \gamma_{N-2,N-1}$, are assumed to be constant and known before the run. The turning control parameters $\delta_1, \ldots, \delta_{N-1}$ are assumed to be available to the head oscillator during the entire run.

Under the above mentioned conditions, Proposition 1 states that, if the Ijspeert model in Eq. (1-6) is used with parameters r_N, $\gamma_{N-1,N}$ and δ_N set according to Eq. (3-32) to (3-34), the reference signals from the Ijspeert model asymptotically converge to a head stabilized lateral undulation gait and the head stabilization control objective in Eq. (3-13) is achieved. The gait of the robot is head stabilized under the assumption that the motor dynamics are instant. Parameters r_N and $\gamma_{N-1,N}$ depend on the constant parameters $r_1, \dots, r_{N-1}$ and $\gamma_{1,2}, \dots, \gamma_{N-2,N-1}$. Under the assumption that these parameters are constant and known on forehand, the head stabilizing parameter values for r_N and $\gamma_{N-1,N}$ are constant and can be computed and implemented in the Ijspeert model before the run.

The system description of the head stabilized Ijspeert model is given in Figure 3-3. The figure shows the special case of $\delta_1, \dots, \delta_{N-1} = \delta$ as this case applies in Section 4-2, although the head stabilization method can also be applied to the more general case when $\delta_1, \dots, \delta_{N-1}$ are not equal. The parameter δ_N is inversely proportional to δ according to Eq. (3-21), and can be computed online using a gain of $-\frac{N-1}{2}$.

In the remainder of this section the derivation of Proposition 1 is provided. The reasoning behind the proof of this proposition is best explained using the system schematic in Figure 3-4. Note that the yellow block in this figure does not represent an actual subsystem in the robotic lamprey, but is rather an auxiliary subsystem to obtain the error signal $\bar{\psi}'_{\text{ref}}$. The figure illustrates how the Ijspeert model in Eq. (1-6) is split up into two parts: $f(\boldsymbol{\theta})$ and $g(\boldsymbol{\theta})$. The function $f(\boldsymbol{\theta})$ contains the phase dynamics, and is given in the first line of Eq. (1-6). The function $g(\boldsymbol{\theta})$ maps the phases to the outputs $\boldsymbol{\phi}_{\text{ref}}$, and is given in the second line of Eq. (1-6). Furthermore, the function $h(\boldsymbol{\phi}_{\text{ref}})$ is given in Eq. (3-13), and maps $\boldsymbol{\phi}_{\text{ref}}$ to the error signal $\bar{\psi}'_{\text{ref}}$. By representing the system like this, the dynamics and mapping functions are split from each other and can be treated separately. The limit behaviour of the dynamic part, $\dot{\boldsymbol{\theta}} = f(\boldsymbol{\theta})$, is analysed in Section 3-1-2. This analysis is used to deduce what the limit behaviour of the error signal $\bar{\psi}'_{\text{ref}}$ must be by analysing the mapping functions $g(\boldsymbol{\theta})$ and $h(\boldsymbol{\theta})$ in this section.

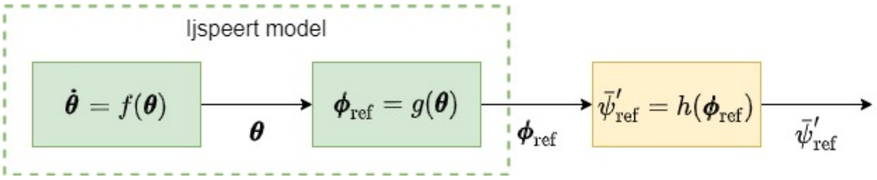

Figure 3-4: The system schematic used for the derivation of the head stabilization method.

Before presenting the final result, we first provide three steps which are required to derive the conditions to achieve head stabilization. First, the error term $\bar{\psi}'_{\text{ref}}$ is expressed in terms of the phases and phase differences of the Ijspeert model. In the first step, this is done for the Ijspeert model without turning, i.e. $\delta_k = 0 \ \forall k \in \{1, \dots, N\}$. In the second step, turning is included by considering arbitrary values for $\delta_k \ \forall k \in \{1, \dots, N-1\}$. The error term in the second case is the most general as it includes turning, and is therefore used in Proposition 1. The third step applies Lemma 1.1 to obtain the limits of the phase differences, which are used to obtain the limits of two functions inside the error term. After the three steps, the proof of Proposition 1 shows that the error term converges to a constant value that depends on the parameters $r_1, \dots, r_N$, $\gamma_{1,2}, \dots, \gamma_{N-1,N}$ and $\delta_1, \dots, \delta_N$. This value is then shown to equal zero by choosing parameters r_N, $\gamma_{N-1,N}$ and δ_N as certain functions of the other parameters.

Error Term without Turning

To simplify the derivations, the Ijspeert model is first considered without turning, i.e. $\delta_k = 0 \; \forall k \in \{1, \dots, N\}$. Eq. (3-13b) is rewritten as follows.

$$\bar{\psi}'_{\text{ref}} = -\frac{1}{N+1} \sum_{k=1}^{N} k \phi_{\text{ref},k} \tag{3-14a}$$

$$= -\frac{N}{N+1} \left(\phi^* + \phi_{\text{ref},N}\right) \qquad \text{with} \tag{3-14b}$$

$$\phi^* = \sum_{k=1}^{N-1} \frac{k}{N} \phi_{\text{ref},k} \tag{3-14c}$$

The effect of the outputs of oscillators $1, \dots, N-1$ on the error is combined in the function ϕ^*. The goal is now to express this term as a single trigonometric function, such that it can be compared to $\phi_{\text{ref},N}$ in the limit. To continue, ϕ^* is expressed in terms of the phase variable θ_{N-1} and the phase differences Θ_k, with $\Theta_k \equiv \theta_k - \theta_{k+1}$ for $k \in \{1, \dots, N-1\}$. The expression for $\phi_{\text{ref},k}$ from Eq. (1-6) is substituted into Eq. (3-14c), where the turning parameters δ_k are set to zero.

$$\phi^* = \sum_{k=1}^{N-1} \frac{k}{N} r_k \cos(\theta_k) \tag{3-15a}$$

$$\begin{aligned} = \; & \frac{N-1}{N} r_{N-1} \cos(\theta_{N-1}) \\ & + \frac{N-2}{N} r_{N-2} \cos(\theta_{N-1} + \Theta_{N-2}) \\ & + \frac{N-3}{N} r_{N-3} \cos(\theta_{N-1} + \Theta_{N-2} + \Theta_{N-3}) \\ & + \dots \end{aligned} \tag{3-15b}$$

The terms dependent on θ_{N-1} and the ones dependent on Θ_k are separated by using the trigonometric identity $\cos(p+q) = \cos(p)\cos(q) - \sin(p)\sin(q)$ where $p = \theta_{N-1}$ and q is the sum over Θ_k.

$$\begin{aligned} \phi^* = \; & \frac{N-1}{N} r_{N-1} \cos(\theta_{N-1}) \\ & + \frac{N-2}{N} r_{N-2} \Big(\cos(\theta_{N-1}) \cos(\Theta_{N-2}) - \sin(\theta_{N-1}) \sin(\Theta_{N-2}) \Big) \\ & + \frac{N-3}{N} r_{N-3} \Big(\cos(\theta_{N-1}) \cos(\Theta_{N-2} + \Theta_{N-3}) - \sin(\theta_{N-1}) \sin(\Theta_{N-2} + \Theta_{N-3}) \Big) \\ & + \dots \end{aligned} \tag{3-15c}$$

$$\begin{aligned} = \quad & \cos(\theta_{N-1}) \left[\frac{N-1}{N} r_{N-1} + \frac{N-2}{N} r_{N-2} \cos(\Theta_{N-2}) + \frac{N-3}{N} r_{N-3} \cos(\Theta_{N-2} + \Theta_{N-3}) + \ldots \right] \\ & - \sin(\theta_{N-1}) \left[\qquad\qquad \frac{N-2}{N} r_{N-2} \sin(\Theta_{N-2}) + \frac{N-3}{N} r_{N-3} \sin(\Theta_{N-2} + \Theta_{N-3}) + \ldots \right] \end{aligned} \tag{3-15d}$$

This expression can be written compactly as follows,

$$\phi^* = P\cos(\theta_{N-1}) + Q\sin(\theta_{N-1}), \tag{3-15e}$$

$$P = P(\boldsymbol{\Theta}) \equiv \left[\frac{N-1}{N} r_{N-1} + \frac{N-2}{N} r_{N-2} \cos(\Theta_{N-2}) + \frac{N-3}{N} r_{N-3} \cos(\Theta_{N-2} + \Theta_{N-3}) + \ldots \right], \tag{3-15f}$$

$$Q = Q(\boldsymbol{\Theta}) \equiv - \left[\qquad\qquad \frac{N-2}{N} r_{N-2} \sin(\Theta_{N-2}) + \frac{N-3}{N} r_{N-3} \sin(\Theta_{N-2} + \Theta_{N-3}) + \ldots \right], \tag{3-15g}$$

where $\boldsymbol{\Theta} \equiv \begin{bmatrix} \Theta_1 & \ldots & \Theta_{N-1} \end{bmatrix}^\top$. Finally, this expression can be written as a single trigonometric function by applying the following trigonometric identity for $z = \theta_{N-1}$. That is,

$$P\cos(z) + Q\sin(z) = C\cos(z + D), \tag{3-16a}$$

$$C = C(\boldsymbol{\Theta}) \equiv \sqrt{P^2 + Q^2}, \tag{3-16b}$$

$$D = D(\boldsymbol{\Theta}) \equiv \arctan\left(\frac{Q}{P}\right). \tag{3-16c}$$

The result is

$$\phi^* = C\cos\Big(\theta_{N-1} + D\Big). \tag{3-17}$$

Substituting this into Eq. (3-14b) results in the following expression for the error term.

$$\bar{\psi}'_{\text{ref}} = -\frac{N}{N+1}\Big(C\cos(\theta_{N-1} + D) + r_N\cos(\theta_N)\Big) \tag{3-18}$$

It should be noted that, although the final equation for ϕ^* looks simple, the time evolution of the amplitude $C(\boldsymbol{\Theta})$ and phase lag $D(\boldsymbol{\Theta})$ are generally complicated. However, in the third step is shown that, under certain conditions, these functions converge to some constant value.

Error Term with Turning

In the previous step, the error term $\bar{\psi}'_{\text{ref}}$ is derived for a lateral undulation gait without turning by setting the turning parameters in the Ijspeert model to zero. However, the goal is to design a head stabilizing method that is applicable to the Ijspeert model in Eq. (1-6) including the turning parameters, such that the head can be stabilized in a lateral undulation gait that includes turning. Therefore, the error term $\bar{\psi}'_{\text{ref}}$ is now derived for the Ijspeert model with arbitrary values for δ_k $\forall k \in \{1, \dots, N-1\}$. Allowing for arbitrary values for the turning parameters changes the derivation in the above only slightly. Starting from Eq. (3-14c) again and substituting $\phi_{\text{ref},k}$ with the expression in Eq. (1-6), this time including δ_k, gives

$$\phi^* = \sum_{k=1}^{N-1} \frac{k}{N} \phi_{\text{ref},k}, \tag{3-19a}$$

$$= \sum_{k=1}^{N-1} \frac{k}{N} \Big(r_k \cos(\theta_k) + \delta_k \Big), \tag{3-19b}$$

$$= \sum_{k=1}^{N-1} \frac{k}{N} r_k \cos(\theta_k) + \sum_{k=1}^{N-1} \frac{k}{N} \delta_k. \tag{3-19c}$$

The first term in Eq. (3-19c) is the same as Eq. (3-15a), which was found in the first step to equal Eq. (3-17). The second term is the weighted sum over the turning parameters δ_k, which can be computed online under the made assumption that these parameters are available to the head oscillator during the run. The result is similar to the one obtained in Eq. (3-17), but now with an additional turning term.

$$\phi^* = C \cos\Big(\theta_{N-1} + D \Big) + \delta^* \tag{3-20a}$$

$$\delta^* = \sum_{k=1}^{N-1} \frac{k}{N} \delta_k \tag{3-20b}$$

For the special case where all turning parameters of the body oscillators are set equal, i.e. $\delta_k = \delta$ $\forall k \in \{1, \dots, N-1\}$ (which is used in Section 4-2), the expression for δ^* can be simplified to

$$\begin{aligned} \delta^* &= \sum_{k=1}^{N-1} \frac{k}{N}\delta, && \text{(3-21a)}\\ &= \frac{\delta}{N}\sum_{k=1}^{N-1} k, && \text{(3-21b)}\\ &= \frac{\delta}{N}\,\frac{(N-1)N}{2}, && \text{(3-21c)}\\ &= \frac{\delta(N-1)}{2}. && \text{(3-21d)} \end{aligned}$$

For both of the cases of δ^*, the expression for the error term in Eq. (3-14b) becomes

$$\bar{\psi}'_{\text{ref}} = -\frac{N}{N+1}\Big(C\cos(\theta_{N-1} + D) + \delta^* + r_N\cos(\theta_N) + \delta_N\Big). \tag{3-22}$$

Convergence of the Error Term

In this step we determine the limits of the phase differences Θ_k, and use this to obtain the limits of the functions $C(\boldsymbol{\Theta})$ and $D(\boldsymbol{\Theta})$. Under the imposed restrictions on the initial conditions of the Ijspeert model parameters given at the start of this section, Lemma 1.1 is applied to find that the limits of the phase differences are expressed in Eq. (3-3). This equation is rewritten in a more convenient form as

$$\lim_{t\to\infty}\Theta_k = \lim_{t\to\infty}\theta_k - \theta_{k+1} = \gamma_{k,k+1} + m_k\ 2\pi \qquad \forall k \in \{1,\dots,N-1\}, \tag{3-23}$$

where $m_k \equiv n_{k,k+1} \in \mathbb{Z}$.

The functions $C(\boldsymbol{\Theta})$ and $D(\boldsymbol{\Theta})$ are both functions of the phase differences Θ_k. As the arguments in $C(\boldsymbol{\Theta})$ and $D(\boldsymbol{\Theta})$ become constant in the limit according to Eq. (3-23), the function outputs also become constant. The limits can therefore be written as

$$\lim_{t\to\infty} C(\boldsymbol{\Theta}(t)) = C^\infty, \tag{3-24}$$

$$\lim_{t\to\infty} D(\boldsymbol{\Theta}(t)) = D^\infty, \tag{3-25}$$

$$C^\infty \equiv \sqrt{(P^\infty)^2 + (Q^\infty)^2}, \tag{3-26}$$

$$D^\infty \equiv \arctan\left(\frac{Q^\infty}{P^\infty}\right), \tag{3-27}$$

$$P^\infty \equiv \quad \left[\frac{N-1}{N} r_{N-1} + \frac{N-2}{N} r_{N-2}\cos(\gamma_{N-2,N-1}) + \frac{N-3}{N} r_{N-3}\cos(\gamma_{N-2,N-1}+\gamma_{N-3,N-2}) + \ldots\right], \tag{3-28}$$

$$Q^\infty \equiv -\left[\qquad\qquad \frac{N-2}{N} r_{N-2}\sin(\gamma_{N-2,N-1}) + \frac{N-3}{N} r_{N-3}\sin(\gamma_{N-2,N-1}+\gamma_{N-3,N-2}) + \ldots\right]. \tag{3-29}$$

The terms C^∞, D^∞, P^∞ and Q^∞ are constants. The constants P^∞ and Q^∞ are obtained by replacing Θ_k with $\gamma_{k,k+1}$ in Eq. (3-15f) and (3-15g). Using the derivations in the above, the error in Eq. (3-22) is shown to converge to zero under certain conditions in Proposition 1.

Proposition 1. *Consider the Ijspeert model in Eq. (1-6) defined over a chain graph with adjacency matrix* A*, and with phase biases adhering to Eq. (1-3), coupling weight* $w > 0$ *and the initial phases meeting the criteria in Eq. (3-7) and (3-8) (i.e. Assumption 1.1 holds). If the amplitude and turning parameter of the* N^{th} *oscillator are set to* $r_N = C^\infty$ *and* $\delta_N = -\delta^*$*, respectively, and the phase bias parameter between the* $N-1^{th}$ *and* N^{th} *oscillators is set to* $\gamma_{N-1,N} = -D^\infty + \pi$*, the reference signals from the Ijspeert model asymptotically converge to a head-body aligned lateral undulation gait, i.e. the control objective in Eq. (3-13) is achieved.*

Proof. We examine the convergence of the error term in Eq. (3-22). First, $\theta_{N-1} = \theta_N + \Theta_{N-1}$ (which is the rewritten form of the definition of Θ_k for $k = N$) is substituted in Eq. (3-22) to obtain

$$\bar{\psi}'_{\text{ref}} = -\frac{N}{N+1}\Big(C\cos(\theta_N + \Theta_{N-1} + D) + \delta^* + r_N\cos(\theta_N) + \delta_N\Big). \tag{3-30}$$

By using Eq. (3-23), (3-24) and (3-25), the limit of the error term is expressed as

$$\lim_{t\to\infty} \bar{\psi}'_{\text{ref}} = -\frac{N}{N+1}\Big(C^\infty\cos(\theta_N + \gamma_{N-1,N} + D^\infty) + \delta^* + r_N\cos(\theta_N) + \delta_N\Big), \tag{3-31}$$

where the constants C^∞ and D^∞ are defined in Eq. (3-26) to (3-29). To satisfy the control objective in Eq. (3-13), this equation is equated to zero. To do so, the oscillating terms (involving a θ_N) need to cancel each other, and all constant terms (δ_1 and δ^*) also need to cancel each other. There are two options to make the oscillating parts cancel each other, one for which r_N is non-negative and one for which it is non-positive (the options overlap for $C^\infty = 0$). Both options suffice to satisfy the control objective in Eq. (3-13), so we consider the solution for which r_N is non-negative, which is given as

$$r_N = C^\infty, \tag{3-32}$$

$$\gamma_{N-1,N} = -D^\infty + \pi, \tag{3-33}$$

$$\delta_N = -\delta^*. \tag{3-34}$$

Note that r_N is indeed non-negative here, as $C^\infty \geqslant 0$.

□

Remark 1. *It is interesting to point out that the head stabilization method for the Ijspeert model can be extended to robotic lampreys using sine-based generators (see Section 1-2). By equating* r_k*,* $\gamma_{k-1,k}$ *and* δ_k *to their analogous parameters in the sine-based generator, and subsequently computing* r_N*,* $\gamma_{N-1,N}$ *and* δ_N *with Eq. (3-32) to (3-34), the error term* $\bar{\psi}'_{ref}$ *equals zero for any time instance, instead of converging to zero asymptotically. The analogous sine-based system is*

$$\phi_{\text{ref},1} = r_1 \sin(\omega t - \sum_{l=1}^{N-1} \gamma_{l,l+1}) + \delta_1, \tag{3-35a}$$

$$\phi_{\text{ref},k} = r_k \sin(\omega t - \sum_{l=k}^{N-1} \gamma_{l,l+1}) + \delta_k \qquad \text{for } k \in \{2, \ldots, N-1\}, \tag{3-35b}$$

$$\phi_{\text{ref},N} = r_N \sin(\omega t) + \delta_N. \tag{3-35c}$$

Remark 2. *As mentioned in Section 1-2-3, the amplitude dynamics in the original Ijspeert model are neglected in this thesis. However, the head stabilization method can be extended to include the amplitude dynamics. Consider the expression of the error term in Eq. (3-22), but now for* r_k *being the amplitude dynamics state. In order to take the limit of this expression to obtain* $\lim_{t\longrightarrow\infty} \bar{\psi}'_{ref}$*, the limit* $\lim_{t\longrightarrow\infty} r_k$ *now also needs to be considered. In Section 1-2-3 is described that the amplitude dynamics are a second order damped system that make* r_k *track* R_k*, and that the setpoints* R_k *are the global asymptotically stable equilibrium points of the corresponding states* r_k*. Assuming that the amplitude setpoints* R_k *remain constant, it follows that* $\lim_{t\longrightarrow\infty} r_k = R_k$*. This means that the amplitude dynamics are included by replacing* r_k *with* R_k *in Eq. (3-24) to (3-29), and* r_N *with* R_N *in Eq. (3-31) and (3-32). From the new expressions then follows that the head stabilization control objective is achieved in the Ijspeert model including amplitude dynamics.*

3-3 Numerical Results

The goal of the simulations is to verify that the control objectives in Section 3-1 are achieved. This section is split into three parts. First, the models used in the simulations and their parameter settings are explained in Section 3-3-1. Second, the Ijspeert model simulations are shown in Section 3-3-2. Third, the simulation results for the head stabilization method is verified to hold in Section 3-3-3. In this part, the head stabilization method is also compared to the Ijspeert model without head stabilization [21]. The latter is referred to as the baseline model in this section.

The simulations are done in Matlab 2020b. The Ijspeert model, motor units and body and fluid model are combined into one closed loop state space model that is solved using the `ode23tb` [17] and `ode45` solvers with relative and absolute tolerances of 10^{-3}.

3-3-1 Models and Parameters

Both the Ijspeert model simulations and head stabilization simulations require the Ijspeert model. The head stabilization simulations additionally require models for the motor units and body fluid model, which are combined according to the system schematic in Figure 2-4. The three models are described below, together with their parameter settings.

Ijspeert Model

For the Ijspeert model, the description in Eq. (1-6) is used. This model is simulated for two different parameter settings: the not stabilized settings as a baseline [14, 21], and the head stabilized settings. The parameters for both models are listed in Table 3-1, and are either the result of tuning or are adopted from [14, 21].

For the lateral undulation gait to propel the body in the head first direction and not the tail first direction, either the combination $\gamma_{k,k+1} < 0$ and $\omega > 0$, or $\gamma_{k,k+1} > 0$ and $\omega < 0$ is required. This is different from [14, 21], with the reason that there the head is defined as the first segment instead of the $N + 1^{\text{th}}$ one. The combination $\gamma_{k,k+1} < 0$ and $\omega > 0$ is chosen.

Deriving the phase bias parameters $\gamma_{k,k+1}$ from the desired number of waves on the body, S, is adopted from [21]. The desired number of waves is chosen to be $S = 1$. A full number of standing waves is expected to result in a more symmetrical load of the fluid on the center of mass of the body, which lessens the sideways oscillations of the CM and therefore increases head stability.

As can be noticed from the table, the conversion equations from S to $\gamma_{k,k+1}$ are not the same for the not stabilized and stabilized Ijspeert model. The latter is actually the one that differs from the original equation. Because the head joint does not participate in the lateral undulations in that case, the number of joints in the equation is dropped by one to keep the benefit of symmetrical loading.

All turning parameters except for δ^* are set equal. This means that the simplified expression for δ^* in Eq. (3-21) can be used.

Table 3-1: Parameter values for the baseline and head stabilized Ijspeert model.

Parameter	Value in the baseline Ijspeert model	Value in the stabilized Ijspeert model	Description	Source/Eq.
N	7	7	number of joints and Ijspeert oscillators	[14, 21]
S	1	1	desired number of standing waves on the body	
ω	π rad/s	π rad/s	exogenous frequency	(1-4)
w	4	4	coupling strength	[14], (1-5)
$r_1 \, \dots \, r_{N-1}$	0.20 rad	0.20 rad	amplitude of body oscillators	
r_N	0.20 rad	0.17143 rad	amplitude of head oscillator	(3-32)
$\gamma_{1,2} \, \dots \, \gamma_{N-2,N-1}$	$-\frac{2\pi S}{N}$	$-\frac{2\pi S}{N-1}$	phase bias parameters for the body couplings	[21]
$\gamma_{N-1,N}$	$-\frac{2\pi S}{N}$	$\frac{4}{3}\pi$ rad	phase bias parameters for the head coupling	[21], (3-33)
$\gamma_{k+1,k}$	$-\gamma_{k,k+1}$	$-\gamma_{k,k+1}$	phase bias parameters	(1-3)
$\delta_1 \, \dots \, \delta_{N-1}$	δ	δ	turning parameter for the body oscillators	
δ_N	δ	$-\frac{1}{2}\delta(N-1)$	turning parameter for the head oscillator	(3-34), (3-21)

Furthermore, the phases of the oscillators are initialized at the arbitrarily chosen vector $\boldsymbol{\theta}(0) = \begin{bmatrix} 2 & 0.5 & -1 & -1 & -2.5 & -3 & -4 \end{bmatrix}^\top + \frac{\pi}{2}\mathbb{1}$. This vector adheres to the restrictions given in Eq. (3-7) and (3-8), and is kept the same for all simulations.

Motor Units

The motor units subsystem consists of one motor unit for every oscillator output and for every joint to be actuated. Each motor unit refers to a motor, motor controller and sensor for the joint angle. The specific hardware components used for this are not explored here, and furthermore the dynamics of the conversion of the motor control action to the torque delivered by the motor are not taken into account. The dynamics from the motor units arise from the motor controllers, which are modelled as the following PD-controllers [14]

$$e_k = \phi_{\mathrm{ref},k} - \phi_k, \tag{3-36a}$$

$$u_k = K_{\mathrm{m,P}}\ e_k + K_{\mathrm{m,D}}\ \dot{e}_k, \tag{3-36b}$$

with proportional gain $K_{\mathrm{m,P}} = 20$ and derivative gain $K_{\mathrm{m,D}} = 5$ [8]. These gains are used in the design of the robotic snake Mamba (see Section 2-1-1), and are therefore deemed realistic.

Body and Fluid Model

For the kinematics and body-fluid interactions, the underwater snake-robot model from Section 2-3-1 is used. The parameters for the fluid model and the kinematic parameters are given in Table A-1. The current $\mathbf{V_c}$ is set to zero.

The states of the fluid model are given in Eq. (2-4). The entries in $\boldsymbol{\psi}$ are initialized at $\boldsymbol{\psi}(0) = \begin{bmatrix} -0.1 & -0.3 & -0.2 & 0.0 & 0.3 & 0.2 & 0.0 & 0.1 \end{bmatrix}^\top$, which produces an average body angle of zero but apart from that is chosen arbitrarily. The other states, $\mathbf{p_{cm}}$, $\dot{\boldsymbol{\psi}}$ and $\mathbf{p_{cm}}$, are initialized at zero. These initial states are used for all simulations.

3-3-2 Ijspeert Model Simulations

We first verify that frequency synchronization occurs in the phase dynamics of the Ijspeert model (Eq. (3-2)), and that the phase differences converge to the phase bias parameters (Eq. (3-3)). Since the phase dynamics of the Ijspeert model are not influenced by external signals, it can be studied isolated from the rest of the system.

Frequency synchronization is verified by plotting $\dot{\Theta}_k = \dot{\theta}_k - \dot{\theta}_{k+1}$ in Figure 3-5. To verify if the phase differences converge to the phase biases, the signals $\Theta_k - \gamma_{k,k+1} = \theta_k - \theta_{k+1} - \gamma_{k,k+1}$ are plotted in Figure 3-6. Simulations are done for 10 seconds, and only the plots for $k \in \{1, 2, 3\}$ are shown. In the simulated time interval the signals $\dot{\Theta}_k$ appear to converge to zero, and the signals Θ_k appear to converge to integer multiples of 2π. This verifies that the lateral undulation gait objectives in Eq. (3-2) and (3-3) are achieved.

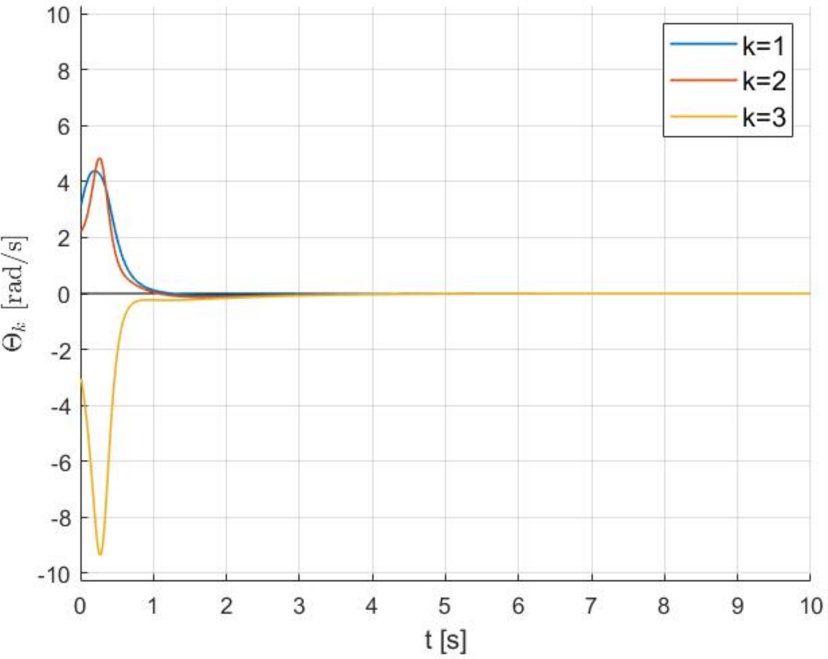

Figure 3-5: The evolution of the frequency differences $\dot{\Theta}_k$ for $k \in \{1, 2, 3\}$.

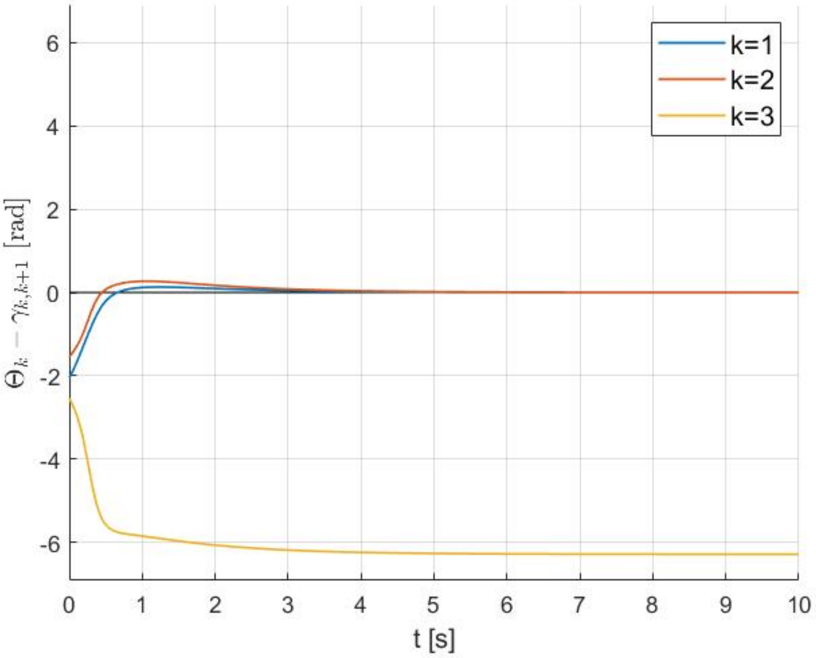

Figure 3-6: The evolution of the phase differences minus the phase biases, $\Theta_k - \gamma_{k,k+1}$, for $k \in \{1, 2, 3\}$.

3-3-3 Head Stabilization Simulations

To verify if the control objective in Eq. (3-13) is achieved, the reference average body angle $\bar{\psi}'_{\text{ref}}$ is plotted. Moreover, the effect of non-instant motor dynamics is investigated by plotting the average body angle $\bar{\psi}'$. These are plotted for both the head stabilized Ijspeert model and the baseline model.

The baseline and head stabilized Ijspeert models are simulated with the motor units and fluid model for 10 seconds. The turning parameters are set to $\delta = 0.10$ to include the effect of a nonzero value for the turning parameter on the error signals. The results are shown in Figure 3-7.

First of all, the reference average body angle $\bar{\psi}'_{\text{ref}}$ (the dashed orange line) appears to converge to zero within the simulation time. This verifies that the control objective in Eq. (3-13) is achieved, and that Proposition 1 holds. The effect of the non-instant motor dynamics is that $\bar{\psi}'$ does not converge to zero (the solid orange line), but instead keeps oscillating around a nonzero offset. However, it is verified that the difference between $\bar{\psi}'_{\text{ref}}$ and $\bar{\psi}'$ becomes smaller for higher motor gains (not shown Figure 3-7), indicating that the difference can indeed be attributed to the non-instant motor dynamics.

Perfect head-body alignment is not achieved for non-instant motor dynamics, but the head-body alignment is significantly improved compared to the baseline model (the solid blue line), both in terms of oscillation amplitude and oscillation offset.

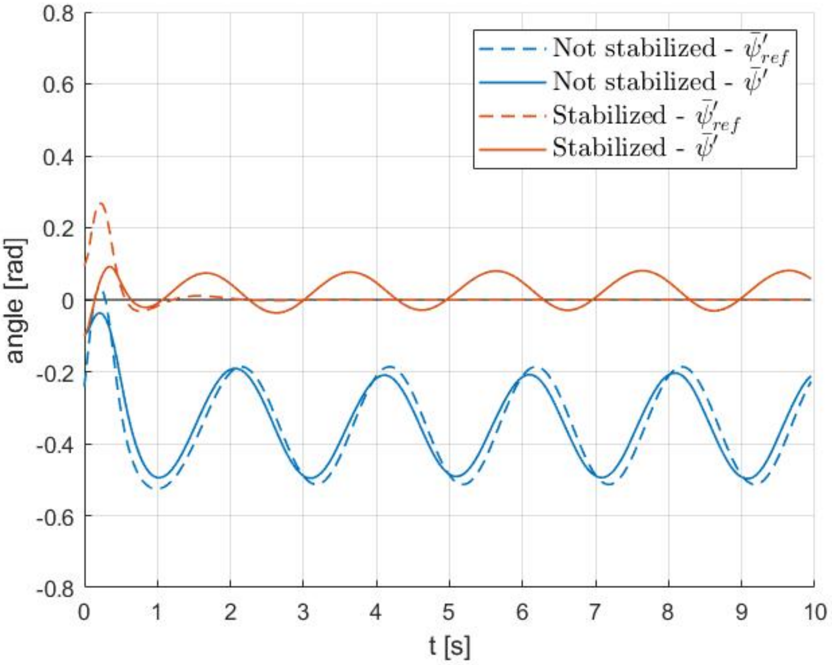

Figure 3-7: The evolution of $\bar{\psi}'_{\text{ref}}$ and $\bar{\psi}'$, both for the head stabilized Ijspeert model and baseline (not stabilized) Ijspeert model.

3-4 Discussion

Locomotion objectives are formulated in Section 3-1-1 to achieve a desirable locomotion gait. Section 3-1-2 shows that these objectives are achieved, first using a proof from [14], and then using an alternative proof. Although both proofs seem to arrive at the same results, the alternative proof includes restrictions on the initial phases that do not appear in the proof of [14]. The reason for this difference is that the original proof does not consider the effect of the undesirable unstable phase-locked solutions on the convergence of the phase differences. Namely, in the appendix of [14], the argument is made that, because the desirable phase-locked solutions with $\theta_k - \theta_l = \gamma_{kl}$ are stable, the outputs of the oscillators asymptotically converge to these solutions. However, considering the existence of the unstable phase-locked solutions, this claim only holds locally, not globally. The consequence of this is that, in order to make the oscillator phases converge to the desirable solutions, additional restrictions on the initial phases need to be included. This has been the motivation to include the alternative proof.

In the head stabilization problem formulation in Section 3-2-1, the assumption is made that the motor dynamics are instantaneous. With this assumption, only the reference angles generated by the Ijspeert model $\phi_{\text{ref},k}$ need to be considered, rather than the actual joint angles ϕ_k. The method constructed in Section 3-2-2 achieves the head stabilization control objective, meaning that the reference signals outputted by the Ijspeert network make the body asymptotically converge to a head stabilized lateral undulation gait. This convergence is perfect under the instant motor assumption, since the dynamics of the Ijspeert model dynamics only depend on internal states and are therefore not prone to disturbance or noise. This can be seen back in the evolution of $\bar{\psi}'_{\text{ref}}$ of the head stabilized Ijspeert model, shown in Figure 3-7. In reality, perfect head stabilization is not achieved because of non-instant motor dynamics. This is seen in the evolution of $\bar{\psi}'$ of the stabilized Ijspeert model in Figure 3-7. Still, the stabilized Ijspeert network shown in Figure 3-7 outperforms the Ijspeert model without stabilization in terms of the head-body alignment errors $\bar{\psi}'_{\text{ref}}$ and $\bar{\psi}'$.

As mentioned in Section 3-3-3, the difference between $\bar{\psi}'_{\text{ref}}$ and $\bar{\psi}'$ becomes smaller for higher motor gains, indicating that this error can indeed be attributed to the non-instant motor dynamics. The implication of this is that, for the first time, the motor dynamics are the limiting factor in head stabilization and not the reference signals. An advantage of this is that, in order to improve head stability, the motors can be tuned more aggressively (something to consider when implementing the method). This means that there exist motor gains for which the head stabilization method is better than any existing method. However, it is still possible that some methods are better below certain motor gains.

The head stabilization method is designed for the Ijspeert model in Eq. (1-6), and requires restrictions on the parameters ω_k, w_{kl} and γ_{kl}. It works by giving two of the constant parameters of the head oscillator, r_N and $\gamma_{N-1,N}$, specific values that are precomputed from the parameter values of the other oscillators. Furthermore, it requires turning control parameter to the head oscillator, δ_N, to be a specific function of the turning control parameters to the other oscillators, which can be computed online. The fact that the method is entirely based on the parameter settings has the benefit that no changes to the Ijspeert model dynamics or to the hardware of the robot are required. This makes it simple to implement the head stabilization method in robotic lamprey designs using the Ijspeert model.

Chapter 4

Head-led Target Tracking

This chapter focuses on the head-led target tracking problem, in which the head stabilization algorithm in Chapter 3 is applied to a target tracking application. First, the control problems are formulated in Section 4-1. Then, the control design is described in Section 4-2. The control design is numerically verified in Section 4-3. Last, the results are discussed in Section 4-4.

4-1 Head-Led Target Tracking Problem

The goal of target tracking with a visually guided robotic lamprey is to track the position of the target with the position of the tip of the head segment (where the cameras are attached). This requires both the direction and velocity of the robot to be controlled. As mentioned in Section 1-2-3, this thesis only considers turning control.

Target tracking is approached by combining a novel form of turning control with a forward lateral undulation gait. Turning control normally relies on visual information from cameras that are attached to the head segment, and as this information gets distorted by the gait, the target tracking accuracy is decreased. Therefore, a strategy is implemented to reduce the distortions on the camera inputs by stabilizing the target in the camera field of view. This strategy utilizes the head stabilization algorithm in Chapter 3, that is designed for stabilizing the head segment itself. Since the head stabilization algorithm is designed for a scenario without a target, additional target tracking elements are added in the head-led target tracking design. To clarify the distinction between the head stabilization algorithm and the head-led target tracking design throughout this chapter, their algorithms are provided in Appendix B.

The head-led target tracking problem consists of two parts: increasing the accuracy of the visual inputs, and turning the body towards the target. For the first part of the problem, the distortions of the target position in the camera field of view due to the lateral undulation gait are reduced. This is approached by actuating only the head joint, again with the arguments that the rest of the body remains available for the gait, and the two problems can be treated separately. The objective is to direct the head segment towards the target, using the head-target alignment error signal β. This error is measured by the cameras that are attached to the tip of the head segment, and centered in the the forward direction of the head segment. The error signal is the angle between the direction of the center of the cameras, and the direction from the camera to the target (see Figure 4-1). It is assumed that the vision processor can perfectly retrieve the error signal β from the pixels of the target in the camera view. Perfect head-target alignment is achieved when error signal β is zero, so the control objective is given as

$$\lim_{t \to \infty} \beta = 0. \tag{4-1}$$

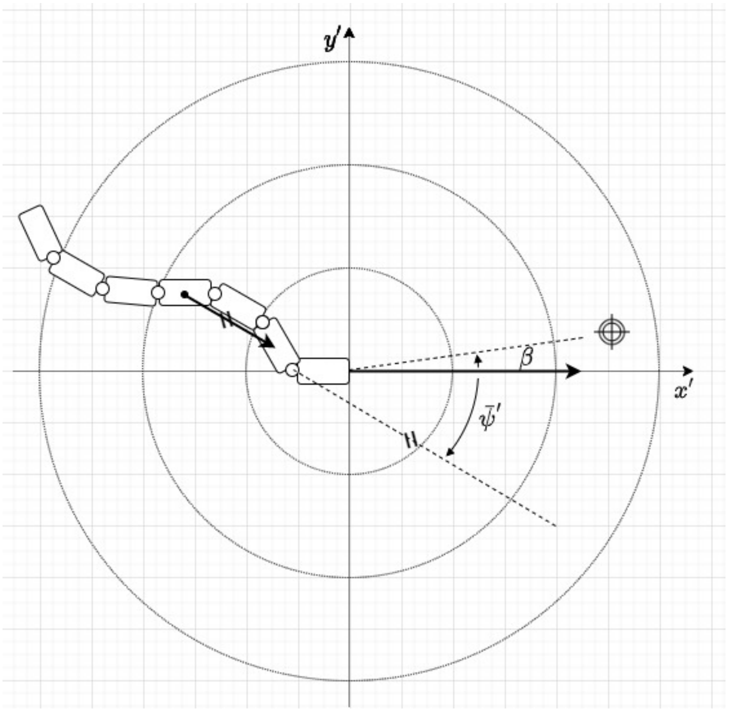

Figure 4-1: Schematic of head-led target tracking with head-body alignment error signal $\bar{\psi}'$ and head-target alignment error signal β.

The second part, turning the body towards the target, requires information about the direction to the target relative to the orientation of the robot. With a target centered in the field of view, the cameras do not provide this information anymore but only inform how well the head is directed towards the target. However, given that the direction of the head segment converges to the direction towards the target, the body can be directed towards the target by aligning itself with the head segment using turning control. The head-body alignment error is $\bar{\psi}'$, which is the average body angle measured in the head fixed frame (see Figure 4-1). However, as a measurement of this error is not directly available to the robot, the signal $\bar{\psi}'_{\text{ref}}$ is used instead, which is the instant motor approximation of $\bar{\psi}'$. We assume that the motor dynamics are instant, i.e. $\phi_k = \phi_{\text{ref},k}$ and $\bar{\psi}'_{\text{ref}} = \bar{\psi}'$. Under this assumption, perfect head-body alignment is achieved when $\bar{\psi}'_{\text{ref}}$ is zero. The head-body alignment control problem is formulated by Eq. (3-13), repeated here for convenience.

$$\begin{aligned}\lim_{t \longrightarrow \infty} \bar{\psi}'_{\text{ref}} &= 0 \\ \bar{\psi}'_{\text{ref}} &= \frac{1}{N+1} \sum_{k=1}^{N} k \phi_{\text{ref},k}\end{aligned}$$

To summarize this section, the head joint is controlled to direct the head segment towards the target, and the body is controlled to turn in alignment with the head. The combination of these two is referred to as head-led target tracking. The similarity with the head stabilization problem described in Section 3-2-1 is that the head segment is aligned with the average body angle by reducing $\bar{\psi}'_{\text{ref}}$. For this reason, both problems share the same control objective in Eq. (3-13). However, this alignment is achieved differently in both problems; the head-led target tracking uses turning control of the body, whereas in the head stabilization problem the head joint is actuated to achieve this.

4-2 Head-Led Target Tracking Design

First, the head-led target tracking system description is given in Section 4-2-1. In the remainder of the section, the subsystems are described in more detail. Continuing with the division in the problem formulation, the design for head-led target tracking is subdivided into head-target alignment and head-body alignment. The head-target alignment strategy uses the head-target alignment controller, which is explained in Section 4-2-2. After that, Section 4-2-3 describes the head-body alignment strategy that uses a turning controller.

4-2-1 Head-Led Target Tracking System Description

The head-led target tracking system is shown in Figure 4-2 and contains the head-target alignment controller described in Section 4-2-2 and the turning controller described in Section 4-2-3. A description of the individual subsystems is given below.

Starting on the left, the visual unit consists of the cameras and visual processor, and has the goal of determining β. This subsystem is not explored further, and a perfect measurement of β is assumed to be available. The head-target alignment controller consists of both the PI-controller and the output of the N^{th} oscillator, as given in Eq. (4-6a). The PI-controller has a control law given in Eq. (4-8), and its output signal α is multiplied by a gain of $-\frac{N+1}{N}$ before it is added to the oscillator output y_N. The signal α serves the additional purpose of providing the approximation of the head-body alignment error for the turning controller. The turning controller is as described in Eq. (4-8). The head stabilized Ijspeert model, motor units and body and fluid model, as well as the initialization of the states, are as described in Section 3-3-1.

In the remainder of this section, the reasoning behind the design of the head-led target tracking system is provided. Furthermore, the algorithm for the head-led target tracking design is provided in Algorithm 2 in Appendix B.

4-2-2 Head-Target Alignment Controller

As mentioned in Section 4-1, the head-target alignment problem is approached by actuating the head joint using visual information. The motor unit of the head joint therefore requires reference signal $\phi_{\text{ref},N}$ to direct the head segment towards the target. This control task is referred to as head-target alignment control, which is visualized in Figure 4-3, and is written in general form as

$$\phi_{\text{ref},N} = g_{\beta}(\beta). \tag{4-2}$$

Note that the other reference signals $\phi_{\text{ref},k}$ for $k \in \{1, \ldots, N-1\}$ are still produced by the Ijspeert network. The goal now is to specify the control law $g_{\beta}(\beta)$ such that the objective in Eq. (4-1) is achieved.

To do so, consider the visualization of the problem in Figure 4-3, containing error signal β and controlled variable $\phi_{\text{ref},N}$. Note that in Figure 4-3, the joint angles equal the reference signals under the instant motor dynamics assumption. For $\phi_{\text{ref},N} = 0$, the error signal β would

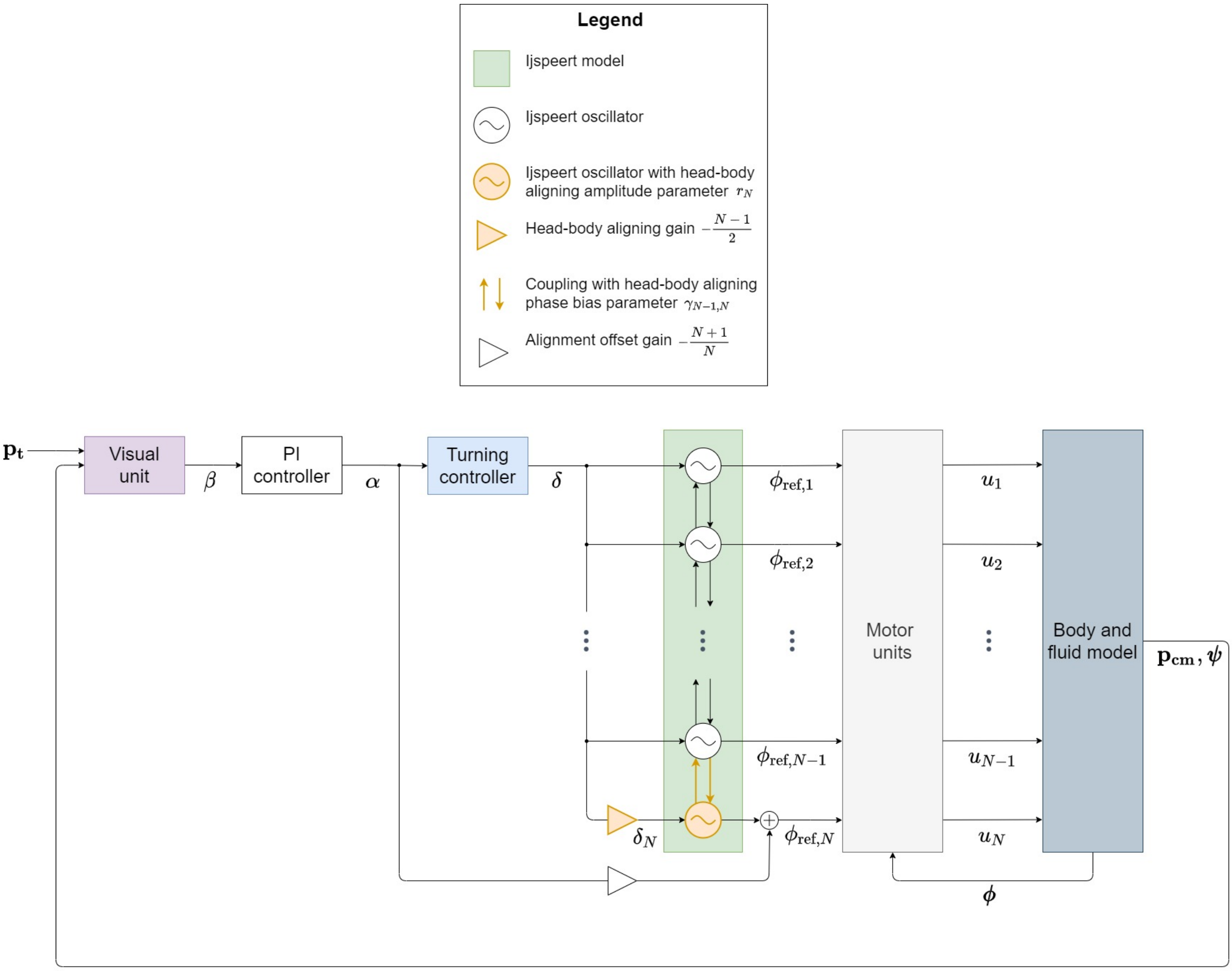

Figure 4-2: System description of the head-led target tracking design.

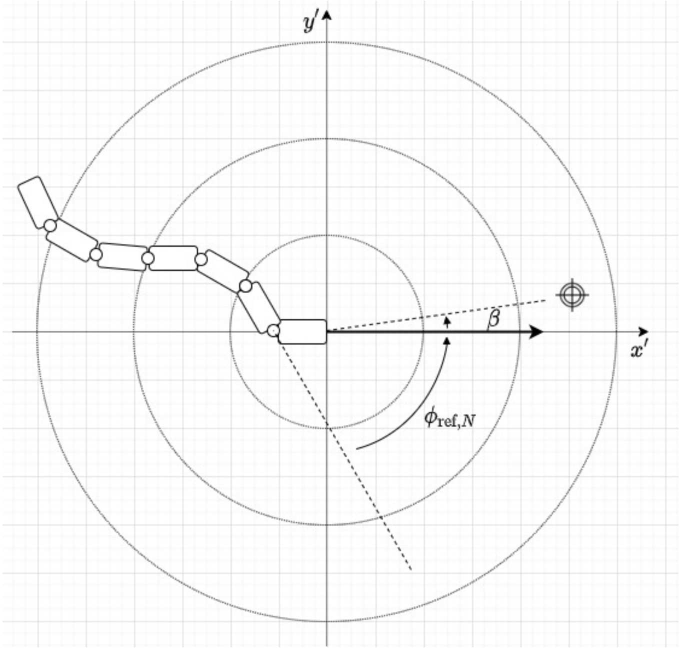

Figure 4-3: Schematic of the head-target alignment control problem, under the instant motor dynamics assumption, $\phi_k = \phi_{\mathsf{ref},k}$.

consist of two components: a rhythmic component resulting from the lateral undulations of the body, and a remaining component depending on the position of the target with respect to the position and orientation of the robot. This composition of β suggests to design the target alignment controller in two parts: one part mitigating the rhythmic component of β from the lateral undulations, and the other part reducing the remaining component. This partitioning is visualized in Figure 4-5, of which the signals are explained below.

The periodic component of β can be mitigated by using a head stabilizing reference signal for the head joint. Section 3-2-2 has already been devoted to finding such a reference signal, and Proposition 1 shows that, if oscillator N in the Ijspeert network is provided with the head stabilizing parameters r_N and $\gamma_{N-1,N}$ from Eq. (3-32) and (3-33), and with the controlled parameter δ_N from Eq. (3-34), its output aligns the head segment with the average body angle (given that Assumption 1.1 holds and assuming the motor dynamics are instant). The output of the N^{th} oscillator is referred to as y_N instead of $\phi_{\text{ref},N}$, as it is not used directly as reference signal to the head joint anymore. The outputs of oscillators $k \in \{1, \dots, N-1\}$ are still referred to as $\phi_{\text{ref},k}$, as these outputs are directly used as reference signal for the corresponding motor units.

The signal $\phi_{\text{ref},N} = y_N$ alone would align the head segment with the average body angle and achieve $\lim\limits_{t \longrightarrow \infty} \psi'_{\text{ref}} = 0$ (see Section 3-2), which is shown in the schematic in the head fixed frame of Figure 4-4a. This would direct the head segment in a stabilized direction, but not in the direction that minimizes β. What therefore remains is to create some offset between the head angle and the average body angle that minimizes β. Creating such an offset implies that ψ'_{ref} has to converge to α, with α being the offset that minimizes β (see Figure 4-4b). This is done with the second part of the controller. Its design is broken down into two steps: computing the desired offset α that minimizes β, and making ψ'_{ref} converge to α.

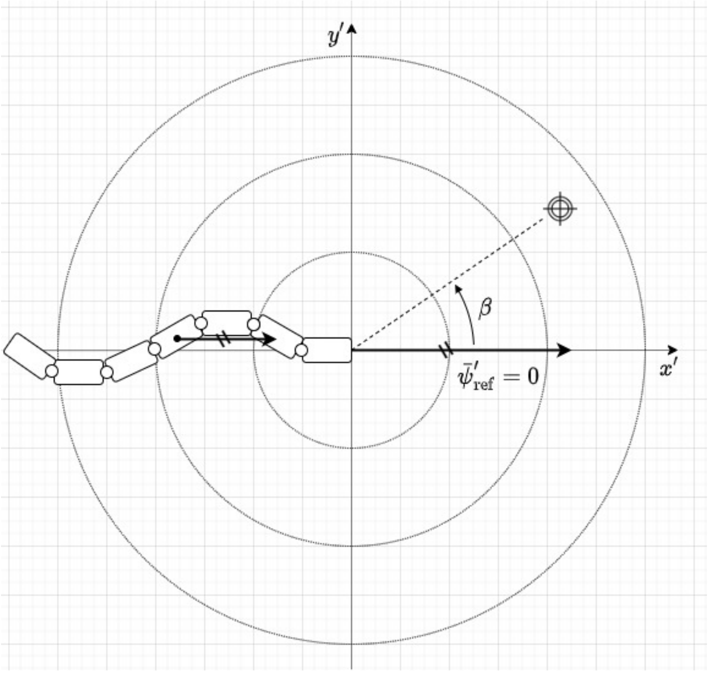

(a)

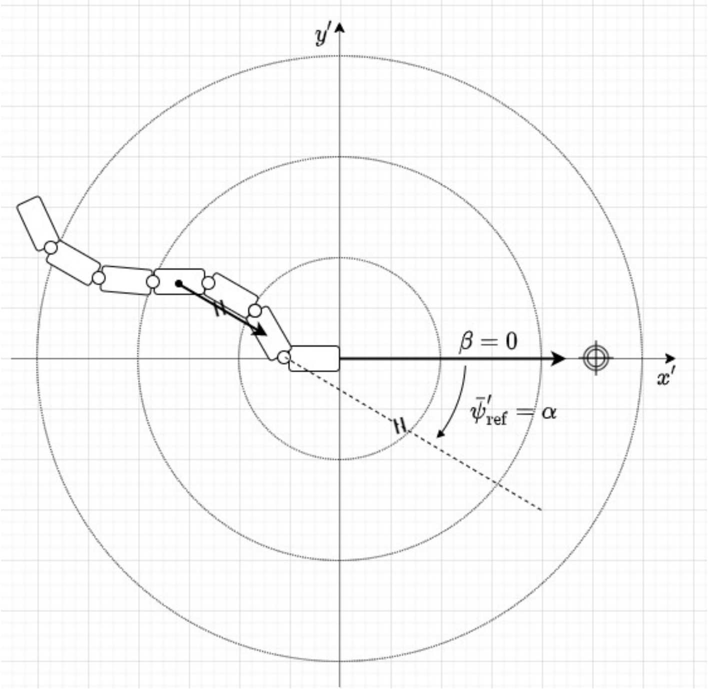

(b)

Figure 4-4: Schematic of two target tracking scenarios. In **(a)** the head joint aligns the head segment with the average body direction, and in **(b)** the head joint creates an offset of α between the head segment and average body direction. The figures show ideal situations where the oscillators are perfectly synchronized, and α perfectly directs the head towards the target. Note that, apart from the angle of the head joint, the bodies of the robots in the two figures are the same.

For computing the desired offset α, the following PI control law is used.

$$\alpha = \alpha(\beta) = -\left(K_{\mathrm{h,P}}\beta + K_{\mathrm{h,I}} \int_0^t \beta(\tau)\ d\tau \right) \tag{4-3}$$

The gains $K_{\mathrm{h,P}}$ and $K_{\mathrm{h,I}}$ are the proportional and integral gains, respectively. The minus sign in front is due to the definitions of α and β. Namely, if β needs to decrease, α needs to increase and vise versa (see Figure 4-4). Eq. (4-3) contains the dynamics of the PI-controller subsystem in Figure 4-2. With the desired offset α, the reference signal $\phi_{\mathrm{ref},N}$ must be altered in such a way that $\bar{\psi}'_{\mathrm{ref}}$ converges to this desired offset. This requirement is captured in the following objective

$$\lim_{t \to \infty} \bar{\psi}'_{\mathrm{ref}} - \alpha = 0. \tag{4-4}$$

Although at first glance this seems to be done simply by subtracting offset signal α from $\phi_{\mathrm{ref},N}$, the fact that the average body direction slightly changes as the head changes its direction must be taken into account as well. The effect of the reference signal $\phi_{\mathrm{ref},N}$ on the average body angle signal is captured in Eq. (3-14), repeated here for convenience.

$$\begin{aligned} \bar{\psi}'_{\mathrm{ref}} &= -\frac{N}{N+1}\left(\phi^* + \phi_{\mathrm{ref},N}\right) \qquad \text{with} \\ \phi^* &= \sum_{k=1}^{N-1} \frac{k}{N}\phi_{\mathrm{ref},k} \end{aligned}$$

Note that this equation is considered for the general case where the turning parameters δ_k have arbitrary values. In Section 3-2-2 is concluded that for $\phi_{\mathrm{ref},N} = y_N$ with $y_N = r_N \cos(\theta_N) + \delta_N$, the sum $\phi^* + \phi_{\mathrm{ref},N}$ becomes zero in the limit of $t \to \infty$. If instead $\phi_{\mathrm{ref},N} = y_N - \frac{N+1}{N}\alpha$ is chosen, the following expression is obtained.

$$\bar{\psi}'_{\mathrm{ref}} = -\frac{N}{N+1}\left(\phi^* + y_N - \frac{N+1}{N}\alpha\right) \tag{4-5a}$$

$$= -\frac{N}{N+1}(\phi^* + y_N) + \alpha \tag{4-5b}$$

By taking the limit and again applying $\lim_{t \to \infty} \phi^* + y_N = 0$, it can be concluded that the objective in Eq. (4-4) holds for

$$\phi_{\mathrm{ref},N} = y_N - \frac{N+1}{N}\alpha, \tag{4-6a}$$

$$= \left(y_N - \frac{1}{N}\alpha\right) - \alpha. \tag{4-6b}$$

The interpretation of the term $-\frac{N+1}{N}\alpha$ is best explained with the rewritten expression in Eq. (4-6b), of which the components are visualized in Figure 4-5. As described before, the reference signal $\phi_{\text{ref},N} = y_N$ would align the head with the average body direction. If the offset $-\alpha$ is added to the head joint angle, the average body direction itself also changes. This change is accounted for in the term between the parentheses, $y_N - \frac{1}{N}\alpha$, where the additional term $-\frac{1}{N}\alpha$ is the effect of the offset on the average body direction. For the special case where $\alpha = 0$, i.e. the target is always straight in front of the head segment, the reference signal to the N^{th} oscillator would reduce to $\phi_{\text{ref},N} = y_N$, and the head-target alignment controller would reduce to the head stabilization method described in Section 3-2-2.

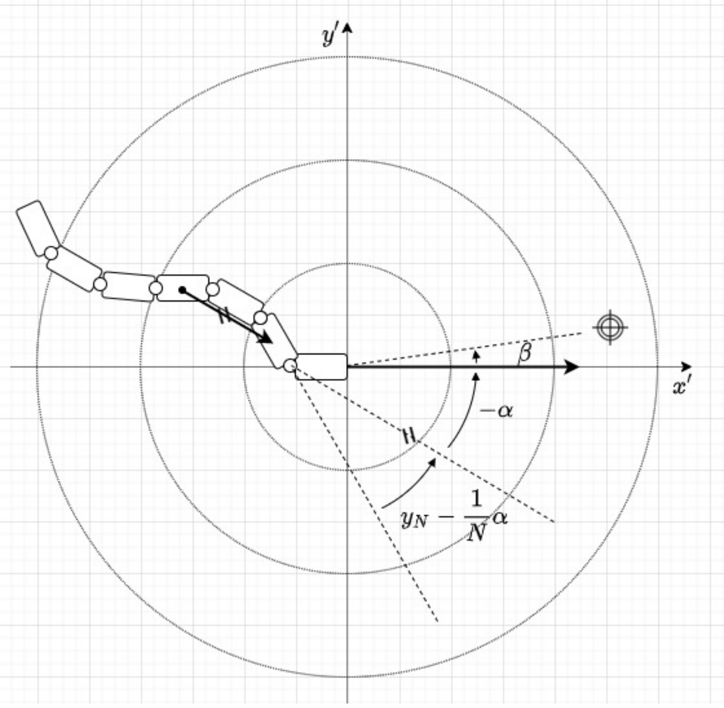

Figure 4-5: Visualization of the components of $\phi_{\text{ref},N}$. The left most dashed line is the $\phi_{\text{ref},N} = 0$ direction to which the actual reference signal is added. The figure shows the scenario for instant motor dynamics and for when the oscillators are perfectly synchronized s.t. $\phi_{\text{ref},N} = y_N$ would perfectly align the head segment with the average body angle.

The computation of $\phi_{\text{ref},N}$ in Eq. (4-6a) is implemented in the head-led target tracking system shown in Figure 4-2 by computing y_N and $-\frac{N+1}{N}\alpha$ separately, and then adding them up. The signal y_N is the output of the head oscillator in the head stabilized Ijspeert model, and $-\frac{N+1}{N}\alpha$ is obtained by multiplying α with the alignment offset gain $-\frac{N+1}{N}$.

There are two notes to be made about this design. First of all, as mentioned in Section 4-1, the design uses the instant motor assumption. In reality, $\phi_k \approx \phi_{\text{ref},k}$, which means that the signal y_N does not perfectly stabilize the head segment. As a consequence, the periodic component of β is not removed but only reduced with the stabilizing part of the controller. However, it is expected that, despite this imperfection, the periodic component of the error due to the body oscillations is reduced, which will improve the performance of the controller. This hypothesis is tested in Section 4-3 to justify the added complexity of the head stabilization algorithm to the design.

Secondly, Eq. (4-4) seems to contradict the turning control objective in Eq. (3-13), since in general α is not zero. It therefore appears that the head-target alignment controller counteracts the turning controller. The reason that these two equations can be used simultaneously is that, as will be explained in Section 4-2-3, α is driven to zero with the turning controller. Making $\bar{\psi}'_{\text{ref}}$ converge to α, and α converge to zero in this fashion has the following reasoning behind it. The head-target alignment controller purposefully creates a head-body alignment error in order to direct the head segment towards the target, which indeed counteracts the convergence of this error to zero. However, this induced error is what contains the information about the misalignment between the body and the target. Driving this error, induced by the head-target alignment controller, to zero with the turning controller is exactly what encompasses the collaboration between the two controllers, which eventually results in directing the body towards the target.

4-2-3 Turning Controller

The head-body alignment objective for head-led target tracking is given in Eq. (3-13a), and is achieved using the turning controller. The head-body alignment problem of the turning controller is visualized in Figure 4-6. Turning gaits in a single chain of Ijspeert oscillators are created by the tuning parameters δ_k (see Section 1-2-3). These parameters induce local curvatures in the body at their corresponding joints k [21], which alters the gait such that the body rotates in the direction of the curvature. This mechanism relies on body-fluid interactions, making the exact relation between the local curvatures and sharpness of turning of the body complex. To overcome this complexity, Amphibot II has been used to determine this relation experimentally [14]. After setting the body curvatures for all joints, the turning radius was measured for different values of the curvature. This showed that, inside the tested range, the inverse of the turning radius increases monotonically with the local body curvature. Amphibot II uses a double chain of Ijspeert oscillators with a different turning mechanism that the one for a single chain. Therefore, a similar experiment is performed using a simulated robotic lamprey in a virtual fluid environment, of which the results are shown in Appendix C. The relation between the turning parameters and the inverse of the turning radius, which is a measure of turning sharpness, is determined to be a monotonically increasing function in the tested range. This indicates that the turning of the robot can indeed be controlled with the turning parameter δ.

Following the turning control strategy in [21] for a single chain of Ijspeert oscillators, the turning parameters are set equal for all oscillators except the head oscillator (i.e. $\delta_k = \delta \; \forall k \in \{1, \ldots, N-1\}$). The turning control law for head stabilized target tracking is written in general form as

$$\delta = f_{\alpha}(\alpha). \tag{4-7}$$

The signal α is used here as error signal, whereas the control objective in Eq. (3-13) requires $\bar{\psi}'_{\text{ref}}$ to converge to zero. However, as shown in Section 4-2-2, α becomes equal to $\bar{\psi}'_{\text{ref}}$ in the limit of $t \to \infty$. Therefore, the signal $\bar{\psi}'_{\text{ref}}$ can be driven to zero by driving α to zero with the control law in Eq. (4-7).

The turning control law used here is based on the controller in [21], which is applied on the same Ijspeert network as used in this thesis (apart from the amplitude dynamics which are

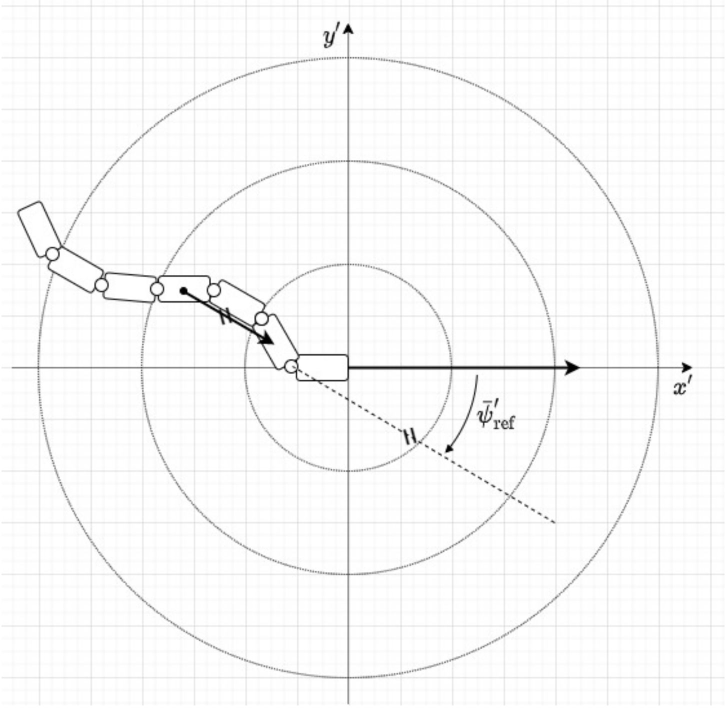

Figure 4-6: Schematic of the head-target alignment control.

irrelevant for this comparison). The source uses a proportional control law with an error signal that is derived from the location and size of the target in the field of view. As described in Section 4-1, visual information does not contain information about the misalignment between the body and the target in the head-led target tracking design, but the offset signal α does. A proportional control law with α as input signal is used here, given as

$$\delta = -K_{\text{t}}\ \alpha. \tag{4-8}$$

Here, K_t is the proportional gain for turning, and the minus sign is again due to the definitions of α and δ. Eq. (4-8) contains the control law for the turning controller subsystem in Figure 4-2. Using a proportional control law without a derivative or integral term would normally have the risk that the error signal keeps oscillating without damping. In this case, this is prevented by the drag force of the water, which acts as a limiter of the derivative.

4-3 Numerical Results

In this section, the numerical results used for verification of the head-led target tracking design are given. The designs used for the simulations are described in Section 4-3-1. Thereafter, the performance of the head-led target tracking design is investigated and compared to two other designs in Section 4-3-2.

The first comparison is with the target tracking design from [21], which will be referred to as the Manfredi design. The Manfredi design produces a head stabilized lateral undulation gait with a single chain of Ijspeert oscillators modified for head stabilization, and uses a turning controller for target tracking. The resemblance between the Manfredi design and the head-led target tracking design provides an opportunity to compare the performance of the two target tracking designs, and can give insight in the different approaches to accuracy improved target tracking.

The second comparison is between two versions of the head-led target tracking design: the regular design that includes the head stabilization algorithm, and an adjusted version of the design that excludes the head stabilizing algorithm. This comparison is made to verify the hypothesis in Section 4-2-2 that the stabilizing part of the controller improves the performance of the controller.

4-3-1 Simulated Designs

The system description of the head-led target tracking design is given in Section 4-2-1. In this design, three different types of controllers are modelled: the motor controllers, the head-target alignment controller and the turning controller. The gains of the controllers are tuned on forehand. The motor controller dynamics are modelled as described in Section 3-3-1 with proportional gain $K_{\mathrm{m,P}} = 20$ and derivative gain $K_{\mathrm{m,D}} = 5$ [8]. The head-target alignment controller is as described in Eq. (4-6a) and (4-3), with proportional gain $K_{\mathrm{h,P}} = 5$ and integral gain $K_{\mathrm{h,I}} = 1$. The turning controller is modelled as described in Eq. (4-8), with a proportional gain of $K_{\mathrm{t}} = 0.15$.

To model the visual unit, the geometry of the target location $\mathbf{p_t}$ and position and orientation of the head segment is converted into a perfect measurement of β. Furthermore, for modelling the head stabilized Ijspeert model, the values in the third column of Table 3-1 are used.

The head-led target tracking design is compared to two other designs which are described below.

Manfredi Design

In the Manfredi design, the head segment is not directed to the target. Instead, the modification to the Ijspeert network is made to decrease the oscillations of the head segment (see also Section 1-3). A description of Ijspeert model, including the head oscillator modification, can be found in [21]. The Manfredi design can not directly be modelled in the simulations, since turning control in this design is done using the pixel size of the target in the field of view. This is not possible in the simulations of this thesis, so instead the error signal β is provided to the turning controller of the Manfredi design (using the same proportional gain as in the head-led target tracking design). The modified Ijspeert model from [21] and the altered turning controller are combined with the visual unit, motor units, body and fluid dynamics described in Section 4-2-1.

Head-Led Target Tracking Design Without Stabilization

The head-led target tracking design with stabilization uses for the head-target alignment controller $\phi_{\text{ref},N} = y_N - \frac{N+1}{N}\alpha$. The head-led target tracking design without stabilization is simulated by using $\phi_{\text{ref},N} = -\alpha$ for head-target alignment control, thereby removing the necessity to compute y_N. All other subsystems are kept the same as described in Section 4-2-1.

4-3-2 Target Tracking Experiment

In this part, the performance of the head-led target tracking design is investigated. The error signals β, $\bar{\psi}'_{\text{ref}}$ and $\bar{\psi}'$ and the time to reach the target are considered performance measures. These signals are retrieved from the simulations using the three different target tracking design in a target tracking experiment.

First, the design of the target tracking experiment set-up on which the experiments are carried out is described. Second, the performance of the head-led target tracking design is evaluated by simulating the head-led target tracking design on the experiment set-up. Third, the head-led target tracking design is compared to the Manfredi design. Fourth, the head-led target tracking method including and excluding the head stabilization algorithm are compared.

Experiment Set-Up

The experiment set-up is shown in Figure 4-7. The target is placed at $(4, 8)$, which is chosen to create a large initial misalignment, both between the target direction and head direction and between the target direction and average body angle. The simulation is terminated when the head tip of the robot (where the cameras are attached) is inside radius 0.1 m of the target.

The head-led target tracking design relies on the states in the Ijspeert model being phase and frequency synchronized in order to function properly. Although perfect convergence takes infinite time for trajectories not initialized in the phase synchronized trajectories, the synchronization error becomes small enough for all practical purposes after some initialization time. From Figure 3-5 and Figure 3-6, an initialization time of 5 seconds is deduced. Therefore, the head-led target tracking design is started after the Ijspeert model has been turned on for 5 seconds. This is done for all three of the designs to keep a fair comparison. It should be noted that the initialization time can vary for different initialization settings.

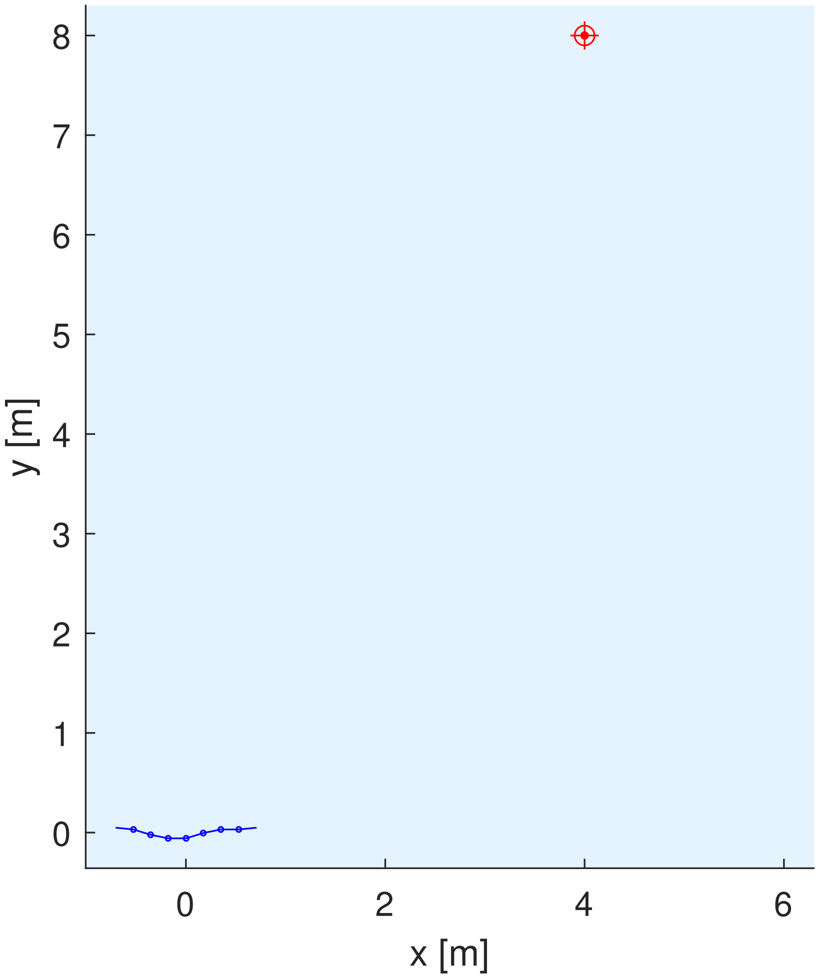

Figure 4-7: The set-up for the target tracking experiments.

Performance of the Head-Led Target Tracking Design

First of all, the simulated robotic lamprey using the head-led target tracking design is capable of reaching the target to within the set radius of 0.1m. In Section 4-2-2 is described that the head-target alignment controller relies on the intermediate objective given in Eq. (4-4). This convergence of the error signal $\bar{\psi}'_{\text{ref}} - \alpha$ is associated with the degree of synchronization of the oscillators, i.e. the error signal is directly caused by the oscillators not being perfectly synchronized. As synchronization between the oscillators only depends on internal states and is not influenced by external signals, it is expected that the asymptotic convergence of the error signal $\bar{\psi}'_{\text{ref}} - \alpha$ to zero is perfect. This is verified by monitoring the error during the target tracking experiment described above. In Figure 4-8, the error is shown for the first 10 seconds of the simulation (which is less that the total simulation time). In the simulated time span, the error appears to converge to zero, verifying that the control objective in Eq. (4-4) is achieved. The error signal converges to a small neighborhood around zero in a similar time span as the phase and frequency differences in Eq. (3-3-2), which is expected as the error is caused by the oscillators not being synchronized. After 5 seconds, this error signal has become small enough for all practical purposes, which justifies the use of the 5 second initialization time.

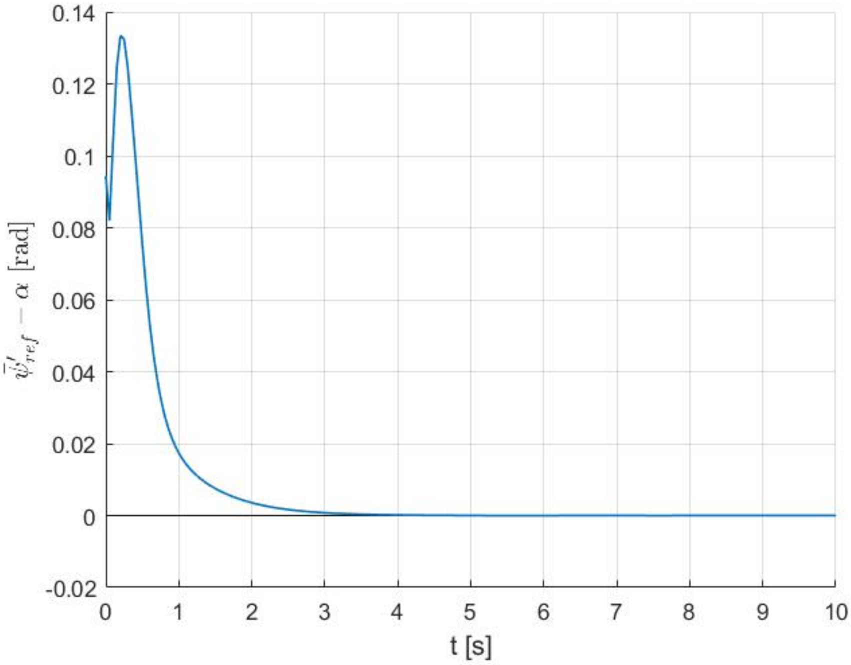

Figure 4-8: Evolution of the error signal $\bar{\psi}'_{\text{ref}} - \alpha$ of the head-led target tracking design.

The head-target alignment controller is responsible for achieving the control objective in Eq. (4-1). The same evolution of β for the head-led target tracking design is shown with the orange lines in Figures (4-9) and (4-11) on a zoomed-out and zoomed-in scale on the y-axis, respectively. Exact convergence to zero is not achieved, although β stays inside a close neighborhood of zero after a few seconds. Moreover, β eventually converges to a neighborhood of just 0.01 radians around zero near the end of the run. To investigate if the remaining oscillations are caused by the non-instant motor dynamics, the motor gains have been increased to investigate their effect on the amplitude of the oscillations (not shown in the figures). High motor gains reduce the amplitude of the oscillations only slightly, indicating that the problem is not just caused by the fact that the instant motor dynamics assumption does not hold.

In Figure 4-10, the evolution of $\bar{\psi}'_{\text{ref}}$ and $\bar{\psi}'$ are shown with orange lines. Contrary to the results in Figure 3-7, perfect convergence of $\bar{\psi}'_{\text{ref}}$ to zero is not achieved in the head-led target tracking design. The reason for this is that $\bar{\psi}'_{\text{ref}}$ equals α in the limit of $t \to \infty$, and α does not perfectly converge to zero because of the oscillations of β visible in Figures 4-9 and 4-11. The oscillation amplitude of $\bar{\psi}'$ is slightly increased compared to that of $\bar{\psi}'_{\text{ref}}$, so it appears that the motors and fluid do not have a large effect on the head-body alignment.

Comparison with the Manfredi Design

The evolution of β for the head-led target tracking design is compared to that of the Manfredi design in Figure 4-9. In the head-led target tracking design, the error β eventually converges to oscillations with an amplitude of about 0.007 rad. Compared to the error in the Manfredi design, in which the oscillations converge to an amplitude of about 0.09 rad, this is about a 13 fold decrease. Moreover, the average around which the error appears to oscillate converge more slowly to zero in the Manfredi design. This is due to the fact that, in the Manfredi design, β is only indirectly reduced with the turning controller. This controller has slow dynamics compared to the the head-target alignment controller that is used to directly reduce the error in the head-led target tracking design. Last, it is notable that the simulation time of the Manfredi design is a little over 10 seconds longer than that of the head-led target tracking design. This either implies that the average speed in the Manfredi design is lower, or the covered path taken to the target is longer in length (or a combination of the two). Judging from the simulation data, both of these turn out to be the case, so both have contributed to the delay.

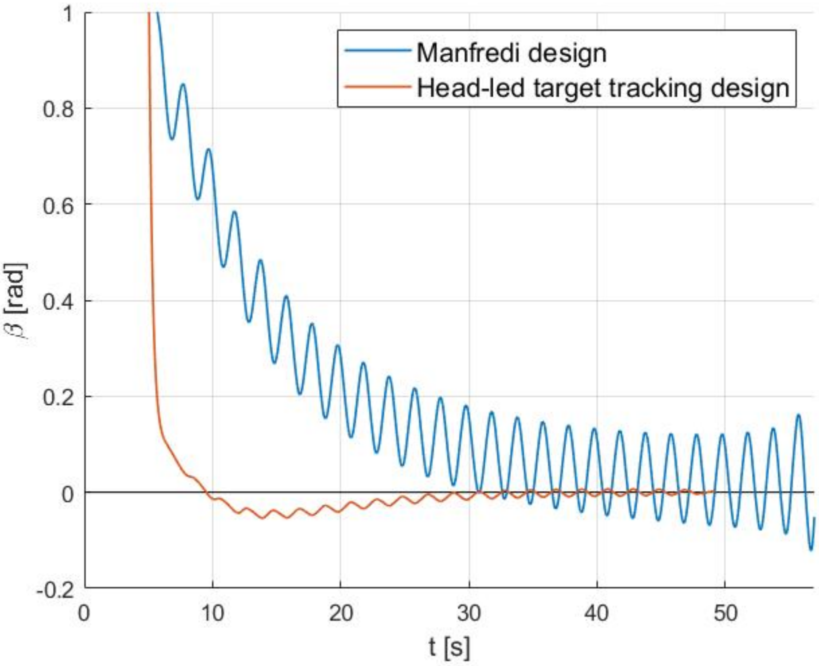

Figure 4-9: The evolution of the error β in the target tracking experiment for the head-led target tracking design and the Manfredi design.

The evolution of the signals $\bar{\psi}'$ and $\bar{\psi}'_{\text{ref}}$ using both the head-led target tracking design and the Manfredi design are shown in Figure 4-10. Both signal $\bar{\psi}'_{\text{ref}}$ and $\bar{\psi}'$ show better performance for the head-led target tracking design than for the Manfredi design, both in terms of oscillation amplitude and speed of convergence of the oscillation averages. Remarkable is that $\bar{\psi}'_{\text{ref}}$ has a larger amplitude than $\bar{\psi}'$ in the Manfredi design, implying that higher motor gains will only worsen the head-body alignment and head stability in the Manfredi design, whereas the opposite is true for the head-led target tracking design.

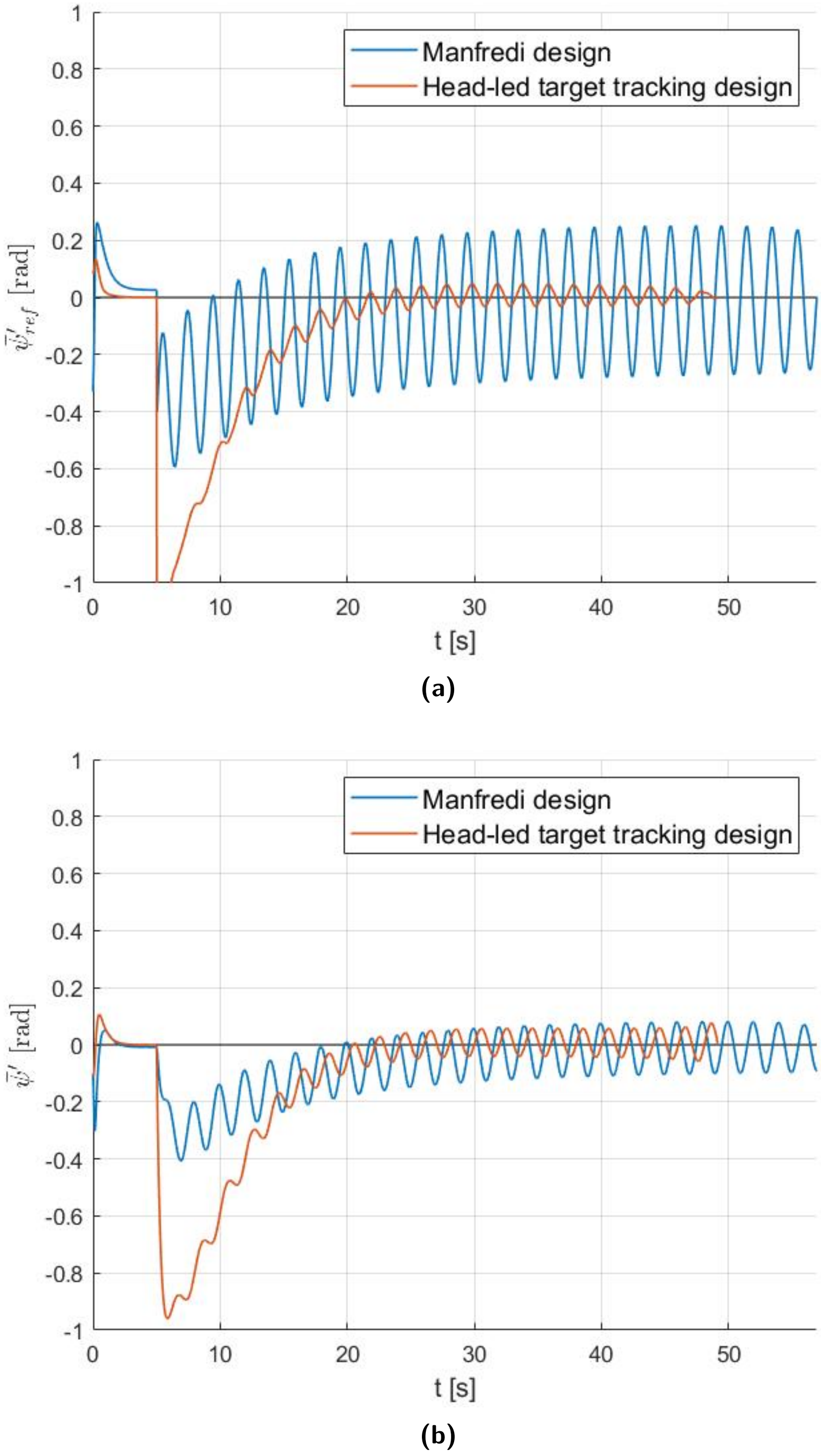

Figure 4-10: The evolution of $\bar{\psi}'_{\text{ref}}$ in **(a)** and $\bar{\psi}'$ in **(b)** in the target tracking experiment using the head-led target tracking design and Manfredi design.

Comparison with the Head-Led Target Tracking Design without Stabilization

The effect of the stabilizing part of the head-led target tracking design is investigated by comparing the error signal β in the head-led target tracking design with and without stabilization. The results of both are shown in Figure 4-11. As hypothesised, the error β in the stabilized variant of the design, although not converging to zero, becomes significantly smaller than the error signal of the non-stabilized variant; the oscillation amplitude near the end is 0.007 rad for the stabilized variant, and 0.02 rad for the non-stabilized variant, meaning the former is smaller by a factor of about 3. The average of the oscillations seems about equally close to zero, with the non-stabilized design performing slightly better at the start, and the stabilized design performing slightly better near the end. Furthermore, the time to reach the target is about six seconds less in the head-led target tracking design including the head stabilization algorithm.

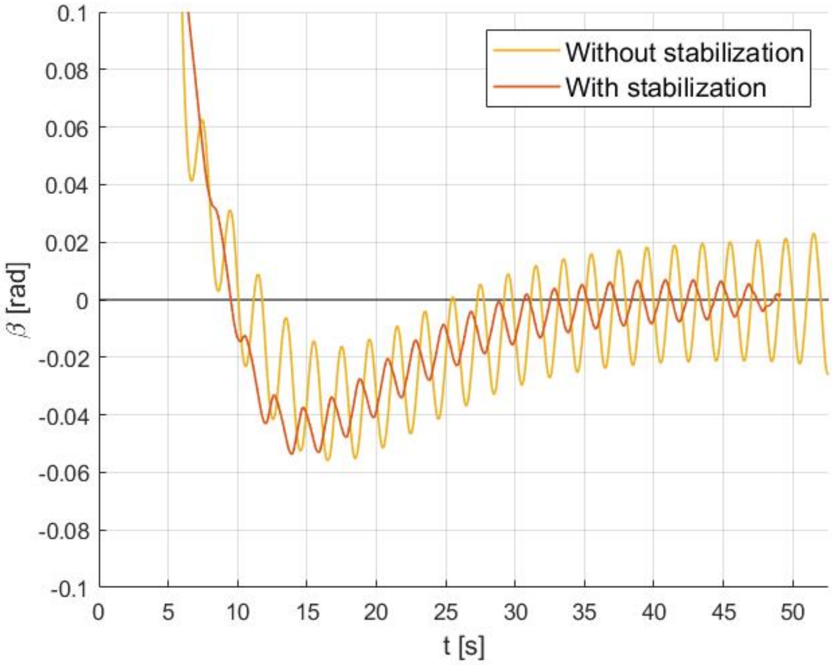

Figure 4-11: The evolution of the error β in the target tracking experiment for the head-led target tracking design with and without stabilization.

4-4 Discussion

Figures 4-9 and 4-11 show that the error signal β keeps oscillating with a certain amplitude that does not seem to get smaller as time increases. This periodic disturbance has the following causes. First, the head joint has to compensate for the lateral undulation gait of the robot, and since the motor dynamics are not instant, this compensation is not perfect. Second, the sideways motion due to the gait of the robot and the fluid forces causes the target to appear to move in the field of view. This is compensated by the head-target alignment controller, which acts with a delay due to the dynamics of the PI-controller part.

In Figures 4-9 is visible that the head-led target tracking design reaches the target in less time than the Manfredi design. In Section 4-3-2, the reason for this was found to be both a higher average speed and a smaller length of the covered path for the head-led target tracking design. A cause for the higher average speed has not been found, although it is expected that designs producing different gaits will provide different average speeds in general. However, the cause of the smaller length of the covered path has been found by studying the simulations. The head-led target tracking design shows a larger initial turn towards the target such that the remaining path is almost a straight line. The Manfredi design showed a more gradual turn, resulting in a curved path towards the target. This difference can be attributed to the orientation of the head segment at the start of the simulation. Namely, in the head-led target tracking design, the head segment initially makes a large angle with the average body angle to direct itself to the target. Combined with a forward gait, this large angle functions as a rudder that steers the robot towards the target.

In Figures 4-9 and 4-10, the error signal β in the head-led target tracking design appears to have a long lasting undershoot, lasting from the 10^{th} second to approximately the 38^{th} second. This undershoot is caused by the short lasting high peak at the start, caused by the initial misalignment of the head with the target. The integration of this part of the curve by the PI controller causes the PI controller to overcompensate. After a while, the area of the curve underneath zero has compensated for the large initial area above zero, and only the smaller periodic oscillations remain. Such an undershoot can possibly be reduced by using a leaky integrator for the PI controller.

The head-led target tracking design has the strategy of only using the head joint for head-target alignment, which causes a large initial kink between the head and neighboring segments. One simplification on the fluid model is that the fluid effects induced by the corners are neglected (see Appendix A), which may not be realistic anymore due to the large kink. This may have influenced how realistic the results from the simulations are. However, the effect of this is not deemed to be too large, as the large kink only occurred at the start of the simulation and only at a small part of the robot.

Chapter 5

Conclusions and Recommendations

This chapter describes the conclusions of this thesis in Section 5-1. After that, suggestions for future work are given in Section 5-2.

5-1 Conclusions

This thesis contains two contributions to the stabilization of visually guided robotic lampreys: the head stabilization method and the head-led target tracking design. Both approach the problem of inaccurate camera inputs from cameras attached to the head segment. Head stabilization is designed to stabilize the head segment itself, and head-led target tracking is designed to stabilize the target in the field of view of the cameras. Conclusions for the head stabilization method are given in Section 5-1-1, and conclusions for the head-led target tracking design are given in Section 5-1-2.

5-1-1 Head Stabilization

The head stabilization method requires the analysis of the phase dynamics of the Ijspeert model in Eq. (1-6), to prove that frequency synchronization between the oscillators occurs, and the phase differences converge to the phase bias terms. This analysis is done by rewriting the phase dynamics of the Ijspeert model as a network of Kuramoto oscillators. The analysis concludes with Lemma 1.1, which states that, if the initial phases of the Ijspeert model obey Assumption 1.1, the phase differences converge according to Eq. (3-2) and (3-3). Simulations of the Ijspeert model in Section 3-3-2 verify Lemma 1.1.

At the start of Section 3-1-2 is described that this convergence of the phase differences in the Ijspeert model has been shown before by [14]. As mentioned in Section 3-4, the approaches in [14] and this thesis seem to arrive at the same results. However, the approach in [14] does not consider the effect of the undesirable unstable phase-locked solutions on the convergence of the phase differences. Therefore, the claim on the convergence of the phase differences in Eq. (3-4) only holds locally, not globally. The approach in this thesis is to rewrite the phase dynamics of the Ijspeert model as a network of phase-coupled Kuramoto oscillators. Restrictions on the initial phases in Assumption 1.1 are found that guarantee the convergence of the phases in the Ijspeert model according to Eq. (3-2) and (3-3).

The proposed head stabilization method in Chapter 3 is made specifically for the Ijspeert model in Eq. (1-6), and is considered the main contribution of the thesis. The head stabilization control problem is defined as aligning the head segment with the average body direction. The average body direction is considered to be a relatively stationary direction, that is still able to turn with the body, and has the benefit of pointing approximately in the direction of motion. Using this formulation of the problem, we approached head stabilization as a control problem, for the first time to the best of our knowledge.

The head stabilization method is proposed in Section 3-2-2. At the start, the assumption is made that the motor dynamics are instantaneous. This allows to analyse only the Ijspeert model and neglect the effect of the motor dynamics and fluid forces on the stabilization of the head. The limit behaviour of the outputs of Ijspeert model, $\boldsymbol{\phi}_{\text{ref}}$, are analysed by separating the Ijspeert model into the phase dynamics $f(\boldsymbol{\theta})$ and the two mapping functions $g(\boldsymbol{\theta})$ and $h(\boldsymbol{\phi}_{\text{ref}})$. The limit behaviour of the phases differences, given in Lemma 1.1, is then used to deduce the limit behaviour of the error signal $\bar{\psi}'_{\text{ref}}$, by analysing the mapping functions $g(\boldsymbol{\theta})$ and $h(\boldsymbol{\phi}_{\text{ref}})$. This analysis yields Proposition 1, which is used to construct the head stabilization method. Proposition 1 provides Ijspeert model parameters for which head stabilization is achieved, i.e. for which Eq. (3-13) holds, under the instant motor assumption and Assumption 1.1. As the convergence of the error $\bar{\psi}'_{\text{ref}}$ is only dependent on the internal states and not on external influences, the head stabilization control objective in Eq. (3-13) holds perfectly. Since head stabilization can be achieved by only requiring specific parameters settings, no changes in hardware or the dynamics of the Ijspeert model are required. Additionally, the head stabilization method can be extended to robotic lampreys using sine-based generators, as mentioned in Remark 1.

In Section 3-3-3, the robotic lamprey is simulated in a fluid environment. Parameters are chosen to make the Ijspeert model generate a head stabilized forward gait with turning. Using these simulations, Proposition 1 and the control objective in Eq. (3-13) are verified to hold. Furthermore, analysis of the effect of non-instant motor dynamics on the head stabilization shows that $\bar{\psi}'$ does not converge to zero, but instead keeps oscillating around a non zero value. However, it is verified that the error $\bar{\psi}'$ decreases for higher motor gains. This implies that, in order to decrease the amplitude of the the head segment oscillations, the motor gains can be increased. This is something to consider when implementing the head stabilization method. Last, the head stabilized Ijspeert model shows significant improvements in terms of oscillation amplitude and offset compared to the Ijspeert model without stabilization (the baseline model), considering the error signals $\bar{\psi}'_{\text{ref}}$ and $\bar{\psi}'$.

5-1-2 Head-Led Target Tracking

The head stabilization method in Chapter 3 is applied to a novel head-led target tracking design, proposed in Chapter 4. This design combines a forward locomotion gait with a turning controller to perform target tracking, and is designed to increase the accuracy of visual information by directing the head segment towards the target. The head-led target tracking problem is subdivided into head-target alignment and head-body alignment. For the head-target alignment problem, a head-target alignment controller is designed that uses visual information to minimize the error between the head direction and the direction towards the target. To reduce the effect from the lateral undulations of the body on the head segment, the head-target alignment controller also includes the head stabilization algorithm. For the head-body alignment problem, a turning controller is designed. This controller uses a proportional control law inspired by [21] that is designed to minimize the error between the direction of the head segment and the average body direction.

The head-led target tracking design is verified in Section 4-3 by designing a virtual target tracking experiment. In this experiment, the robotic lamprey is placed in a virtual fluid environment with a target. The robotic lamprey, using the head-led target tracking design, is capable of reaching the target to within a radius of 0.1m. The head-target alignment error β and the head-body alignment errors $\bar{\psi}'_{\text{ref}}$ and $\bar{\psi}'$ converge to a close neighborhood of zero, although the control objectives in Eq. (4-1) and (3-13) are not perfectly achieved.

The performance of the head-led target tracking design is compared to the target tracking design described in [21]. The latter is simulated on the target tracking experiment, which shows that the considered performance measures, β, $\bar{\psi}'_{\text{ref}}$ and $\bar{\psi}'$, of the head-led target tracking design converge to a closer neighborhood around zero than those of the design in [21]. Furthermore, the oscillation amplitude of the error signals are smaller for the head-led target tracking design. The head-led target tracking design can therefore be considered an improvement to the target tracking design in [21] regarding the error signals β, $\bar{\psi}'_{\text{ref}}$ and $\bar{\psi}'$, as well as the time to reach the target.

Furthermore, the effect of the head stabilization algorithm on the head-led target tracking design is investigated to justify the added complexity of the algorithm. This is done by simulating a robotic lamprey in the target tracking experiment that uses the head-led target tracking design without the head stabilization algorithm. The simulations show that the oscillation amplitude of head-target alignment error signal, β, is about 3 times larger in the design without head stabilization than in the design with head stabilization. Therefore, we conclude that the added complexity of the head stabilization algorithm is justified.

5-2 Future Directions

In the head-led target tracking design in Chapter 4, velocity control is not considered. As explained in Section 1-2-3, the head-led target tracking design needs to be combined with a velocity controller in order to stop the robot close to the target. A simple goal of such a velocity controller can be to make the head segment hover at a certain distance from the target. Another approach is to switch to an entirely different form of control in the close vicinity of the target, fitting the control task at hand.

Both the head stabilization method and head-led target tracking design are designed to stabilize the head segment using only the head joint. A disadvantage of this strategy is that it can result in a large angle between the head and its neighboring segment. This can disturb the water dynamics around the body and reduce efficiency, or even cause clashes between the segments. To prevent this problem, a 'neck' consisting of more than one joint can be considered. The term neck here refers to the set of joints participating in head stabilization, which in this thesis only consists of the front joint. Using more joints in the neck may also allow for a different form of head stabilization that not only directs the head segment in the desired direction but also places it at a desired position. An example of this is to place the head segment in one line with the average body direction (an extension to head-body alignment that is done in this thesis), thereby reducing the sideways motion of the head segment. This is especially of interest for control tasks that require the precise positioning and orienting of the head segment relative to a target. Including more than one neck joint in the head stabilization method can be approached by excluding more joints from ϕ^* in Eq. (3-14) than just $\phi_{\text{ref},N}$. The excluded joints together must then compensate for the effect of ϕ^* on the error signal $\bar{\psi}'_{\text{ref}}$, which can be done with a derivation analogous to the one in Section 3-2-2.

As mentioned in Section 1-3, the approach to increase the accuracy of visual inputs in this thesis has been to stabilize the head segment. A different approach to vision stabilization can be taken based on eye compensation in animals, where movements in the body are compensated by movements in the eyes (see Section 1-3). However, instead of moving the cameras of the robots, the visual data from the cameras can be post processed to compensate for the participation of the head segment in the lateral undulation gait. Like eye compensation works by having the movements of the eyes depend on movements in the body, the post processing of visual data can possibly be achieved by connecting the post processing element to the locomotion signal generator.

Appendix A

Supplementary Material for the Underwater Snake-Robot Model

This appendix provides supplementary material for the underwater snake-robot model described in Section 2-3-1. The content of this appendix is mainly borrowed from [8,17,18].

A-1 Simplifications and Assumptions

In the derivation of the underwater snake-robot model in [17], the following three simplifications are made. First of all, each segment is approximated by an elliptical cylinder with length $2l$, major diameter $2a$ and minor diameter $2b$. Secondly, fluid effects induced by corners (joints) are neglected. Thirdly, the robot is modelled as a slender body.

Furthermore, three assumptions about the fluid are made [17].

1. 'The fluid is viscid and incompressible, and irrotational in the inertial frame.'
2. 'The current in the inertial frame is constant and irrotational.'
3. 'The relative velocity at each section of the link in body-fixed frame is equal to the relative velocity of the respective center of mass of each link.'

A-2 Parameters and Notations

The geometry and properties of the body of the robot are captured with a set of parameters given in the upper part of Table A-1. Since, for the purposes of this thesis, there are no preferences for the dimensions and characteristics of the robot, it has been decided to adopt these from the model of Mamba in [8] for convenience. The parameter values from the source are added to the table.

The lower part of the table shows the fluid parameters of the model. The values of these parameters are computed from fluid and body characteristics. The value or equation from which the value is computed is shown in the table. Note that the number of joints, N, is not the same as in the source.

Parameter	Value	Description
l	0.09m	half length of links
a	0.055m	half major ellipse diameter of links
b	0.050m	half minor ellipse diameter of links
m	0.8kg	mass of each link
j	$\frac{1}{3}ml^2$	inertia of each link (around the z-axis)
ρ	1,000kg/m^3	density of water
C_f	0.3	drag coefficient in the x-direction of motion
C_D	1.75	drag coefficient in the y-direction of motion
C_A	1.5	added mass coefficient
c_t	Eq. (2-13)	fluid force tangential drag coefficient
c_n	Eq. (2-14)	fluid force normal drag coefficient
μ_{n}	Eq. (2-15)	fluid force normal added mass coefficient
λ_1	Eq. (2-16)	fluid torque parameter
λ_2	Eq. (2-17)	fluid torque parameter
λ_3	Eq. (2-18)	fluid torque parameter

Table A-1: Values and definitions of the parameters used in the underwater snake-robot model. The parameters are adopted from [8].

In the coming derivations the following notations are used. First of all, the addition matrix A and difference matrix D are defined as [17]

$$\mathrm{A} \equiv \begin{bmatrix} 1 & 1 & & \\ & \ddots & \ddots & \\ & & 1 & 1 \end{bmatrix}, \qquad \mathrm{D} \equiv \begin{bmatrix} 1 & -1 & & \\ & \ddots & \ddots & \\ & & 1 & -1 \end{bmatrix} \quad \in \mathbb{R}^{N \times N+1} \tag{A-1}$$

Furthermore, the following matrices and vectors are defined [17].

$$\mathrm{K} \equiv \mathrm{A}^\top(\mathrm{D}\mathrm{D}^\top)^{-1}\mathrm{D} \qquad \in \mathbb{R}^{(N+1)\times(N+1)} \tag{A-2}$$

$$\mathrm{V} \equiv \mathrm{A}^\top(\mathrm{D}\mathrm{D}^\top)^{-1}\mathrm{A} \qquad \in \mathbb{R}^{(N+1)\times(N+1)} \tag{A-3}$$

$$\mathbf{e} \equiv \begin{bmatrix} 1 & \dots & 1 \end{bmatrix}^\top \qquad \in \mathbb{R}^{N+1} \tag{A-4}$$

$$\dot{\boldsymbol{\psi}}^2 \equiv \begin{bmatrix} \dot{\psi}_1^2 & \dots & \dot{\psi}_{N+1}^2 \end{bmatrix}^\top \qquad \in \mathbb{R}^{N+1} \tag{A-5}$$

$$\operatorname{sgn}\boldsymbol{\psi} \equiv \begin{bmatrix} \operatorname{sgn}\psi_1 & \dots & \operatorname{sgn}\psi_{N+1} \end{bmatrix}^\top \qquad \in \mathbb{R}^{N+1} \tag{A-6}$$

$$\sin\boldsymbol{\psi} \equiv \begin{bmatrix} \sin\psi_1 & \dots & \sin\psi_{N+1} \end{bmatrix}^\top \qquad \in \mathbb{R}^{N+1} \tag{A-7}$$

$$\cos\boldsymbol{\psi} \equiv \begin{bmatrix} \cos\psi_1 & \dots & \cos\psi_{N+1} \end{bmatrix}^\top \qquad \in \mathbb{R}^{N+1} \tag{A-8}$$

$$\mathrm{S}_\psi \equiv \operatorname{diag}(\sin\boldsymbol{\psi}) \qquad \in \mathbb{R}^{(N+1)\times(N+1)} \tag{A-9}$$

$$\mathrm{C}_\psi \equiv \operatorname{diag}(\cos\boldsymbol{\psi}) \qquad \in \mathbb{R}^{(N+1)\times(N+1)} \tag{A-10}$$

$$\mathrm{J} \equiv j\ \mathrm{I}_{N+1} \tag{A-11}$$

$$\mathrm{L} \equiv l\ \mathrm{I}_{N+1} \tag{A-12}$$

$$\mathrm{M} \equiv m\ \mathrm{I}_{N+1} \tag{A-13}$$

Appendix B

Algorithms

This appendix provides the algorithms of the head stabilization method described in Section 3-2-2, and the head-led target tracking design described in Section 4-2.

Algorithm 1 Head stabilization

```
Input: $N$,  $r_1, \dots, r_{N-1}$,  $\gamma_{1,2}, \dots, \gamma_{N-2,N-1}$,  $\delta_1, \dots, \delta_{N-1}$
Output: $r_N, \gamma_{N-1,N}, \delta_N$
Goal: For given Ijspeert model parameters $N$, $r_1, \dots, r_{N-1}$, $\gamma_{1,2}, \dots, \gamma_{N-2,N-1}$, $\delta_1, \dots, \delta_{N-1}$, compute the head stabilizing parameters $r_N$, $\gamma_{N-1,N}$ and $\delta_N$

Compute $P^\infty$                                   (Eq. (3-28))
Compute $Q^\infty$                                   (Eq. (3-29))

Compute $C^\infty$                                   (Eq. (3-26))
Compute $D^\infty$                                   (Eq. (3-27))
Compute $\delta^*$                                   (Eq. (3-20b))

$r_N \leftarrow C^\infty$                            (Eq. (3-32))
$\gamma_{N-1,N} \leftarrow -D^\infty + \pi$          (Eq. (3-33))
$\delta_N \leftarrow -\delta^*$                      (Eq. (3-34))
```

Algorithm 2 Head-led target tracking

Input: Ijspeert model parameters, body and fluid parameters, motor gains, controller gains, initial states, $\mathbf{p_t}, r_\mathrm{t}$

Output: $\boldsymbol{\psi}, \mathbf{p_{cm}}, \dot{\boldsymbol{\psi}}, \dot{\mathbf{p}}_\mathbf{cm}$ for all time steps

Goal: Run the head-led target tracking method until the target is reached

```
Compute the head stabilizing parameters $r_N, \gamma_{N-1,N}$ and $\delta_N$ with the head stabilization algorithm

Initialize:
    $\boldsymbol{\psi}(0) \leftarrow \boldsymbol{\psi_0}$
    $\mathbf{p_{cm}}(0) \leftarrow \mathbf{p_{cm,0}}$
    $\dot{\boldsymbol{\psi}}(0) \leftarrow \dot{\boldsymbol{\psi}}_\mathbf{0}$
    $\dot{\mathbf{p}}_\mathbf{cm}(0) \leftarrow \dot{\mathbf{p}}_\mathbf{cm,0}$
    $\boldsymbol{\theta}(0) \leftarrow \boldsymbol{\theta_0}$
    Internal state PI-controller $\leftarrow 0$

while $|\mathbf{p}_\mathrm{cam} - \mathbf{p_t}| > r_\mathrm{t}$ do
    Compute $\beta$ from the geometry of the robot and target
    Compute $\alpha$                                                   (Eq. (4-3))
    Compute $\delta$                                                   (Eq. (4-8))
    Compute $\boldsymbol{\theta}$ and $\phi_{\mathrm{ref},\{1,\ldots,N-1\}}$                      (Eq. (1-6))
    Compute $\phi_{\mathrm{ref},N}$                                            (Eq. (4-6a))
    Compute $\mathbf{u}$                                                   (Eq. (3-36))
    Compute $\boldsymbol{\psi}, \mathbf{p_{cm}}, \dot{\boldsymbol{\psi}}, \dot{\mathbf{p}}_\mathbf{cm}$                           (Eq. (2-4))
    Compute the camera position $\mathbf{p}_\mathrm{cam}$ from $\boldsymbol{\psi}$ and $\mathbf{p_{cm}}$
```

Appendix C

Turning Experiment

In Section 4-2-3, the assumption is made that the robot turns with nonzero δ, and the relation between δ and the inverse of the turning radius is a monotonically increasing function. To verify if this assumption holds, a turning experiment is designed. The experiment uses simulations of the robotic lamprey in the fluid with the Ijspeert model without head stabilization described in Section 3-3-1. The experiment described below is inspired by the turning experiment for Amphibot II in [14] [1].

The parameters of the Ijspeert model without head stabilization are described in the second column of Table 3-1. The turning parameter δ is varied between 0.05 and 0.30 rad in steps of 0.05 rad, ranging from a gentle turn to a sharp turn. This induces a turning gait that makes the center of mass of the robot move approximately in circles. To retrieve the turning radius of the robot, the center of mass is tracked until the robot has covered at least three such circles. The turning radius is then approximated by fitting a circle through the trajectory. An example of this is shown in Figure C-1a for $\delta = 0.15$.

The inverse of the turning radii for all different turning parameters are given in Figure C-1b. This figure implies that the inverse of the radius (i.e. the turning sharpness) is indeed a monotonically increasing function of the turning parameter δ in the tested range, which verifies the assumption for the turning controller in Section 4-2-3.

---

[1] As described in Section 4-2-3, Amphibot II uses a double chain of Ijspeert oscillators, which has a different turning mechanism than the one in a single chain. Therefore, a variant of the experiment for a single chain is performed here.

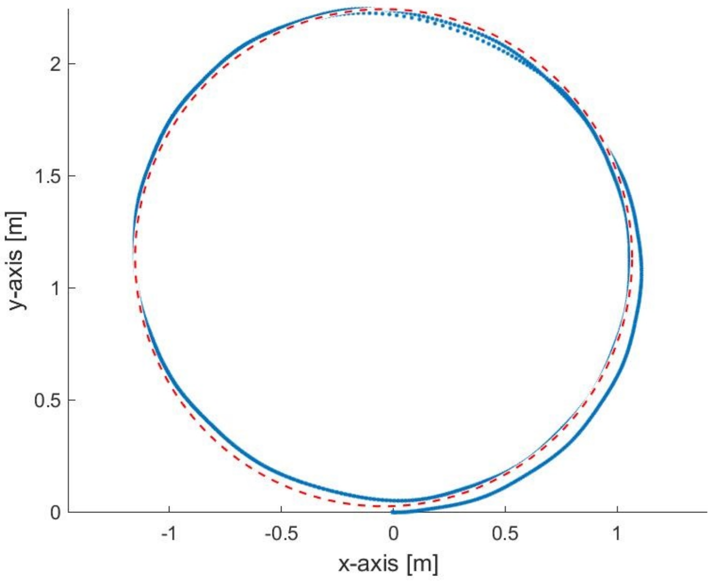

(a)

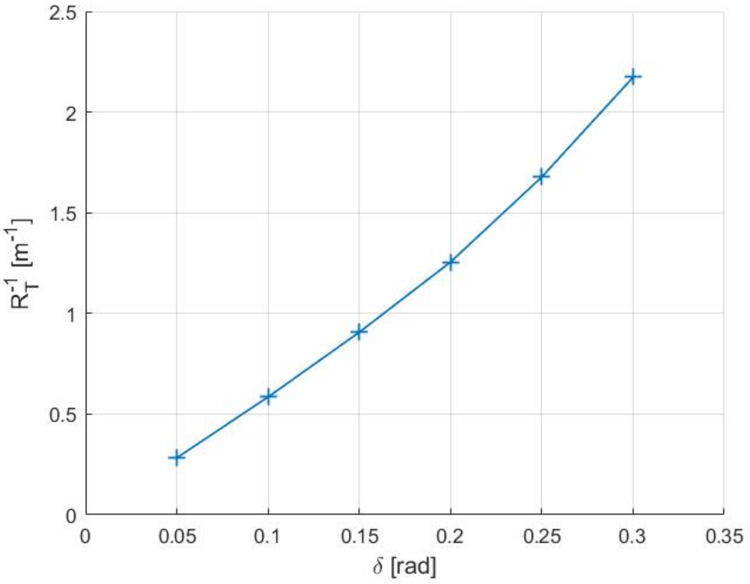

(b)

Figure C-1: The results of the turning experiment with the Ijspeert model without stabilization. An example of the curve fitting method is shown in **(a)** for $\delta = 0.15$ with the trajectory of $\mathbf{p_{cm}}$ shown in blue, and the fitted circle through the trajectory in red. The inverse of all turning radii is plotted against the corresponding δ in **(b)**.

Bibliography

[1] Seaclear. https://seaclear-project.eu/.

[2] Juan A. Acebrón, L. L. Bonilla, Conrad J.Pérez Vicente, Félix Ritort, and Renato Spigler. The Kuramoto model: A simple paradigm for synchronization phenomena. *Reviews of Modern Physics*, 77(1), 2005.

[3] Behzad Bayat, Naveena Crasta, Alessandro Crespi, António M. Pascoal, and Auke Ijspeert. Environmental monitoring using autonomous vehicles: a survey of recent searching techniques, 2017.

[4] Behzad Bayat, Naveena Crasta, Howard Li, and Auke Ijspeert. Optimal search strategies for pollutant source localization. In *IEEE International Conference on Intelligent Robots and Systems*, volume 2016-November, 2016.

[5] Behzad Bayat, Alessandro Crespi, and Auke Ijspeert. Envirobot: A Bio-inspired environmental monitoring platform. In *Autonomous Underwater Vehicles 2016, AUV 2016*, 2016.

[6] P. Breedveld. Memoflex 2 – mechanical cam-following snake, 2021. https://www.bitegroup.nl/category/snake-like-instruments/memoflex-2/.

[7] Quan Minh Dao and Quan Tuong Vo. Design of a CPG-based close-loop direction control system for lateral undulation gait of snake-like robots. In *International Conference on Advanced Technologies for Communications*, volume 2017-October, 2017.

[8] Kelasidi Eleni, Pål Liljebäck, Kristin Y Pettersen, and Jan Tommy Gravdahl. Innovation in Underwater Robots. *IEEE Robotics & Automation Magazine*, (March), 2016.

[9] Chris Godsil and Gordon F. Royle. *Algebraic Graph Theory*, volume 207, chapter 8. Springer Science & Business Media, 2001.

[10] S. Grillner, T. Deliagina, A. El Manira, R. H. Hill, G. N. Orlovsky, P. Wallén, Ö Ekeberg, and A. Lansner. Neural networks that co-ordinate locomotion and body orientation in lamprey, 1995.

[11] Christina L. Hamlet, Kathleen A. Hoffman, Eric D. Tytell, and Lisa J. Fauci. The role of curvature feedback in the energetics and dynamics of lamprey swimming: A closed-loop model. *PLoS Computational Biology*, 14(8), 2018.

[12] Marcus Hultmark, Megan Leftwich, and Alexander J. Smits. Flowfield measurements in the wake of a robotic lamprey. *Experiments in Fluids*, 43(5), 2007.

[13] Auke Jan Ijspeert. Central pattern generators for locomotion control in animals and robots: A review. *Neural Networks*, 21(4), 2008.

[14] Auke Jan Ijspeert and Alessandro Crespi. Online trajectory generation in an amphibious snake robot using a lamprey-like central pattern generator model. In *Proceedings - IEEE International Conference on Robotics and Automation*, 2007.

[15] Ali Jadbabaie, Nader Motee, and Mauricio Barahona. On the stability of the Kuramoto model of coupled nonlinear oscillators. In *Proceedings of the American Control Conference*, volume 5, 2004.

[16] Iman Kamali Sarvestani, Alexander Kozlov, Nalin Harischandra, Sten Grillner, and Örjan Ekeberg. A computational model of visually guided locomotion in lamprey. *Biological Cybernetics*, 107(5), 2013.

[17] E. Kelasidi, K. Y. Pettersen, J. T. Gravdahl, and P. Liljeback. Modeling of underwater snake robots. In *Proceedings - IEEE International Conference on Robotics and Automation*, 2014.

[18] E. Kelasidi, K. Y. Pettersen, P. Liljeback, and J. T. Gravdahl. Integral line-of-sight for path following of underwater snake robots. In *2014 IEEE Conference on Control Applications, CCA 2014*, 2014.

[19] Eleni Kelasidi, Signe Moe, Kristin. Y. Pettersen, Anna M. Kohl, Pål Liljebäck, and Jan Tommy Gravdahl. Path Following, Obstacle Detection and Obstacle Avoidance for Thrusted Underwater Snake Robots. *Frontiers in Robotics and AI*, 6, 2019.

[20] Q. Liu and J. Z. Wang. Modeling and analysis of a new locomotion control neural networks. *Biological Cybernetics*, 112(4), 2018.

[21] L. Manfredi, T. Assaf, S. Mintchev, S. Marrazza, L. Capantini, S. Orofino, L. Ascari, S. Grillner, P. Wallén, Ö Ekeberg, C. Stefanini, and P. Dario. A bioinspired autonomous swimming robot as a tool for studying goal-directed locomotion. *Biological Cybernetics*, 107(5), 2013.

[22] Dan McLeod and John Jacobson. Autonomous UUV inspection Revolutionizing undersea inspection. In *OCEANS'11 - MTS/IEEE Kona, Program Book*, 2011.

[23] Marko Nonhoff, Philipp N. Kohler, Anna M. Kohl, Kristin Y. Pettersen, and Frank Allgower. Economic model predictive control for snake robot locomotion. In *Proceedings of the IEEE Conference on Decision and Control*, volume 2019-December, 2019.

[24] Joram Overdevest. Bioinspired visually guided robotic lampreys. unpublished literature survey, 2021.

[25] Mathieu Porez, Frédéric Boyer, and Auke Jan Ijspeert. Improved lighthill fish swimming model for bio-inspired robots: Modeling, computational aspects and experimental comparisons. *International Journal of Robotics Research*, 33(10), 2014.

[26] Kazuya Saitoh, Ariane Ménard, and Sten Grillner. Tectal control of locomotion, steering, and eye movements in lamprey. *Journal of Neurophysiology*, 97(4), 2007.

[27] H. Sanctuary and E. Barraud. Breakthrough neurotechnology for treating paralysis, 2018.
`https://actu.epfl.ch/news/breakthrough-neurotechnology-for-treating-paralysi/`.

[28] Eric D. Tytell, Chia Yu Hsu, Thelma L. Williams, Avis H. Cohen, and Lisa J. Fauci. Interactions between internal forces, body stiffness, and fluid environment in a neuromechanical model of lamprey swimming. *Proceedings of the National Academy of Sciences of the United States of America*, 107(46), 2010.

[29] Eric W. Weisstein. Graph orientation. `https://mathworld.wolfram.com/GraphOrientation.html`.

[30] A. Westphal, N. F. Rulkov, J. Ayers, D. Brady, and M. Hunt. Controlling a lamprey-based robot with an electronic nervous system. *Smart Structures and Systems*, 8(1), 2011.

[31] Ibrahim Youssef, Mehmet Mutlu, Behzad Bayat, Alessandro Crespi, Simon Hauser, Jörg Conradt, Alexandre Bernardino, and Auke Ijspeert. A Neuro-Inspired Computational Model for a Visually Guided Robotic Lamprey Using Frame and Event Based Cameras. *IEEE Robotics and Automation Letters*, 5(2), 2020.

[32] Junzhi Yu, Min Tan, Jian Chen, and Jianwei Zhang. A survey on CPG-inspired control models and system implementation. *IEEE Transactions on Neural Networks and Learning Systems*, 25(3), 2014.